CRANFIELD UNIVERSITY

ODEH DABABNEH

Multidisciplinary Design Optimisation for Aircraft Wing Mass Estimation

School of Engineering

Centre for Aeronautics

A Thesis Submitted for the Degree of

Doctor of Philosophy

April 2016

CRANFIELD UNIVERSITY

School of Engineering

Centre for Aeronautics

Ph.D. Thesis

Academic Year 2015 - 2016

ODEH DABABNEH

Multidisciplinary Design Optimisation for Aircraft Wing Mass Estimation

Supervisor: Dr Timoleon Kipouros
Co-Supervisor: Dr James F. Whidborne

April 2016

Abstract

Multidisciplinary Design Optimisation for Aircraft
Wing Mass Estimation

Dababneh, Odeh

Ph.D., School of Engineering
Centre for Aeronautics

Supervisor: Dr Timoleon Kipouros
Co-Supervisor: Dr James F. Whidborne

April 2016, 169 pages

The implementation of key technologies in the initial stages of the aircraft wing design process has always represented a substantial challenge for aircraft designers. The lack of reliable and accessible wing mass prediction methods - which allow assessment of the relative benefits of new technologies for reducing structural wing weight - is of significant importance. This necessitates the development of new and generally applicable wing mass estimation methods. This thesis aims to create a new framework for estimating the mass of metallic and composite transport aircraft wings via finite element multidisciplinary analysis, and design optimisation techniques. To this end, the multidisciplinary static strength and stiffness, dynamic aeroelastic stability, and manufacturing constraints are simultaneously addressed within an optimisation environment through a gradient-based search algorithm. A practical optimisation procedure is presented as part of the sizing optimisation process, with enhanced features in solving large-scale nonlinear structural optimisation problems, incorporating an effective initial design variable value generation scheme based on the concept of the fully stressed design. The applicability and accuracy of the proposed approaches is accomplished by conducting a number of case studies in which the wingbox structure of the public domain NASA wing - commonly referred to as the Common Research Model (CRM) - is optimised to produce a minimum mass design.

The results of a case study examining minimisation of the mass of the CRM wingbox structures designed using four different models of increasing structural fidelity prove that the multidisciplinary design optimisation framework can

successfully calculate the mass of realistic real-world aircraft wing designs. This provides an insight into the competence of certain wingbox models in predicting the mass of the metallic and composite primary wing structures to an acceptable level of accuracy, and in demonstrating the relative merits of the wingbox structural complexity models under consideration and the computational resources necessary to achieving the required degree of accuracy.

A feasibility study indicates the importance of taking into account all the loads acting upon the wingbox structures during the CRM wingbox mass estimation process, allowing a lower-mass wingbox design to be achieved. The viability of using composites for the design of the CRM wingbox shows that that the total structural mass saving for the composite CRM wing over the metallic wing is around 21.5%. The breakdown of the CRM wing mass results reveals that the mass of the wing primary structures is a major contributor to the overall mass of the CRM wing. The values of the total mass of the metallic CRM wing and the wingbox mass calculated in the current thesis are generally in good agreement with the values according to the literature, although some discrepancies have been observed. The results of the last study convey the advantage of considering dynamic aeroelastic stability constraints in the early stages of the design process, especially in the case of composite aircraft wing designs. A 5.6% decrease in the total composite CRM wingbox structural mass has been achieved at the cost of a 5.3% decrease in the critical flutter speed. The design continues to be flutter-free within the flight envelope.

The efficiency of the practical optimisation procedure is also investigated. Its performance is illustrated through the application of a case study in which the metallic and composite fourth wingbox models are optimised for a design of minimum mass. It is revealed that the change in the optimised mass value - as a consequence of using different starting values for the design variables, as well as switching between different gradient-based algorithms in deriving the local optimum at each iteration step - is more appreciable in the case of the composite construct than in the case of the metallic. It is anticipated, therefore, that each optimisation algorithm will have completely different search routes from the initial to final points, with the output as the solution. Moreover, using composite construction materials will dramatically alter the size of the design space, thereby increasing the number of solutions available to a designer, with the aim of improving the overall structural performance of the wing components.

Dedicated to the soul of my grandfather
&
To my beloved parents and wife

Acknowledgements

This research has been carried out at the Centre of Aeronautics of Cranfield University Engineering School between November 2012 and March 2016.

I would like to express my sincerest gratitude to my supervisor, Dr Timoleon Kipouros, and I offer my deepest thanks to him for his continual advice, guidance and support throughout my studies. Many warmest thanks also go to Dr James F. Whidborne for his support and advice throughout my research.

I also would like to thank Prof Dr Altan Kayran from METU for encouraging me to pursue my PhD. Without the unique academic knowledge and experience that I gained in my time at METU, I do not think this thesis would have been possible.

I would like to deeply thank my parents, Fayez and Amira, and my wife Linute for their never fading love, support, encouragement and patience throughout the studying and completion time of the thesis.

Special thanks also go to Dr Mustapha Gourma for his support, and encouragement. We had a great time discussing different topics on science, politics and football. Appreciation is also extended to Dr Quintain McEnteggart for his advice and assistance during the course of my studies.

The greatest enemy of knowledge is not ignorance,
it is the illusion of knowledge.

Stephen Hawking

Table of Contents

List of Figures

List of Tables

Nomenclature

Acronyms

ADS	Automated Design Synthesis
ASTROS	Automated Structural Optimisation System
BC's	Boundary Conditions
CAD	Computer Aided Design
CAE	Computer Aided Engineering
CFRP	Carbon Fibre Reinforced Polymers
CRM	Common Research Model
DLM	Doublet Lattice Method
DOT	Design Optimisation Tool
FAR	Federal Aviation Regulations
EAS	Equivalent Air Speed
EASA	European Aviation Safety Agency
FASTOP	Flutter and Strength Optimisation Program
FEA	Finite Element Analysis
FEM	Finite Element Method
FOP	Flutter Optimisation Program
FPS	Finite Plate Spline
FRP	Fibre Reinforced Plastic
FSD	Fully Stressed Design
MDCAD	Multidisciplinary Concept Assessment and Design
MDO	Multidisciplinary Design Optimisation
MMFD	Modified Method of Feasible Directions
MPC	Multipoint Constraint
MSCADS	Modified Version of the Automated Design Synthesis
MTOM	Maximum Take-Off Mass
MZFM	Maximum Zero Fuel Mass
PrADO	Preliminary Aircraft Design and Optimisation Program

SOP	Strength Optimisation Program
VLM	Vortex Lattice Method
WAATS	Weight Analysis of Advanced Transportation Systems

Greek Symbols

α	Angle of attack
α_{dive}	Angle of attack at dive speed
γ	Coefficient of the transient decay rate
γ_{jl}	Damping for the lth root value calculated at the jth velocity
γ_{jREQ}	User-defined required damping value at the jth velocity
$\delta_{tip(Z)}$	Z-Component of the wingtip displacement
$(\delta)^{+}_{max}$	Maximum vertical displacement in positive direction
$(\delta)^{-}_{max}$	Maximum vertical displacement in negative direction
ε	Axial strain
$\varepsilon_{allowable}$	Allowable strain
$\varepsilon_{ultimate}$	Ultimate strain
Θ_{tip}	Angle of twist at the wingtip
$\mu\varepsilon$	Micro strain
μ_g	Mass parameter
ν_{12}	Major Poisson's ratio
ρ	Air density at required altitude
ρ_0	Air density at sea level altitude
ρ_c	Air density at critical gust altitude
ρ_l	Material density
$\sigma_{von\ Mises}$	von Mises stress
$\sigma_{allowable}$	Allowable stress
$\sigma_{ultimate}$	Ultimate stress

σ	Axial stress
τ	Shear stress
$\boldsymbol{\phi}$	Ply angle
ω	Angular frequency
$\boldsymbol{\Omega_x}$	Design space

Roman Symbols

$a_{composite}$	Cross-sectional area of the composite wingbox flanges
$a_{metallic}$	Cross-sectional area of the metallic wingbox flanges
a_s	Speed of sound
$\mathrm{A_i}$	Optimised solution set
$\mathrm{A_{i+1}}$	New optimised solution set
$[\boldsymbol{A}]$	Real matrix
b	Wing semi-span
$\boldsymbol{B}_{hh}$	Modal damping matrix
c	Reference wing chord length
C	Wing chord length
$\bar{c}$	Wing mean aerodynamic chord length
$C_{L,0}$	Zero angle of attack lift coefficient
$C_{L,\alpha}$	Lift curve slope
$[\boldsymbol{C}]$	Damping matrix
D_s	Set of discrete design values
$[\boldsymbol{D}]$	Bending stiffness matrix of the symmetric laminate
E	Elastic modulus
EI	Bending stiffness
$\mathrm{E_{11}}$	Longitudinal modulus
$\mathrm{E_{12}}$	Transverse modulus
FI	Failure index

F_{1c}	Longitudinal compressive strength
F_{1t}	Longitudinal tensile strength
F_{2c}	Transverse compressive strength
F_{2t}	Transverse tensile strength
F_{6}	In-plane shear strength
$f(\boldsymbol{x})$	Objective function
$\boldsymbol{F}(\boldsymbol{x}, t)$	Aerodynamic load vector
$\boldsymbol{F}_a(\boldsymbol{x}(t))$	Aeroelastic force vector
$\boldsymbol{F}_e(t)$	Externally applied non-aeroelastic force vector
g	Damping value
g	Gravitational acceleration
$GFACT$	Scale factor
GJ	Torsional stiffness
G_{12}	In-plane shear modulus
$\boldsymbol{h}$	Vector of equality constraints
I_{xx}	Area moment of inertia
$[\boldsymbol{I}]$	Identity matrix
k	Reduced frequency
k_b	Beam bending stiffness
k_g	Gust reduction factor
$[\boldsymbol{K}]$	Stiffness matrix
$\boldsymbol{K}_{hh}$	Modal stiffness matrix
L	Lift force
$\boldsymbol{l}$	Vector of inequality constraints
M_C	Cruise Mach number
M_D	Dive Mach number
M_{Ref}	Reference Mach number
M_∞	Free stream Mach number

$M(\boldsymbol{x})$	Objective function representing the wingbox structural mass
$[\boldsymbol{M}]$	Mass matrix
$\boldsymbol{M}_{hh}$	Modal mass matrix
n	Manoeuver limit load factor
n_g	Gust load factor
n_{ply}	Number of plies
$N\ element$	Number of elements in the finite element model
p	Eigenvalue parameter
$prop_{\mathrm{i}}$	Element/panel property value
$[\bar{\boldsymbol{Q}}]_K$	Transformed reduced stiffness matrix of the kth layer
$\boldsymbol{Q}_{hh}$	Complex aerodynamic matrix
$\boldsymbol{Q}_{hh}^{Im}$	Imaginary part of complex aerodynamic matrix
$\boldsymbol{Q}_{hh}^{Re}$	Real part of complex aerodynamic matrix
R	Set of interior starting points
S	Reference wing area
S	Set of initial starting points
$t_{metallic}$	Thickness of the metallic wingbox panels
U_{de}	Gust velocity at critical gust altitude
$\boldsymbol{u}_h$	Modal amplitude vector
V	Design speed
V_A	Manoeuvring air speed
V_C	Cruise speed
V_D	Dive speed
V_l	Volume of the lth element
V_{NE}	Never exceed speed
V_∞	Free stream velocity
W	Maximum take-off weight

W_{wing}	Wing mass
x	Design solution
$\boldsymbol{x}$	Design variables vector
$\boldsymbol{x}_b^L$	Lower bound on design variables vector
$\boldsymbol{x}_b^U$	Upper bound on design variables vector
$\boldsymbol{x}_s$	Discrete design variables vector
$\boldsymbol{x}(t)$	Structural deformation vector
$(Z_k - Z_{k+1})$	Ply thickness

Other parameters are clearly defined wherever applicable.

Chapter 1

Introduction

1.1 Background to the Study

Commercial aviation is a key component of the world's economic development and growth. In recent years, air traffic has experienced an average global growth rate of approximately 4-5% per annum [1] and the demand for aviation transportation is expected to continue and even increase in the future. The continued growth in air travel has led to substantial increases in the emission of gases attributed to global warming, including carbon dioxide, and, given the increasing importance of climate change within the global political agenda, there is a general demand to reduce the environmental impact of transportation, including aviation. Aircraft manufacturers have made significant efforts and have issued ambitious goals for the reduction of emissions in air traffic and transportation. Over the last decade, different concepts and technologies, ranging from completely new aircraft design concepts, like the box wing aircraft [2,3] and the blended wing body [4,5], to the implementation of new technologies in more conventional aircraft designs, have been suggested to face the increased economic and environmental challenges. Examples of key enabling technologies are the use of advanced materials, such as composite materials and carbon fibre reinforced polymers (CFRP), high aspect ratio laminar flow wings [6,7], and wing configurations utilising high lift device concepts to decrease aircraft noise during take-off and landing [8]. Furthermore, innovative detailed technologies, like the NASA shape-changing wing equipped with novel morphing technology [9], must be considered for the new generation of aircraft.

In recent years, aircraft manufacturers and research institutes have been focusing on aircraft concepts that require new wing designs. The NASA Common Research Model (CRM) for a generic transport aircraft model is an example [10,11]. The design of an efficient aircraft wing featuring new technologies has always represented a substantial challenge for aircraft designers, especially when the proposed novel concept challenges the existing knowledge base and the accuracy of normally used empirical methods and statistical data collected from previously constructed aircraft.

During the development of new aircraft, the structural mass of an aircraft has always been a key performance indicator. The wing of a modern transport aircraft is one of the heaviest structural components, and therefore a particular focus has always been placed on the accurate estimation of wing structural mass. The lack of reliable and accessible wing mass prediction methods that allow assessment of the relative benefits of novel technologies that can enhance the lift-to-drag ratio of the aircraft wing, while reducing the structural wing weight, is of significant importance. It requires the development of new and generally applicable wing mass estimation methods.

Determining the mass of an aircraft wing, for which the database is insufficient or non-existent or the wing design lies beyond the use of empirical methods, via fully integrated finite element analysis and design optimisation software packages appears to be a promising approach to consider at the early stages of the design process. This has been made possible over the last 10 years by the increased processing power of computers, the advancements in computer-aided design, the enhancement of multi-dimensional design space visualisations, simultaneous calculation, visual screening and representations of a variety of design analysis and optimisation results [168].

1.2 Thesis Objectives

The preceding discussion highlights various challenges that arise when new advanced technologies are used in the design of a new aircraft wing. Implementing key technologies at the initial stages of the aircraft wing design process requires re-evaluating the existing wing mass estimation methods. These existing methods were not designed to take into account the advantages of these new technologies. By addressing the challenges surrounding wing mass estimation methods, this

thesis aims to further investigate and explain the influence of such technologies on mass estimation of primary and secondary aircraft wing structures.

Three main research objectives provide the scope and direction for the work presented in this thesis.

The first objective is to generate a wing mass estimation framework based on multidisciplinary analysis and design optimisation techniques suitable for the preliminary stage of the design process. It is fulfilled by constructing a wingbox cross-section using four different models of increasing structural complexity, showing the wingbox structural components idealised by finite elements. The wing mass estimation process consists of structural sizing and optimisation to satisfy a set of pre-defined design requirements. Design and modelling tips are also provided to avoid potential challenges when introducing local loads and boundary conditions to the wingbox model.

The second objective is to develop a practical optimisation procedure for handling large-scale nonlinear structural optimisation problems. This is achieved by proposing and investigating a practical optimisation procedure that utilises the existing local optimisation capability of MSC.Nastran based on gradient-based algorithms. This includes using different techniques and algorithms to find an optimum solution.

The third objective is to demonstrate and validate the applications of the investigated approaches in estimating the mass of an aircraft wing. This is accomplished by conducting a number of case studies to reveal the usefulness of the wing mass estimation and practical optimisation methods. The CRM wing featuring new technologies is used in particular to gain insight into the value of these methods.

1.3 Thesis Outline

Each chapter in the thesis builds on prior material and they are organised as follows.

Chapter 2: The phases of aircraft design and the development process are discussed. The open literature on the subject of wing mass estimation methods and optimisation techniques and their applications in the aerospace industry is reviewed and relevant data are presented to provide reference materials for

subsequent chapters. Perspectives are drawn from the research gaps identified and are used to propose a framework for wing mass estimation and a practical procedure for large-scale structural optimisation problems.

Chapter 3: In this chapter, an overview of the wing mass estimation approach for conventional aircraft is given, and is modified as necessary to accommodate the implementation of key technologies in recent aircraft designs. Next, a methodology for determining the mass of a transport aircraft wingbox structure using Multidisciplinary Design Optimisation (MDO) is presented. The design and analysis tools employed in this study are also discussed.

Chapter 4: This chapter is dedicated to the structural design process of typical transport aircraft wingbox models using the design tools and methodologies described in Chapter 3. The public domain NASA wing, commonly referred as the Common Research Model, is used as a baseline model.

Chapter 5: The chapter describes the development of the finite element model of the CRM wingbox configurations discussed in Chapter 4. The finite element type selection, mesh quality checks, boundary conditions and wing load introduction methods will be presented. The finite element model was developed to be used in the structural optimisation module for sizing and mass estimation of the primary wing structure components.

Chapter 6: The objective of this chapter is to propose and investigate the efficiency of a practical optimisation framework in solving large-scale nonlinear structural optimisation problems with the existing local optimisation capability of MSC.Nastran based on gradient-based algorithms. Particular emphasis is given to generating good initial starting points for the search process and improving the opportunity of finding a better optimum solution.

Chapter 7: In this chapter, the structural optimisation of the CRM wing primary structures, both metallic and composite, is performed using a finite element method in conjunction with numerical gradient-based optimisation techniques. The optimisation problem is first described and then mathematically formulated in terms of the objective function, imposed constraints and design variables. During the optimisation, the effects of using different starting points for the design variables, as well as different gradient-based algorithms and the effect of including aeroelastic constraints on the optimised wingbox configurations, are also investigated.

Chapter 8: General conclusions and recommendations for future work are presented.

1.4 Contributions to Knowledge

The contributions to knowledge, which have been made as a result of this research, are summarized below:

- Creation of a novel framework for estimating the mass of transport aircraft wing based on Finite Element Analysis (FEA) and Multidisciplinary Design Optimisation (MDO) techniques that are suitable for the preliminary stage of the design process.

- A revealing study into the consequences of using wingbox cross-section models that increase structural complexity on the wing mass estimation results for conventional aluminium alloys and composite designs.

- A gainful analysis of the impact of considerations of the dynamic aeroelastic stability constraint (flutter) at early stages within the design process, notably for composite aircraft wing designs.

- Proposal of a practical optimisation procedure in solving large-scale nonlinear structural optimisation problems, using the existing local optimisation capability of MSC.Nastran which is based upon gradient-based algorithms.

- A valuable study into the effects of using different starting values for the design variables as well as different gradient-based algorithms in deriving the local optimum solutions for conventional aluminium alloys and composite designs.

Chapter 2

Review of the Literature

2.1 An Overview of the Aircraft Design Process

Aircraft design and development is a complex and fascinating process. It is the academic engineering process of creating a flying machine to a certain set of specifications and requirements established by either a prospective user or pioneering innovative ideas and technology. The aircraft design process is described in many aircraft design textbooks [12,13,14]. According to these textbooks, the process, which requires design experience as well as good intuition, takes place in three distinct phases. Figure 2.1 shows the aircraft design and development phases [14].

During the first phase, the conceptual design, the overall size, shape, weight and performance of the aircraft are determined, yielding the general layout. Throughout this stage, the configuration of the aircraft is developed using simple methods and tools that require only a few input parameters and are therefore well suited to this particular design phase. The second phase, the preliminary design, involves structural and control system analysis, detailed wind-tunnel testing and computational fluid dynamics calculations. During this stage, the aircraft concept remains largely unchanged and only minor modifications are made. The detailed design phase is the last phase in which the precise designs of each individual part of the aircraft are prepared for production. The size, number and locations of aircraft structural elements and fasteners are decided and manufacturing tools are designed. At each phase of the design process, each design decision is evaluated for its impact on overall performance, weight and unit cost of the aircraft, since

an accurate prediction of aircraft weight during the initial stages is essential in achieving an optimum and successful configuration [14].

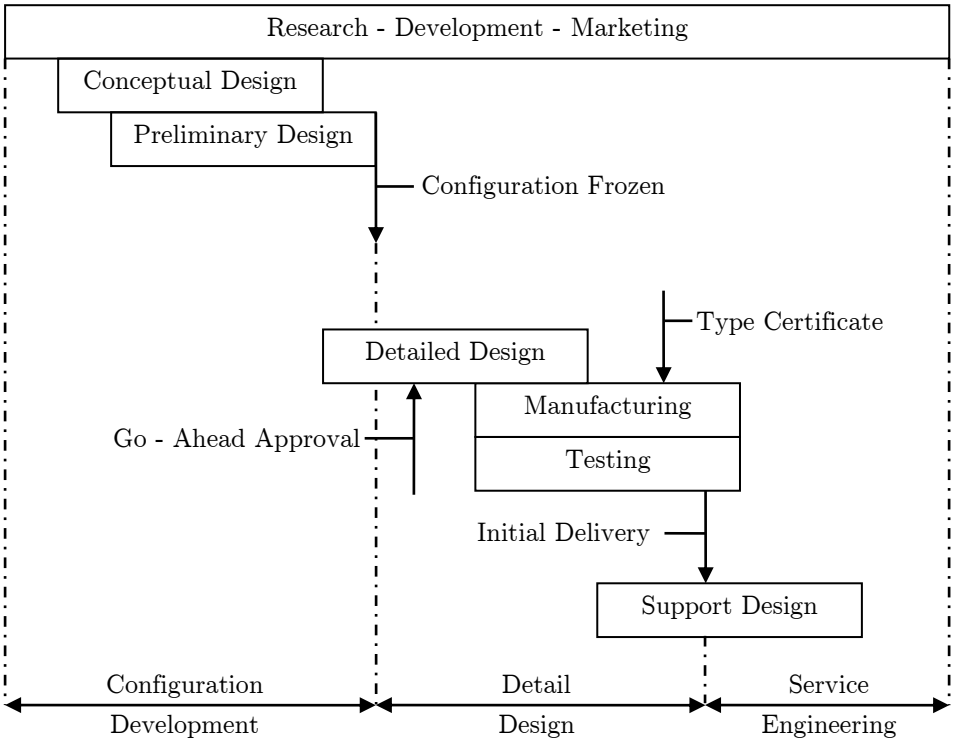

Figure 2.1: Development phases of the aircraft design process

2.2 Classifications of Wing Mass Estimation Methods

The total mass of the primary and secondary structures of an aircraft has a big influence on the overall performance and cost development of the aircraft at the initial design stages. Reducing the structural mass has the effect of lowering the operating empty weight, allowing the aircraft to fly higher payloads at a greater range. In the literature, great efforts have been put into and reported on developing wing mass prediction methods. This is because of the well-defined structural role of the wingbox as a primary load-carrying component and the importance of optimum wing design as a significant subject of the preliminary design phase [15].

Different classifications for mass estimation methods have been developed by many authors in recent years. In his study, Murphy [16] places mass estimation methods into three classes: purely statistical, hybrid analytical-statistical and

purely analytical methods. Ardema et al. [17] classify wing mass prediction methods by increasing order of complexity and accuracy as empirical regression, detailed finite element structural analysis and classical plate theory based methods. Kundu [18] divides weight estimation methods at the conceptual design level into three methods, addressed as:

- the rapid method, based on empirically determined weight fractions used to estimate the weight of major aircraft components;

- the graphical method, statistically based on weight equations for existing aircraft used to predict the weight of major components such as a wing;

- the semi-empirical method, usually consisting of analytically based equations, which are adjusted using statistical correlations from historical data.

Recently Elham [19] logically divided mass estimation techniques into four categories:

- class I methods, termed fractions methods, where mass of each aircraft component is defined as a fraction of the maximum take-off mass of the aircraft. To establish ratio of the mass of a particular component (e.g. wing) to the aircraft mass, a number of existing aircraft designs of the same class and category as the aircraft under study are analysed. Typically, these techniques are used at initial stages of aircraft design process.

- class II methods, where in addition to coefficients obtained by statistical analysis of existing aircrafts, aircraft parameters such as design speeds, load factors, geometrical dimensions, configuration aspects, etc. are included into sets of empirical equations to calculate mass of every fundamental aircraft component.

- class II & 1/2 methods, based on estimation of the mass of material, required to withstand a certain loads applied to a particular aircraft component. In order to calculate the required amount of material, basic strength/stiffness analysis is applied to simplified structural model of the load-carrying component. The use of statistical and experimental data may be considered to improve performance of these methods. These methods

allow studying the influence of particular design decisions on the estimated mass of aircraft component or group of components.

- class III methods, in these methods the mass of the aircraft primary structure is calculated using Finite Element Method (FEM). Since the influence of the secondary and non-structural masses on the aircraft structural loading is not computed in FEM, other analytical and empirical methods are still required.

In summary, wing mass estimation methods can be logically separated between three categories: Empirical, Analytical and based on Finite Element Analysis, although each category can be divided into sub-categories. Advantages and drawbacks of methods falling in these categories will be compared in sections 2.2.1-2.2.3.

2.2.1 Empirical and Semi-Empirical Based Methods

Empirical wing mass estimation methods are mostly based on statistical data from previously investigated or constructed aircraft and rudimentary performance equations of the most significant design parameters, but it is also possible to have experimentally based methods. The simplicity of understanding and applying these methods can be of some use at the initial stages of the conceptual design process in order to approximate the mass breakdown of major components such as maximum take-off mass, payload mass and wing mass.

A great and valuable contribution to the field of aircraft design is attributed to Raymer [12], Roskam [13] and Torenbeek [14]. The empirical wing mass estimation methods developed by these authors are still in use by many aerospace manufacturing research centres and university researchers in the field of aeronautical engineering today. A typical example of a purely statistical-based method is *WAATS - A Statistical Based Prediction Method*, given by Murphy [16]. The method was fully explained and coded for use on computers by Glatt [20]. According to Ardema [17], however, the implementation and accuracy level of statistical-based methods in predicting wing mass depends primarily on the amount and quality of the data available for existing aircraft, in addition to how closely the presented aircraft matches the design and configuration concept, mission profile and weight of the aircraft under investigation. These conditions make statistical-based methods of limited practical use to the designers of an

innovative design concept, where the novelty is in the configuration or the material used. As an example, the wing mass prediction method of Torenbeek [21] presents remarkably good results, but it is limited to subsonic transport aircraft only.

Semi-empirical methods, on the other hand, are used when a simplified geometrical layout of the aircraft configuration becomes available. These methods are used to estimate the mass of the primary structural components of an aircraft such as the wing, fuselage and landing gear. This is done using analytically based equations that combine geometrical parameters, load factors and aircraft design speeds, adjusted using statistical data correlations derived from the weight breakdowns of existing aircraft [18]. These methods enable the design engineers to assess the effect of geometrical design parameters such as wingspan, sweep angle, and taper ratio on wing mass. Examples of semi-empirical methods are found in most aircraft design books [12,13,14,15]. Howe [22] presented a method, which calculates the mass of the wing as a function of the main geometrical and operational parameters. This method was called the C_1 method, where C_1 is a coefficient dependent on the type of aircraft. The method was only applicable to wings made from light alloy and further work was needed to cover composite construction. Moreover, some experience was needed to account for any special features of the design. Although semi-empirical methods improve the accuracy of the wing mass prediction compared to statistical-based methods, the effect of the internal wing structural design configuration, like the number and location of spars, stiffeners and ribs, still cannot be evaluated at this stage.

2.2.2 Analytical and Quasi-Analytical Based Methods

Purely analytical structural analysis methods for mass estimation are rarely found in the literature. In 1960, Ritter [23] presented a method for obtaining a realistic wing rib mass estimate using structural analysis techniques which could be applied to a wide range of structural configurations. A simple geometry was considered for analysing and sizing the rib and the weight was calculated by determining the amount of material necessary to satisfy structural rigidity and flexural strength requirements. The method was too complex to be used for parametric weight comparison and was only applied to proposal studies.

During the 1950s, Burt [24] and Shanley [25] presented a new mass prediction method based on elementary strength/stiffness analysis improved by statistical

and experimental data. In this quasi-analytical method, the material amount required to resist the applied loads is computed using structural analysis of simplified wing models. This method has enabled mass engineers to obtain higher accuracy and better design sensitivity results. In 1954, Spath [26] derived a general form for wing mass estimation based on a simple beam representation of an airplane semi-wing. The load distribution acting on the wing was represented by bending moment and shear force distributions. The amount of material needed to resist this load at each station semi-spanwise was then estimated and the wing mass was calculated by integrating the mass of the shear and bending material over the span.

John, St. [27] illustrated the principles of analytical-statistical weight prediction methods by using the engineering analysis bending stress equation to derive a correlation expression, and statistical analysis was used to apply the correlation expression to available aircraft data. The method was considered useful at the beginning of the preliminary design stages where detailed information was available and it showed better average results than other existing methods at the time. Lewis et al. [28] made a major contribution to the area of weight estimation with the development of allowable stress estimation methods particularly tailored to preliminary design prediction methods.

Anderson and Udin [29] presented a theoretical wing mass derivation method based on a simplified concept model of a subsonic aircraft wing. The wing was divided into different components and, by analysis of the wing loads, the relative mass of the wing was estimated as a function of bending moment, twist moment and shear force. Besides being applicable for subsonic aircraft wing models only, the application of this method required too much input data, which limited its use. A number of design-sensitive mass prediction methods based on refined analytical methods for the wing structures of transport aircraft were developed by Torenbeek [21]. A theoretical method, called the F method, was developed by Howe [22], where the wing mass was calculated as the sum of the masses of:

- spanwise covers, booms and shear webs of the structure;
- ribs, the mass of high lift devices and secondary fairings;
- assorted items e.g. power plants, store attachments, landing gear, etc.

In his early studies, Howe suggested that the mass of spanwise covers/booms and shear webs was determined by strength and stiffness considerations in order to satisfy aeroelastic requirements, and in later studies he indicated that aeroelasticity may have a local effect on some parts of the structure. This method was applicable to conventional wings made of light alloy only and gave more accurate results than the C_1 method mentioned in the previous section.

An overview of an advanced conceptual wingbox weight estimation model for transport aircraft was given by Ajaj et al. [30]. The wingbox was modelled based on linear thin-walled beam theory as a simple, swept tapered multi-element beam. The weight of the wingbox was estimated based on the sizing process, including static aeroelastic requirements. The model was validated using five different transport aircraft and showed adequately accurate and reliable results.

Macci [31] presented a method for predicting the wing mass of an aircraft at the preliminary design stage. The theory behind this method was based on the fact that the wing structural box must be designed to meet both the bending strength and the torsional stiffness requirements, due to an assumed trapezoidal lift distribution acting on a rectangular wingbox. Mathematical relations for structural sizing were developed and coded to enable the method to be used as an effective design tool for structures made from both metallic and fibre reinforced plastic (FRP) materials. He concluded that despite the accurate wing mass results provided, it would be wrong to consider this method completely accurate for establishing final design masses. He also illustrated the importance of having detailed information on the wing geometry and construction to establish an accurate wing mass prediction method for existing aircraft, as well as the need for testing the proposed method for aircraft wings made from FRP materials.

Elham et al. [32] proposed a weight prediction method for aircraft lifting surfaces, known as the EMWET method. In this method, the primary wing structure weight was predicted using an advanced analytical method which took into account the structural layout, the actual geometry of the aerodynamic surfaces and the spanwise lift distribution, calculated using the Vortex Lattice Method. The weight of the secondary wing structures was predicted using semi-empirical methods. Mathematical equations were used to relate the required structural properties of the wingbox to the specific shape of the airfoil used. By using these equations, the skin, the spar caps and the stringers of the upper and lower sides of a given wingbox were modelled as two equivalent flat panels and the effective

distance from each other was calculated, making it possible to take into account the effect of the airfoil shape on stress distribution in the flat panels, thereby enabling an accurate panel weight estimation. The method was validated using data from different conventional aircraft and the method proved to achieve more accurate results than similar existing methods.

During the last few decades, different tools and software implementations have been developed based on analytical and quasi-analytical methods. In 1973, WP15 was developed as an improved version of the BAe Subsonic Wing Weight Program WP043. The program used analytical methods for sizing the primary structure components under bending and shear forces and empirical methods for estimating the masses of other components [33]. The program could not handle kinked leading edges and it was considered valid for wings with aspect ratios between 6 and 12. In 1987, Dijk [34] developed a program for Airbus Industry in Toulouse. The program provided a rapid weight prediction of the wing structure components based on appropriate structural parameters derived from strength considerations. These parameters were correlated with actual weight data using linear regression. The AdAstra program [35] was developed in 2002, in which the wing mass was estimated by sizing the primary structure using a stationary structural analysis approach, while a set of statistical data was used to estimate the mass of the secondary structures. The application of this program was limited to conventional transport aircraft.

In 1996, Ardema et al. [17] developed an analytical method for wing and fuselage mass estimation of transport aircraft. This method was based on estimating aircraft loads and modelling the aircraft wing and fuselage structure as an Euler-Bernoulli beam. This method was integrated into a PDCYL computer program that had been made into an ACSYNT (AirCraft SYNThesis) computer program, and was used to estimate aircraft mass in vehicle design studies. The method was limited to subsonic conventional aircraft configurations and did not account for aeroelastic effects. Terpstra [35] conducted a study to compare the accuracy of the WP15 and AdAstra programs and the methods presented by Torenbeek and Dijk for wing mass estimation. The study indicated that the accuracy of wing mass prediction methods can vary significantly. Some methods used simplified structural models to represent the wing geometry, while other methods considered a more detailed representation.

FAME-W (Fast and Advanced Mass Estimation Wing) is weight prediction software designed by Airbus Germany [36,37]. It can estimate the mass of a transport aircraft wing while considering the effects of static aeroelasticity. A beam model representation and analytical methods are used for the analysis and sizing of the wingbox structure. Despite the relatively simple geometrical and structural modelling capabilities, this tool offers a high computational efficiency and it is always revalidated against weight data from existing aircraft configurations.

2.2.3 Finite Element Based Structural Optimisation Methods

One of the early attempts in the literature at using finite element techniques for aircraft mass estimation was proposed by Nisbet et al. [38]. A scheme was first proposed that used engineering bending theory as a base for simpler analysis; later on, the authors presented a finite element method based on structural optimisation. These methods were intended to produce mass values for comparison and optimisation purposes rather than for mass estimation on its own.

In their study, Hutton and Richmond [39] derived a methodology for the application of the finite element analysis method to estimate the structural system weight. This resulted in the development and testing of a numerical weight correction factoring logic, which is composed of a number of sub-factors that account for modelling assumptions, material properties and other weight-sensitive variables that are built into the finite element process as functions of the individual element's geometry. This allowed a reasonable weight estimate to be achieved as a direct result of the automated resizing process. Another study on the use of the algorithmic mass factoring approach applied at the finite element level was given by Pincha [40]. In his study, he derived an algorithm using modelling design and manufacturing criteria for a structural concept. He computed weight increments, each of which represented a non-optimum structural weight, by optimised sizing using geometry and material properties.

Murphy [16] developed a computerised wing mass prediction method, which did not rely on a database of existing aircraft, using finite element analysis techniques. He tested the feasibility of this method for rapidly calculating the weight of an aircraft. The weight results achieved were compared to the results

obtained by the advanced analytical-empirical methods [27,28]. He concluded that a feasible solution and good accurate results can be achieved using the proposed computerised method. Doregkamp [41] presented a technology developed by the McDonnell Aircraft Company to transform the theoretical structural finite element model, with design details such as geometry, material properties and loading, into a realistic weight estimate. In his study, he emphasised the importance of finite element method weight-estimation software for the calculation of the modelled weight and the accurate representation of the structural assembly.

Zaidel [42] illustrated the use of the finite element method as a viable weight-engineering tool. The finite element method was also used in the A-12 aircraft project to distribute structural target weights to enhance the accuracy of the aircraft and determine realistic structural weights, which in turn provided an early indication of potential overweight areas.

Mitchell [43] described the integration process of the tools for finite element mass property analysis for Weight Engineering at Boeing in a multidisciplinary finite element analysis environment. Particular emphasis was put on the weight estimation of primary structures undergoing optimisation. The multidisciplinary approach was very useful for the success of the modelling and weight estimation efforts on the High Speed Civil Transport aircraft.

Sensmeier et al. [44] proposed a methodology for rapid and automatic structural model generation based on a parametric description of aircraft structural elements and their layout rather than the actual dimensions. Using this methodology, a finite element model of moderate fidelity based on a parametric structural model can be generated so that, changing the structural model, the finite element model is changed automatically. This model can then be used within an optimisation algorithm to allow sizing optimisation to be performed. Eventually this will result in improved accuracy in weight estimation for new aircraft designs than the one obtained by the empirical-historical data based methods.

Bindolina et al. [45] presented a multilevel structural and multidisciplinary optimisation procedure for the preliminary estimation of the wingbox weight of an aircraft for which empirical formulas and statistical analysis may not be sufficiently reliable. The procedure consisted of three design cycles running on three separate levels. In the first level, a satisfactory behaviour of the wing was

granted by optimising a one-dimensional model based on beam theory. In the second level, by using the internal forces stressing the wing components and a classical wing structure analysis approach coupled with a genetic optimiser, the design and sizing of the wingbox structure was accomplished. In the last level, the finite element model of the wing structure was generated using the data available from previous levels. The procedure was compared to a wingbox weight estimation of a conventional aircraft configuration using classical semi-empirical methods and was then applied to the wing weight estimation of a nonconventional aircraft configuration. In both cases, satisfactory results were demonstrated.

Hurlimann et al. [46] presented a CAD/CAE-based multidisciplinary process for the mass estimation of a transport aircraft wingbox structure. CATIA V5 was used as a multi-geometrical and multi-structural model generator and the interface capabilities of CATIA V5 were used for the generation and application of wing loads. A finite element structural algorithm was used for analysing and sizing the wingbox structure. The process was verified by performing a mass estimation of the wingbox structure of a generic long-range aircraft configuration. Hurlimann concluded that although the proposed mass estimation method that relied on modern CAD/CAE tools showed several advantages while generating and handling the geometrical and structural model of an aircraft wing, there were some disadvantages that severely limited the viability of the CAD/CAE-based approach. Such disadvantages were related to the low computational efficiency and lack of an external programming interface in CATIA V5 that caused multidisciplinary optimisation to be inapplicable. Another disadvantage was related to the use of composite materials, which was not possible in the particular version of CATIA V5 (R19).

Other studies that used an automated model generator for wing mass estimation in the initial phases of the design process were given by Dorbath et al. [47] and Wenzel et al. [48]. A generic numerical modelling process for nonconventional wing configurations was developed by Seywald [49] and a simulation tool for their evaluation and mass prediction was implemented. The wingbox was modelled by a nonlinear finite element beam model coupled with a low-fidelity aerodynamic method, resulting in a quasi-static aeroelastic model that takes into account the redistribution of aerodynamic forces due to deformation. The tool had been validated on a number of conventional aircraft configurations and complex wing configurations such as the C-Wing. The wingbox predicted masses were generally

a little lighter when compared to the reference values. The joined wing concept has been studied by a number of designers since 1986, when Wolkovich [50] published his concept, and since then a number of methods have been developed and reported on the wing mass estimation of joined wing aircraft configurations. Hajela [51], Miura et al. [52], and Blair and Canfield [53] describe different trends and integrated design processes for creating high fidelity weight modelling and estimation techniques realised using the finite element method.

A number of computational tools have been developed for wing mass estimations. These algorithms have been significantly improved over the past few years and their accuracy has increased with recent advances in computer technology. PrADO (Preliminary Aircraft Design and Optimisation Program) is a program that was originally developed by Heinze [54,55,56] at the Institute of Aircraft Design and Lightweight Structures of the TU Braunschweig. PrADO is used for the design and optimisation of the entire aircraft with respect to different aspects, e.g. operational and economical, by the use of a dedicated cost model. This program offers the user either a fast analytical method or a computationally more expensive but high-fidelity finite element based method for the structural analysis and dimensioning of either conventional-configuration aircraft structures or nonconventional configurations such as the blended wing body. MDCAD (Multidisciplinary Concept Assessment and Design) is another program originally developed by QinetiQ for the analysis and optimisation of military and civil aircraft configurations to investigate the impact of new technologies such as novel wing configurations, composite materials and other systems on the design [57,58]. MDCAD makes use of the geometry model generator in CATIA V5 for structural modelling and the finite element solver of MSC.Nastran for structural analysis.

2.3 A Brief Review of Structural Optimisation

There is a large amount of publications on aircraft structural optimisation. A few of these key studies are referenced in this section to provide the reader with some background information on the field. In the 1960s, Brandt and Wasiutynski [59] reviewed the present state of knowledge in the field of optimum design of structures. The survey papers by Schmit [60] and Vanderplaats [61] offer numerous and important references on the theory and applications of structural optimisation. The development of structural optimisation methods can be tracked to the early works of Maxwell [62] and Michell [63].

In the 1940s and early 1950s, substantial analytical work was done on component optimisation, of which the work presented by Shanley [25] is a typical example. Dantzig [64] developed linear programming techniques, and with the advent of computer technology, these techniques were applied to the plastic design of frame and beam structures as explained by Heyman [65]. In his work, Schmit [66] offered a comprehensive study on the application of mathematical programming techniques to solve different types of nonlinear and inequality constrained problems concerned with the design of elastic structures under a variety of loading conditions. This was done by combining numerical optimisation with the finite element analysis methods available at the time.

In the early 1960s, extensive research was done in the area of structural optimisation, and as a result gradient-based optimisation methods were recognised as the most efficient for solving the optimisation problem. However, the continually increasing number of design variables and the increasing size of the finite element models, together with very slow and extremely expensive computers, were the main difficulties facing structural optimisation technology by the end of the 1960s, according to Gellatly et al. [67]. In addition, the discretised optimality criteria methods presented by Venkayya [68], which were based on the early work of Prager and Taylor [69], offered an efficient way of solving problems with large numbers of design variables, but were limited to small numbers of design constraints. Schmit and Farshi [70] published the concept of using approximation techniques for structural synthesis. These techniques resurrected the use of mathematical programming for structural optimisation. Starnes, Jr. and Haftka [71] overcame the difficulties in using approximation techniques for some constraints, such as buckling by introducing the concept of conservative constraints approximations.

During the 1980s, force approximation techniques for stress constraints with intermediate variables began to evolve. These methods would improve the quality of approximate optimisation techniques but were difficult to integrate into existing analysis programs. A key development in making structural optimisation a widespread reality was the work that had been performed in the field of design sensitivity analysis. More information on sensitivity analysis can be found in the book by Haug et al. [72] and the review paper by Haftka and Adelman [73].

2.3.1 Structural Optimisation in the Aerospace Industry

Structural optimisation methods evolved in the aerospace industry in the late 1950s, when the need to design lightweight structures was critical [74,75,76]. Since then, the aerospace manufacturing industry has shown increasing interest in the application of optimisation methods for the optimum design of minimum-weight aircraft structural components [77,78,79]. The survey paper by Venkayya [68] presents an exhaustive review of relevant literature on the structural optimisation of aerospace structures.

In the field of structural design optimisation concepts for aerospace industry, Gerard [80] demonstrates a generalised theoretical methodology for design optimisation and highlighted techniques to achieve optimum designs. Ashley [81] presents a complete analysis of the implementation of optimisation methods in aeronautical engineering. A short review article on the optimisation of wing structures is given by Butler [82]. Rao [83] describes a procedure for the automated optimum design of aircraft wing structures subjected to multiple behaviour constraints. Structural design optimisation has been the objective of numerous investigations in the last few decades and the majority of the work has dealt with isotropic structures. Dababneh and Kayran [84] reviewed the effect of implementation of various structural idealisations on the design, analysis and optimisation of thin-walled semi-monocoque wing structures in the initial design stages. In their study, the effects of assorted one- and two-dimensional finite element pairs and mesh densities on the optimised configurations of the wing structure were investigated.

The optimisation of composite structures, particularly wing structures, was an area of research that has been widely discussed in the open literature. For instance, Starnes, Jr. and Haftka [71] discuss the initial design of composite wings subject to strength, displacement and buckling constraints. One of the first studies on the use of advanced composite materials in forward-swept wings was performed by Krone [85]. Edwin [86] discussed the application of practical optimisation techniques for the forward-swept wing of the Grumman X-29. The chosen criteria for the optimal design problem included minimisation of structural weight under strength and divergence velocity constraints. While Green [87] investigated the influence of non-symmetrical laminates on the aeroelastic behaviour of high aspect ratio wings, Eastep et al. [88] explored the advantages of declaring the ply orientation as a variable in the design of composite structures.

An optimisation study was performed for a composite wing subjected to constraints on strength and aeroelasticity. The study indicated that the optimal design of a composite wing is nearly unresponsive to the orientation of the laminate layup when multiple structural constraints are applied to the wing. Gurdal et al. [89] and Kameyama et al. [90] present stiffness optimisation studies based on expressing the laminate stiffness matrices as a function of the lamination parameters as a result of classical lamination theory. Dillinger et al. [91] demonstrate the stiffness optimisation of the upper and lower skins of a composite wing structure. A feasibility study that addressed the effect of composite tailoring on the aeroelastic stability margins of the composite tiltrotor wing of a V-22 was performed by Popelka et al. [92]. It was concluded that the gain in stability margins was affected by conflicting requirements of the torsional and bending modes of the wing. Lottati [93] investigated the critical flutter and divergence velocities of a high aspect ratio forward-swept wing, idealised by a box beam. His results indicate that the bending-torsion stiffness that maximises the flutter velocity tends to minimise the divergence speed and vice versa. Similar work was demonstrated by Weisshaar et al. [94], who showed in a parametric study of a swept-back wing that the flutter and divergence velocities of the wing are sensitive to a change in the fibre orientation angle.

Other research studies in the aerospace industry tend towards aircraft multidisciplinary design optimisation. Sobieski and Haftka [95] present a survey on the methods that have been used for the modelling of multidisciplinary design optimisation problems. A survey on the architectures of multidisciplinary design optimisation methods is given by Martins and Lambe [96]. Haftka et al. [97] discuss the multidisciplinary optimisation of engineering systems from the viewpoint of the available computational alternatives. They emphasise that the solution procedure is necessarily iterative in nature. Peter et al. [98] illustrated the application of combined aerodynamic and structural optimisation by applying it to the design model of a High Speed Civil Transport wing. The design objectives included achieving minimum structural weight and minimum aerodynamic drag when subjected to strength, torsional stiffness and buckling constraints. Grossman et al. [99] examined the interaction of structural optimisation and aerodynamic of a sailplane wing using a sequential design procedure (aerodynamic optimisation followed by structural weight minimisation). The study showed that integrated aerostructural optimisation gave higher-performance designs with minimum wing structural weight. An integrated

multidisciplinary procedure for structural and aeroelastic optimisation of composite wings using advanced analysis methods was developed by Jha and Chattopadhyay [100]. The goal of the optimisation procedure was to minimise wing structural weight with constraints on flutter/divergence speed and stresses at the root due to static load conditions. A considerably lower wing structural weight and higher flutter dynamic pressure was achieved compared to the selected base design.

A review article of the methods and tools developed and applied at Airbus to deliver automated sizing for aircraft structures over the course of their development is presented by Grihon, et al. [165]. In the first part of their paper, a multi-step sizing process for aeronautical structures is discussed, whereas in the second part, the authors describe sizing processes suited to supporting aircraft development from the early design concept through to the final detailed design.

In the literature, a number of programs were developed to simultaneously handle multidisciplinary optimisation problems with different requirements such as strength, stiffness and flutter. In the mid-1960s, Nastran, the NASA Structural Analysis System, was developed by NASA to provide a finite element analysis capability for its aerospace development [101]. Meanwhile, Nastran has become world recognised standard in the field of structural analysis, offering the designer large variety of modelling tools and analysis disciplines such as structural analysis, elastic stability analysis, and thermal and fatigue analysis. Among other capabilities, Nastran has provided a multidisciplinary design optimisation solution for a wide range of engineering problems faced by the aerospace industry.

In 1975, the Flutter and Strength Optimisation Program (FASTOP) was developed [102]. FASTOP was mainly composed of two sub-programs which were coupled in sequence. The Strength Optimisation Program (SOP) performed a minimum-weight structural design based on a fully stressed design procedure, and the Flutter Optimisation Program (FOP) addressed dynamic analysis requirements to calculate the flutter speed, and performed resizing if required to increase the flutter speed. The Automated Structural Optimisation System (ASTROS) [103] was made to support both the preliminary design stages and modifications that occur later in the product life cycle of an aerospace structure. ASTROS offered a single multidisciplinary automated environment in which to develop improved designs of aerospace structures by combining finite element modelling and analysis techniques with efficient optimisation solutions. In

ASTROS, a wide range of constraints can be imposed on a design, including strength, displacement, flutter and other requirements. There are other examples of specialised programs designed for structural optimisation and aerospace applications, such as the Aeroelastic Design Optimisation Program (ADOP) [104], HyperSizer [105], Altair OptiStruct [106], GENESIS [107] and ANSYS [108].

2.3.2 Optimisation Methods in Aerospace Engineering

Numerous optimisation methods have been developed for problem solving in the field of aerospace engineering. These methods can be classified into two main groups: genetic algorithms and gradient-based algorithms. Genetic algorithms are renowned evolutionary strategies that derive their principle from Darwin's Theory of Evolution and were first introduced by Holland in 1975, as quoted by Goldberg [109]. The first step of a genetic algorithm is to define a set of designs, called a population, which are usually generated randomly. Computing constraints and objective functions (fitness values) then allow evaluation of every population member. In the next step, a selection method, based on the fitness values, is applied to reproduce a new and improved design from the population to form a mating pool. In the final step, a next-generation design is created by applying mutation and crossover operators to the intermediate designs created in the previous step; new designs are arrived at and replace the worst designs in the population. The procedure is repeated until a convergence is achieved and a best design is generated, or else the evaluation step is repeated.

Alternatively, gradient-based algorithms use function gradient information to search for an optimum design. The first step in the numerical search process is to calculate the gradients of the objective function and constraints for a given point in the design space. Once the gradient is computed, there are several options for finding a minimum. For constrained problems, sequential quadratic methods can be used [110], while for unconstrained problems, quasi-Newton methods are effectively used with a line search procedure [111]. As the search direction is determined, the search process continues in that direction and it can be repeated until an optimum solution has been found.

Genetic and gradient-based algorithms have been applied successfully to various aerospace structural optimisation problems. Kogiso et al. [112] applied the genetic algorithm to the stacking sequence design of laminated composite plates to maximise the buckling loads. Liu et al. [113] used an alternative genetic algorithm

to optimise the stacking sequence of a composite wing subjected to strength and buckling constraints. On the other hand, Gwin and Taylor [114] have used a gradient-based feasible direction method for the optimisation of wing structures subject to flutter speed constraint. Karpel [115] used a gradient-based constrained multidisciplinary optimisation method to minimise the weight of an active flexible wing (AFW) subjected to constraints on flutter speed and control stability margins. Furthermore, the gradient-based algorithms available in MSC.Nastran and ASTROS have also been widely used in the stacking sequence design optimisation of composite plates. The laminate is assumed to be made of plies stacked together, and the thickness and/or orientation of the stacks are treated as continuous design variables.

One of the key advantages of gradient-based methods is their efficiency in solving optimisation problems where the design space is significantly large, and the number of objectives and constraints is considerably smaller than the number of design variables. Furthermore, the speed of convergence with a clear convergence criterion and the low computational cost of the analysis are other primary advantages of gradient-based methods. Another feature is that they can stably handle a large number of continuous and discrete design variables, and are known to be very efficient with respect to searching for an optimum solution closest to the starting point in the design space. One often-mentioned disadvantage of gradient-based methods is that they find a local minima rather than a global optimum. However, in many engineering design perspectives this is unlikely to be an issue, since the highly constrained nature of the design problem in aerospace structures inhibits multimodality. Similarly to gradient-based methods, genetic algorithm methods also have some advantages and drawbacks. Genetic algorithm methods can work very well with a generally discontinuous and sufficiently small design space. The possibility of finding a global optimum is higher than for gradient-based methods but not guaranteed, since the genetic algorithm has to evaluate many alternative designs and therefore the computational cost per evaluation increases. A primary disadvantage associated with genetic algorithms is their very slow convergence behaviour due to the number of evaluations required, especially near an optimum. Another limitation is that determining the convergence criteria for a genetic algorithm is not straightforward and must be supplied by the user. Since gradient-based and genetic optimisation methods each have their own strengths and weaknesses, the choice of method is design-dependent for a specific problem class [116].

2.4 Identifying Research Gaps in the Literature

Based on the literature review, several key research gaps have been identified. In this section we briefly highlight these gaps, including the main findings and some specific research questions or key issues that seem to logically flow from the identified gap. The following research gaps have been identified.

1. A vast majority of current wing mass estimation methods are still dependent on traditional approaches that rely on the use of statistical databases of specific classes and types of aircraft, as well as the experience gained from previous projects. These methods are therefore limited to conventional aircraft designs constructed from light metallic alloys, and are unable to assess the relative benefits of novel wing design concepts, such as the box wing aircraft [2,3] and the blended wing body [4,5], or the implementation of new key technologies. Examples of key technologies are advanced materials, such as composite materials and carbon fibre reinforced polymers (CFRP), high aspect ratio laminar flow wings [6,7] and wing configurations utilising high lift device concepts to decrease aircraft noise during take-off and landing [8]. Furthermore, innovative detailed technologies, like the NASA shape-changing wing equipped with novel morphing technology [9], must also be considered.

2. A number of recently modified semi-analytical and newly developed finite element analysis wing mass estimation methods still use a simplified geometrical layout of an aircraft wing that cannot accurately predict the actual material distribution of the wing or the aeroelastic behaviour of the wing structures. For instance, the skin, the stiffeners and the spar caps of the wing are modelled using just one upper and one lower equivalent panel [19]. In another example, the wing torque box is modelled as a simple rectangular beam box [117], ignoring not only the actual aerodynamic shape of the wing but also the internal wing structure design, which usually affects the reliability of the wing mass estimation methods. Unmaintained, the actual aerodynamic shape of the wing will affect the overall accuracy of the aerodynamic load calculation and distribution over the wing, which has a significant effect on the structural sizing process of the wingbox and hence it's mass. Numerous methods have been used to calculate the aerodynamic load distribution by assuming a simplified shear force and bending moment or an elliptical lift distribution based methods. The use of these methods has revealed a significant inadequacy in the existing mass estimation methods for predicting

a reliable result. Ignoring the internal wing structure design will affect the structural behaviour of the wing torque box, as the primary load-carrying structure, by having a significant effect on the accuracy of the moment of inertia and stress calculation values for each section of the wing. This will have an impact on the structural analysis technique used to size and estimate the wing structural mass components. Furthermore, it will affect the investigation of the advantages of using novel wingbox design concepts like the curvilinear SpaRibs [118] and grid structure [119] concepts in comparison with classical design concepts.

3. Some modern multidisciplinary optimisation methods were used to estimate the structural mass of the wing. Different wing mass estimation results were obtained depending on the utilised fidelity levels of the optimisation solvers and the design analysis discipline used, mainly aerodynamic and structure. A better understanding and application of optimisation methods is needed in order to make the best use of them as one of the most promising methods in wing mass estimation, especially where novel concepts and materials are elements of the design process. The accuracy and stability of the optimisation results depend crucially on the following points:

    - the quality of the finite element wing model, consisting of a well-defined and realistic shape of the wing structure model;
    - accurate calculation and representation of the aerodynamic loads;
    - reasonable design requirements and practical design variables and constraints.

4. A large variety of software packages have been developed for wing mass estimation by different leading aircraft manufacturers and aeronautics and space research centres. These computational tools are mainly developed using in-house software [165,166,167], making them inaccessible for public use and limited to use by the developer company only.

Chapter 3

Design Methodology

In this chapter, an overview of the wing mass estimation approach for conventional aircraft is given, and modified as necessary to accommodate the implementation of key technologies in recent aircraft designs. Then, a methodology for determining the mass of a transport aircraft wingbox structure using Multidisciplinary Design Optimisation (MDO) is presented. The design and analysis tools employed in this study are also discussed.

3.1 Overview

The conventional approach to aircraft wing mass estimation at the early stages of the design process is mostly based on statistical data from previously investigated or constructed aircraft of the same type and manufacturer. Historically, determining the mass of an aircraft wing for which the database is insufficient or non-existent has been limited to two very expensive methods:

- detailed finite element modelling and analysis of the aircraft wing structure, integrated with a corresponding knowledge of the as-built structural design and manufacturing process definition [40,43];

- design and construction of aircraft wing prototypes.

The use of finite element models for aircraft component structural design and mass estimation was always considered by the aerospace industry as a costly

approach in terms of time and resources. Compared to the first approach, the construction of prototypes is considered even more expensive, especially for large transport and military aircraft. However, new technology in computer processors, recent advancements in computer-aided design, finite element analysis software and optimisation techniques have paved the way not only for possible reconsideration of the first approach, but also for the development of multidisciplinary integrated design optimisation methods and tools for the mass prediction of transport aircraft wings.

3.2 Technical Approach

The goals of the present research are mainly twofold. The first is to create a multidisciplinary analysis and design optimisation framework that can be used for the mass estimation purposes of aircraft wing structures. The second is to use the framework to study the effects of introducing new technologies, such as composite materials and/or new design requirements, including but not limited to structural strength and stiffness, aeroelastic instabilities and manufacturing requirements.

This approach is preferred due to the strong interaction between the different disciplines involved in the wing mass estimation process. Therefore, the framework needs to give sufficiently accurate results within acceptable computational time and input efforts. The framework needs be flexible so that the design objective, design variables and design constraints can be easily chosen or changed. Furthermore, the framework needs to be in an environment that allows for fast and easy changes to the MDO formulation. It also has to allow the designer to assess and understand the structural behaviour of the wing at an early stage of the design process, thus eliminating any costly changes during the aircraft development programme [121].

The design methodology consists of five key components, as shown in Figure 3.1. Once the technical data and specifications of a viable aircraft have been identified, the design process can be initialised. For each design module, it is useful to consider what the main inputs and outputs are and what design assumptions can be used as a last resort where necessary information is either not accessible or does not exist. These shall be discussed in more detail as the design methodology is applied to examples of aircraft design in Chapters 4, 5 and 6.

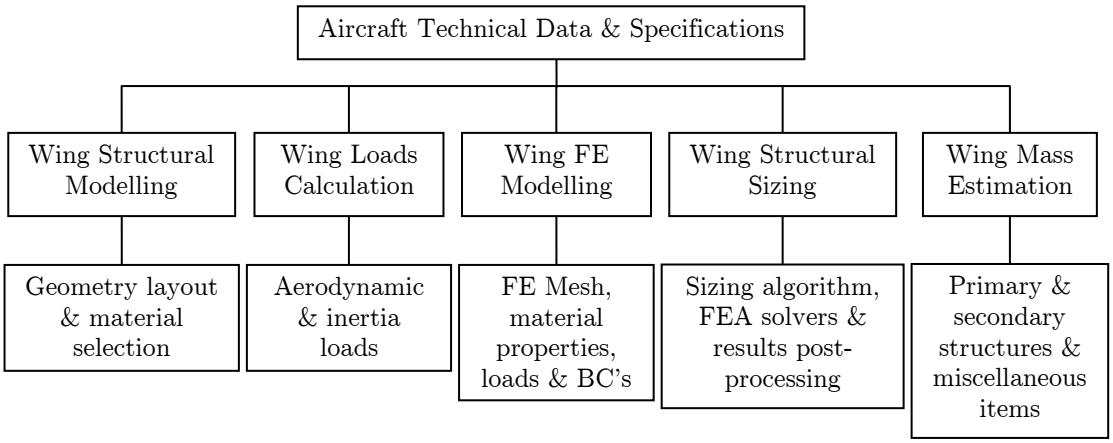

Figure 3.1: Flow diagram of the key components of the design methodology

In a conventional aircraft design process, wing mass property design engineers usually follow a particular published methodology, such as one of those proposed by Raymer [12], Roskam [13] or Torenbeek [14]. In these methodologies, the total wing mass comprises the mass of the primary wing structures, the secondary wing structures and miscellaneous items. Taking up as much as 35-50% of the operating empty weight of modern transport aircraft [120], the wing is one of the heaviest structural components of an aircraft. Therefore, special attention has to be focused on the accurate mass estimation of the wing. Figures 3.2 and 3.3 show the planform and mass breakdown, respectively, of a conventional transport aircraft wing.

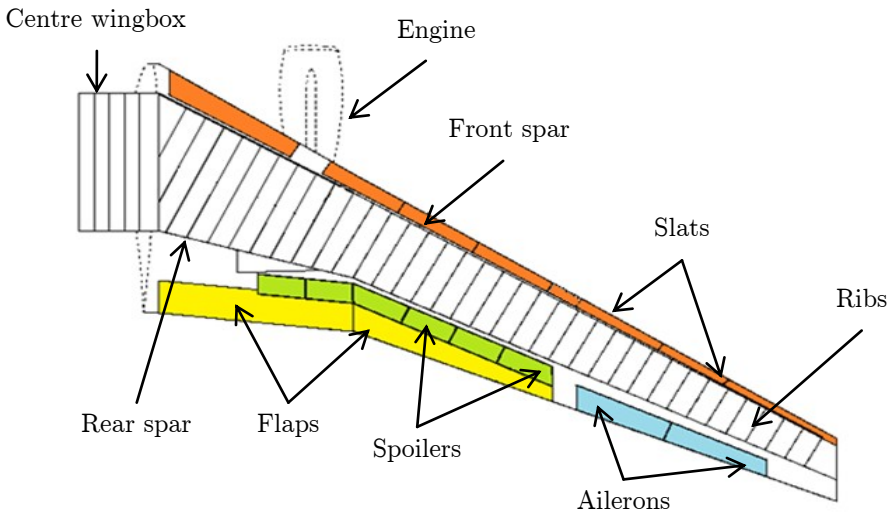

Figure 3.2: Wing planform of a conventional transport aircraft

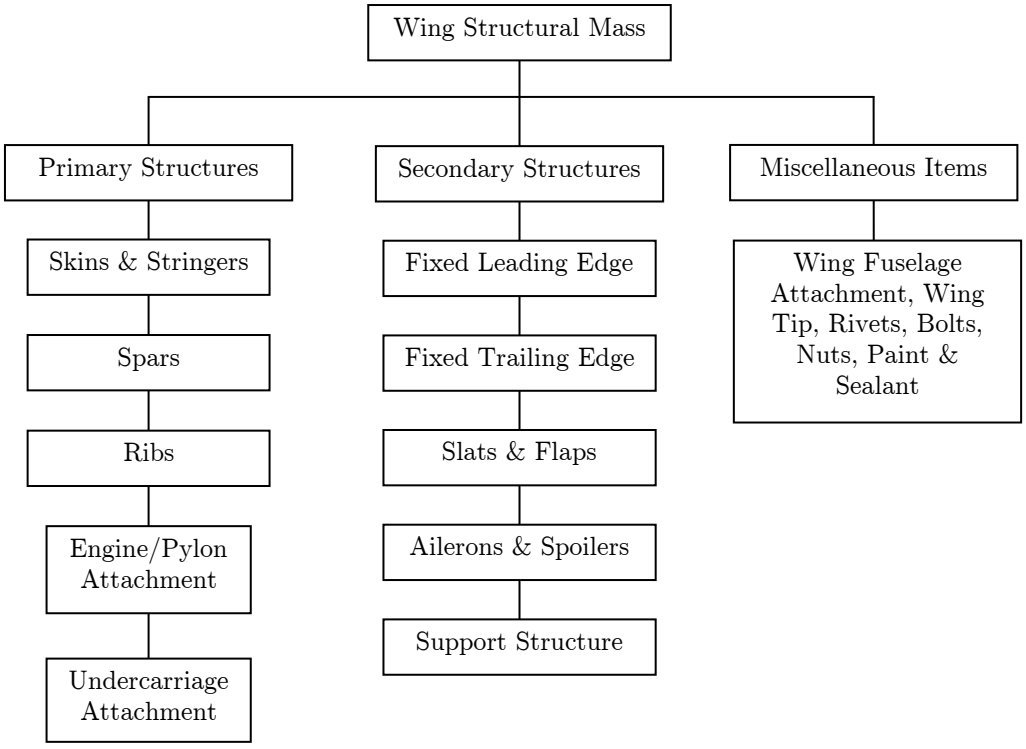

Figure 3.3: Wing mass breakdown of a conventional transport aircraft

3.2.1 Wing Structural Modelling

The aircraft wing is defined using several input parameters, such as the wing semi-span length, the chord length at the wing root, kink and tip locations along the span, airfoil shape and properties, wing sweep, and dihedral and geometric twist angles. Three spanwise locations, the wing root, kink and tip, are used to define the shape of the wing planform. The locations of the front and rear spars define the wingbox and the positions of the ribs define the internal wing structure. The geometry of the wing remains fixed during the sizing optimisation.

In this study, the main load-carrying wing structure is created using different structural models of increasing complexity, and comparative effectiveness studies are conducted to identify and select an appropriate model that can be used to predict the mass of the primary wing structure to an acceptable level of accuracy. Metallic and composite materials have been used as the main construction materials for the wingbox structural elements and their benefits have been investigated during the design and optimisation process.

3.2.2 Wing Loads Calculation

There are currently several theoretical methods available for determining the aerodynamic loading of an aircraft wing. Many of the theoretical solutions have been programmed for digital computation, and separate computer programs were used to calculate the aerodynamic forces on the aircraft wing in different flow conditions. The choice of the appropriate method depends on the complexity of the aircraft wing, the purpose of the analysis, the computational cost and the level of accuracy required at the design stage. In this study, ESDU 95010 [122], a software package for the calculation of spanwise loading of wings with camber and twist in subsonic attached flow is used, and the Tornado VLM code [123] implemented in MATLAB, a three-dimensional Vortex Lattice Method software package for linear aerodynamics, is used to validate the results calculated by ESDU 95010. The aerodynamic loading resulting from the most critical aero-load scenario is considered for sizing the wingbox.

The inertia load relief of the fuel masses, located in the aircraft wing's internal fuel tanks, the wing mounted engine and mounted main landing gear, as well as the inertia relief due to the wingbox structural mass and the wing secondary structures (including the leading and trailing edge wing components, flaps, slats, spoilers and ailerons) are automatically accounted for during the finite element analysis and sizing optimisation process by applying the correct acceleration vector with respect to the assumed flight manoeuver of the aircraft.

3.2.3 Wing Finite Element Modelling

In general, various finite element types could be used to model and analyse aerospace structures; however, the appropriate use of element types is closely related to the loading type that the structure is carrying and the complexity of the structure. In the current study, the thin-walled structures of the wingbox configurations (skins, spar webs and ribs) were modelled using two-dimensional quadrilateral and triangular shell elements (CQUAD4 and CTRAI3) having in-plane membrane and bending stiffness. On the other hand, stiffeners and spar caps were modelled using one-dimensional rod elements (CROD) having axial stiffness.

The non-structural masses are modelled using concentrated lumped masses. These were introduced to the wingbox finite element model at their correct position

using appropriate multi-point constraint elements (RBE3 and/or RBE2). The aerodynamic loads were also introduced to the wingbox finite element model using RBE3 at their pre-defined location. To define wingbox realistic boundary conditions, spring elements (CEALS1) are combined with RBE2 elements. Material and element properties were also assigned to the wingbox finite element model.

The wingbox finite element model has been verified by numerous quality pre-analysis checks, including element free edge, mesh and element quality, boundary conditions, coincident nodes, material and element properties, and element normal. Finite element model checks help to safeguard against fundamental errors, and also guard against the frustration associated with having the solver run for a considerable amount of time, only to abort due to incorrect or missing data.

3.2.4 Wing Structural Sizing

In most of the wing mass estimation methods, the primary and secondary wing mass structures are calculated independently. Therefore, in order to develop an effective and efficient sizing process, a multidisciplinary analysis and design optimisation framework has been used to calculate the mass of the wing primary structural components based on finite element modelling and analysis methods. For the MDO formulation, the objective function selected is to minimise the structural mass of the wingbox. The set of design variables and design constraints are also defined, and there are differences between the metallic wingbox and the composite one. Gradient-based optimisation algorithms available in MSC.Nastran are utilised for this study. Once the mass of the wingbox is calculated, the wingbox structural components can be calculated using the post-processing capabilities of MSC.Patran. The engine/pylon and undercarriage attachment masses are estimated using the empirical equations available in [12,13].

The mass estimation of the wing secondary structures is generally more difficult than the wing primary structures. Despite the fact that wing secondary structures, like the leading and trailing edge devices, are common features of every modern aircraft, the choice of them is crucial and depends mainly on their aerodynamic and aeroacoustic performance. In the initial phases of the design, the detailed high lift device layout is usually unknown, and the structural sizing of the leading and trailing edge devices based on finite element modelling is not

applicable. Thus, the mass of the wing secondary structures can be calculated using the semi-empirical and analytical equations of Torenbeek [21], as used in this study, or by using regression analysis of existing aircraft of the same weight and type and tuning it to account for secondary structural mass. Finally, the total mass of the miscellaneous items is assumed to be 3.75% of the total calculated wing mass [34]. The total mass of the wing is calculated as the summation of the primary wing mass, the secondary wing mass and the mass of miscellaneous items.

3.3 Design and Analysis Tools

MSC.Patran [156], which is commonly used both in industry and in academia as a pre- and postprocessor, is used in the current study for creating the wing geometry, the wingbox structure and the finite element models. MSC.Nastran [138,145] is utilised as a finite element analysis solver (Sol 101 linear static; Sol 103 normal modes) and as a sizing optimiser (Sol 200).

For aeroelastic modelling, the MSC.FlightLoads and Dynamics module [143,144] is used. Flutter analysis and optimisation requirements of the wingbox require the use of the Doublet Lattice Method (DLM) for the computation of unsteady aerodynamics to perform flutter analysis (Sol 145) using the *p-k* method.

MATLAB R2013a [164] is used to run Tornado VLM code which is used to compute and validate aerodynamic loads calculated by ESDU 95010 program.

Chapter 4

Structural Design of the Common Research Model Wingbox

This chapter is dedicated to the structural design process of a typical transport aircraft wingbox model using the design tools and methodologies described in Chapter 3. The public domain NASA wing, commonly referred to as the Common Research Model, is used as a baseline model.

4.1 Technical Description of the CRM Wing

In this study, the public domain NASA wing [10,11], commonly referred to as the Common Research Model (CRM), is used to demonstrate the applicability and accurateness of the wing mass estimation methodology presented in Chapter 3. The CRM is a modern single-aisle transport-class aircraft configuration that was generated as an open geometry for collaborative research within the aerodynamics community. It has a wingspan of 58.76 m, a mean aerodynamic chord of 7.0 m, an aspect ratio of 9.0, a taper ratio of 0.275, a leading edge sweep angle of 35°, a break along the trailing edge at 37% of the semi-span (also referred to as the yehudi break), a wing tip chord of 2.73 m, a wing root chord of 13.56 m and a cruise Mach number of 0.85. The maximum take-off mass (MTOM) and maximum zero fuel mass (MZFM) are set to 260,000 kg and 195,000 kg using the conceptual design formula from [12], and the mass of the main landing gear and engine are estimated according to [12,124] as 9,620 kg and 7,656 kg, respectively. The maximum fuel mass carried in each wing is taken as 65,728 kg [10]. The

maximum cruise speed limit is set to V_C = 193 m/s EAS with a cruise Mach number of M_C = 0.85. The dive speed is set to V_D = 221.7 m/s EAS with a dive Mach number of M_D = 0.92, which results from the equation $M_D = M_C + 0.07$ given in [125]. The cruise altitude is taken as 10,668 m. The geometry configuration of the CRM aircraft, the planform of the wing and the relevant aircraft data are presented in Figures 4.1 and 4.2 and Table 4.1, respectively.

Figure 4.1: CRM aircraft geometry configuration

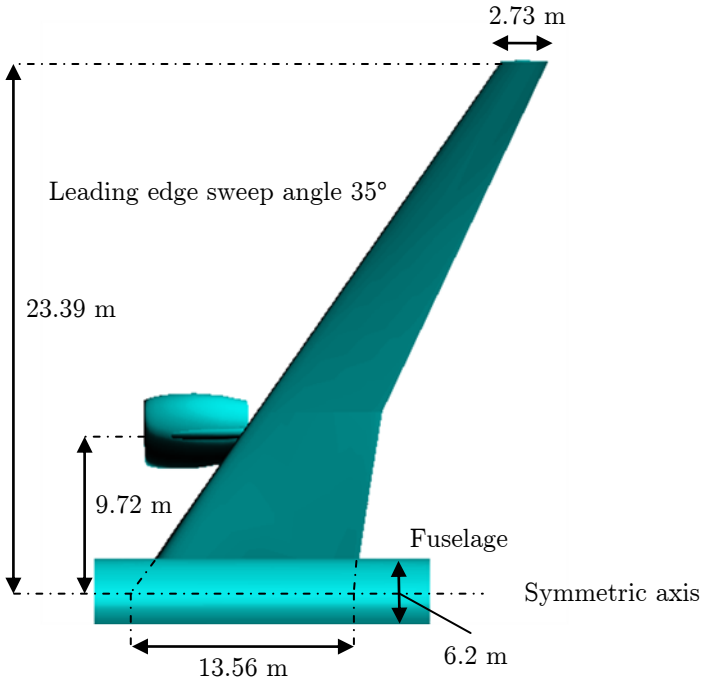

Figure 4.2: Planform of the CRM wing

Table 4.1: CRM aircraft relevant data

Description	Value
Max. take-off mass	260,000 kg
Max. zero fuel mass	19,500 kg
Main landing gear mass	9,620 kg
Engine mass (2x)	15,312 kg
Max. fuel mass	131,456 kg
Wing gross area	383.7 m^2
Wingspan	58.76 m
Aspect ratio	9.0
Root chord	13.56 m
Tip chord	2.73 m
Taper ratio	0.275
Leading edge sweep	35.0°
Cruise speed	193.0 m/s EAS
Dive speed	221.7 m/s EAS
Cruise altitude	10,668 m

The geometry of the CRM wing corresponds to the 1g twisted flying shape at particular flight conditions. Figure 4.3 shows the CRM wing twist distribution from the side-of-body to the wing tip [126]. In this study and since the original jig shape of the CRM wing is not available, the flying shape was used as the jig shape for structural strength and stiffness design and analysis. However, the CRM wing sections were rotated to create untwisted wing geometry for dynamic aeroelastic stability (flutter) analysis.

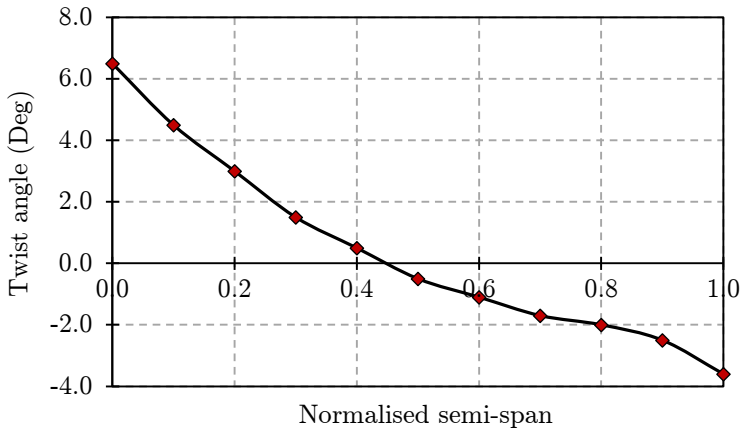

Figure 4.3: CRM wing twist distributions

4.2 Structural Modelling of the CRM Wingbox

During the preliminary design stage of an aircraft wing structure, several theories can be employed to design and analyse the wingbox structure. Euler-Bernoulli beam theory and shell theory are among those discussed in major aircraft structural design reference books [127,128,129]. Different accuracy levels in the results (stress, displacement and mass estimation) can be reached using these theories, depending on the assumptions they were developed on, their application area and the specific type of loading. In beam theory, beam-like structure models were used to represent the primary wing structural components and for calculation of the displacements and stresses. During the design structural analysis it was assumed that the wing could be analysed like a beam with axial, bending and torsional stiffness. Modelling a wing torque box as a beam model is often used in the pre-design stage of a high aspect ratio wing, which is characterised as being very long and slender. The beam model provides valuable insight into the stress state and global behaviour of the structure.

The theory of shell structures has been applied to the structural design and analysis of thin-walled semi-monocoque airplane wings and fuselage skin structures. Reinforcement of thin-walled shells with stiffeners is one of the techniques used by the aerospace industry to manufacture lighter structures and to prevent various failure modes and structural stability problems. The design process is based on the assumption that thin-walled shell members are much thinner than the next larger dimension, and mainly carry either shear loads only or shear plus axial loads, whereas reinforcements primarily take axial loads. A comparison study between beam theory and shell theory for application to wingbox mass estimation at the preliminary aircraft design stage can be found in [117]. In the study, the difference between the two theories in terms of the values of local normal stress, shear and von Mises stresses are analysed for a range of simple wing geometries and load cases. The difference between the two theories in bending, in twist around the wingbox beam axis and in twist in flight direction is also investigated. For more advanced aeronautical structures such as swept wings, finite element computations based on thin-walled shell structure theory are now widely available for stress analysis and sizing of complex structures, thanks to the advent of computer processing technology and finite element simulation methods. Using finite element methods, remarkable improvements relating to the accuracy of torsion, bending and stress computations could be achieved.

4.2.1 Description of the Considered Structural Models

In this study, the main load-carrying wing structure is created using different models of increasing structural fidelity, as shown in Figures 4.4, 4.5, 4.6 and 4.7. The main goal is to identify and select an appropriate model that can predict the mass of the primary wing structure to an acceptable level of accuracy. This done by conducting comparative effectiveness studies that aim to investigate the effects of using different wingbox configurations on the definition of the analysis and optimisation models, and therefore on the total wing mass estimation. Moreover, the aim is to achieve a better understanding of the actual structural material distributions in terms of thickness and orientation when performing size optimisation, and finally to assess the structural behaviour of the wing, including global displacement and local stresses.

1. Wingbox Section Model 1

In this model, as shown in Figure 4.4, each bay in the wingbox is modelled by four un-stiffened thin-walled panels. These panels represent the upper and lower skins of the wingbox, as well as the front and rear spar webs. The thicknesses of the panels are treated as independent design variables representing the wing torsion box and contributing to bending strength properties.

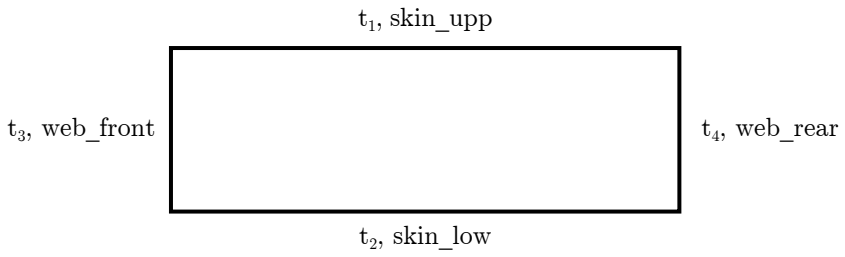

Figure 4.4: Wingbox section Model 1 and related design parameters

2. Wingbox Section Model 2

This model, as shown in Figure 4.5, retraces the previous one and considers the rib thickness as a fifth independent design variable. The number of ribs and their spacing is determined from previously acquired knowledge and evidence from other engineering designs. The ribs and their spacing must maintain the aerodynamic shape of the wing and provide enough clearance through the access hole between each rib section for inspections and maintenance throughout the

operational life of the aircraft. A better evaluation and understanding of the wingbox in-plane and out-of-plane stiffness and bending requirements is hoped to be gained using this model.

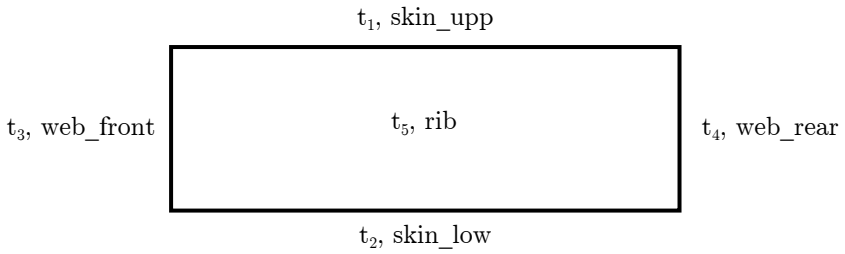

Figure 4.5: Wingbox section Model 2 and related design parameters

3. Wingbox Section Model 3

Four additional independent design variables are added to the third model: upper and lower spar caps are added to the front and rear spars, as illustrated in Figure 4.6. The spar caps take most of the loads from the bending moments, and due to the presence of the spar web, one cap experiences a tension force while another undergoes compression. The spar caps' cross-sectional areas are usually large and vary along the wing.

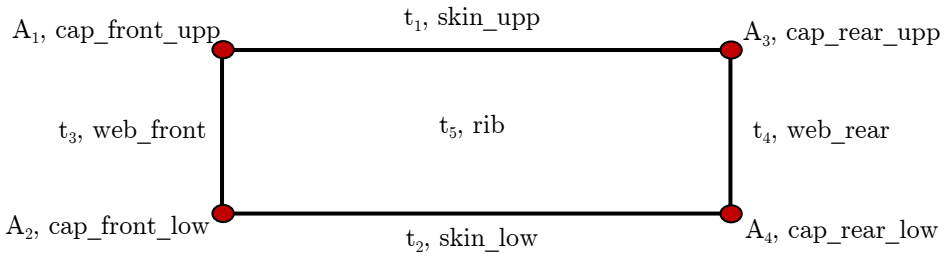

Figure 4.6: Wingbox section Model 3 and related design parameters

4. Wingbox Section Model 4

Stiffeners are added as new independent design variables to the previous model, as shown in Figure 4.7. They are used to support the skin between the ribs and to account for the instability of the thin-walled panels. The stiffeners are also used to resist the part of the bending moment which is not resisted by the spar caps and to take some of the tension and compression loads with effective skin areas. The number of stiffeners and the distance between them is determined from previous design experience.

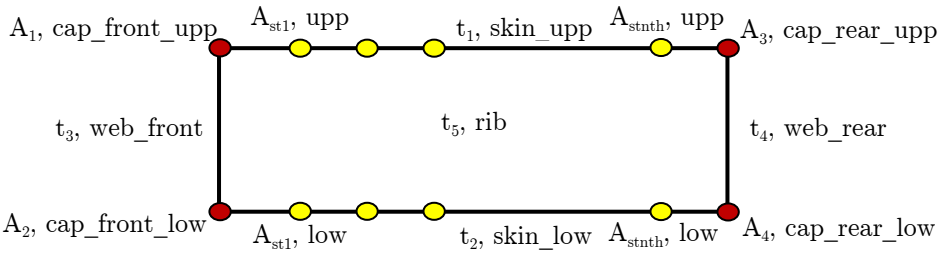

Figure 4.7: Wingbox section Model 4 and related design parameters

4.2.2 Structural Modelling and Layout of the CRM Wingbox

The CRM primary wing structure is modelled to meet the minimum design requirements set forth in the Federal Aviation Regulations (FAR) Part 25 [130] and/or the European Aviation Safety Agency (EASA) CS-25 [125]. Traditional two-spar wingbox architecture is used as a baseline design. The external geometry is defined by CRM.65-BTE airfoil sections and the wingbox is derived from the wing surface model by defining the front and rear spar positions at 12% and 71% of the local airfoil chord. The internal layout is defined by the stiffener pitch, rib pitch and orientation based on the values for a typical large transport aircraft wing. Figure 4.8 shows the CRM wing surface model and the wingbox derived from it.

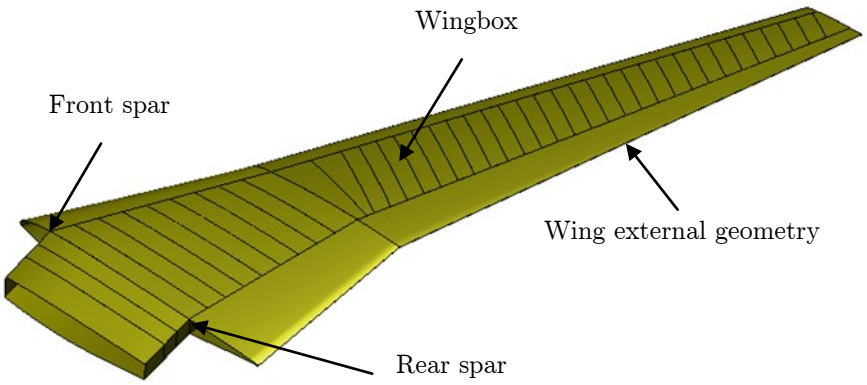

Figure 4.8: Surface and wingbox model of the CRM wing

Figure 4.9 illustrates the design of the CRM wingbox using different models of increasing number of structural components and detail, as described in Section 4.2.1. A number of the wing upper panels were removed to give a good view of the wingbox interior layout.

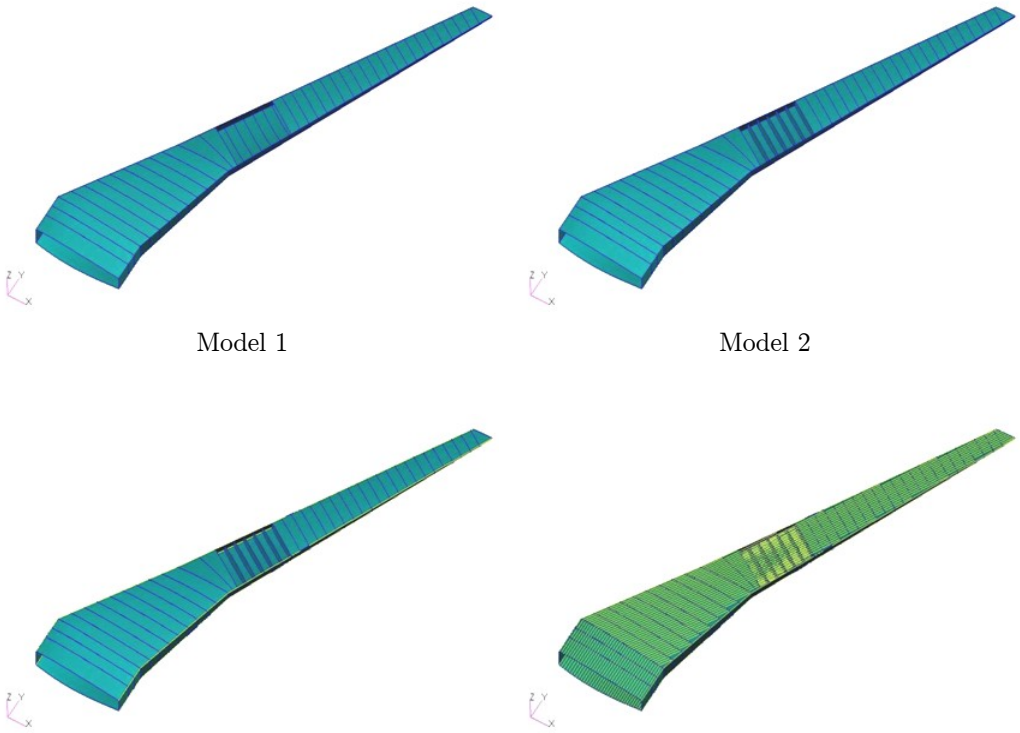

Model 1 Model 2

Model 3 Model 4

Figure 4.9: CRM wingbox models of increasing structural complexity

4.3 CRM Wing Loading Calculation

The loads imposed on a generic aircraft wing are generally dominated by the flight loads, which include aerodynamic loads, gust loads and inertial loads resulting from the wing structural mass, the mass of the secondary structures, the distribution of fuel in the internal wing fuel tanks, concentrated loads of wing-mounted engines and landing gears. Ground loads might also be considered, and loads due to landing, taxiing and towing could be taken into account.

4.3.1 Critical Design Loads

Aircraft wings are frequently subjected to a range of static and dynamic loads resulting from flight manoeuvers and gust encounters. These load cases are accountable for the critical design loads over the aircraft wing structure and therefore affect the structural design and mass estimation. These loads should be determined considering the maximum limit load factors of flight manoeuvers and gust conditions for a particular class and type of aircraft, in accordance with the standard airworthiness certification regulations [125,130]. Figure 4.10 shows a typical V-n diagram for a large transport-type aircraft. The limit loads are defined as the maximum loads expected during an aircraft's service life. The wingbox structure must be able to support limit loads without permanent deformation. On the other hand, the ultimate loads are defined as the limit loads multiplied by a safety factor. In FAR Part 25 and EASA CS-25, the safety factor is defined as 1.5. The structure must be able to withstand the ultimate load for at least 3 seconds without failure.

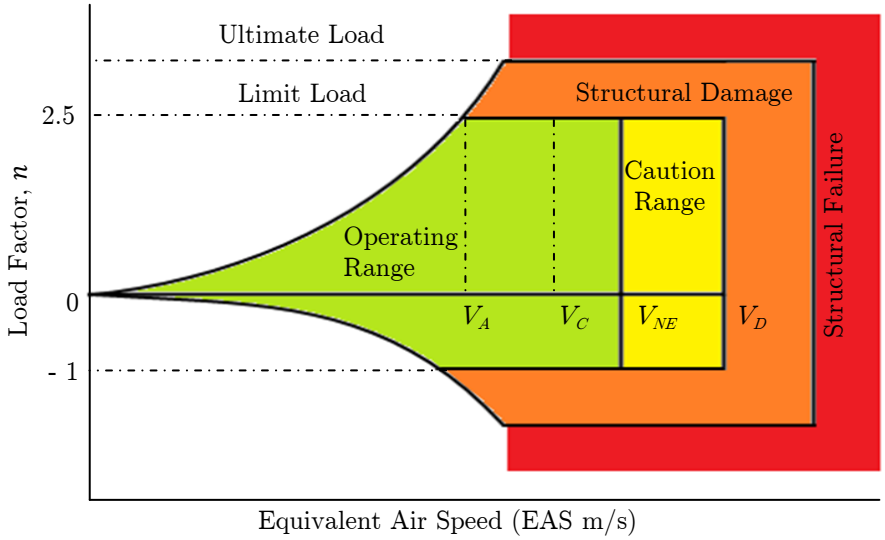

Figure 4.10: V-n diagram for a typical large transport aircraft

There is a large number of possible combinations of external loads to which an aircraft wing might be subjected during different flight manoeuvers and gust conditions. This number can be reduced by considering only the most critical flight scenarios that an aircraft can expect in normal flight operations and procedures. Experience accumulated over many years of design, analysis and study in the field of aircraft wing design has led to the identification of typical

design scenarios that are considered critical in accordance with standard aviation certification regulations [125,130]. A set of procedures have to be followed in order to determine the design load factors and define the related airspeeds, flight altitudes and aircraft weights for which the critical design loads are evaluated. For a large transport aircraft, these procedures are given in the FAR Part 25 and EASA CS-25 regulations. Thus, for the CRM wing, the design loads are obtained from two scenarios, related to flight manoeuvers and gust conditions:

1. symmetric pull-up manoeuver load for the maximum positive limit load factor at maximum take-off mass and maximum dive speed, V_D, at sea-level standard atmospheric conditions;

According to FAR Part 25 and EASA CS-25 regulations, the maximum positive manoeuver limit load factor for a transport aircraft becomes:

$$n = 2.1 + \frac{24{,}000}{MTOM + 1{,}000}. \tag{4.1}$$

where $MTOM$, is the maximum take-off mass of the aircraft, with n limited to $2.5 \leq n \leq 3.8$.

2. gust loads for the maximum gust load factor at maximum zero fuel mass and maximum cruise speed, V_C, at a critical gust altitude of 6,100 m.

The gust loads depends on altitude, the speed and the weight of the aircraft. The most critical altitude for gusts is 6,100 m since the gust speeds are constant until this altitude and then start to decrease with increasing altitude. According to FAR Part 25 and EASA CS-25 regulations, the gust load factor is calculated using the following equation:

$$n_g = 1 + k_g \frac{\rho_c \; U_{de} \; V_{EAS} \, C_{L,\alpha} S}{2 \; MZFW}, \tag{4.2}$$

in which, n_g is the gust load factor, ρ_c is the air density at the critical altitude and equal to 0.653 kg/m^3, U_{de} is the gust velocity at the critical altitude and is equal to 15.25 m/s, V_{EAS} is the equivalent cruise speed, $C_{L,\alpha}$ is the lift curve slope, S is the reference wing area and $MZFW$ is the maximum zero fuel mass.

The gust reduction factor k_g is calculated as:

$$k_g = \frac{0.88\,\mu_g}{5.3 + \mu_g}. \tag{4.3}$$

The mass parameter μ_g is calculated using the following equation:

$$\mu_g = \frac{2\,MZFW}{\rho_0\,\bar{c}\,S\,C_{L,\alpha}}. \tag{4.4}$$

Here, ρ_0 is the air density at sea level altitude, $\bar{c}$ is the wing mean aerodynamic chord, $C_{L,\alpha}$ is the lift curve slope, S is the reference wing area and $MZFW$ is the maximum zero fuel mass.

The load case that produces the maximum design loads is considered as the critical one for the design, analysis and sizing optimisation of the CRM wingbox and hence the mass estimation.

4.3.2 Aerodynamic Loads

There are currently several theoretical methods available for determining the aerodynamic loading of an aircraft wing. Many of the theoretical solutions have been programmed for digital computation, and separate computer programs have been used to calculate the aerodynamic forces on an aircraft wing in different flow conditions. The choice of the appropriate method depends on the complexity of the aircraft wing, the purpose of the analysis, the computational cost and the level of accuracy required at the design stage.

In the current study, the aerodynamic loads are calculated with two different programs in order to ensure the versatility and accuracy of the tool. Two existing aerodynamic codes are used for this work, including the ESDU 95010 computer program and the Tornado VLM code implemented in MATLAB. This is probably a rather simplistic view compared to that from an industrial design perspective. ESDUpac A9510 utilises steady lifting-surface theory based on the Multhopp-Richardson solution to calculate the spanwise loading of wings with camber and twist in subsonic attached flow. The spanwise loading distributions of local lift and pitching moment are calculated as a function of incidence, under the conditions of camber at zero incidence, and twist at zero incidence. The loadings

can be obtained individually or simultaneously. The overall loading distribution can be calculated for a specified incidence or total lift coefficient [122]. The Tornado VLM code [123] implemented in MATLAB is a three-dimensional Vortex Lattice Method software package for linear aerodynamics. Modern aircraft of almost any type can be defined using Tornado software package, including those with multiple wings, both cranked and twisted, and multiple control surfaces. Each wing may have taper of both the camber and the chord. The Tornado VLM code solves for forces and moments, from which the aerodynamic coefficients are computed. Although it is beyond the context of this research to go into details of the theoretical backgrounds of the ESDU 95010 and Tornado VLM methods for calculating aircraft wing aerodynamic loads, the reader may wish to refer to a number of references on lifting-surface theories and vortex lattice methods in [131,132].

The symmetric pull-up manoeuver at the limit load factor ($n = 2.5$) at maximum take-off mass (260,000 kg) and design dive speed (V_D = 221.7 m/s EAS, M_D = 0.65) at sea-level conditions was found to be the critical design load case. The spanwise lift force and pitching moment were calculated at the angle of attack (α_{dive} = 0.5°) at design dive speed. The angle of attack at the dive speed is calculated using the following equation that defined the lift force as:

$$L = nW = \frac{1}{2}\rho V^2\left(C_{L,0} + C_{L,\alpha}\alpha\right)S. \tag{4.5}$$

where L is the lift force, n is the limit load factor, W is the maximum take-off weight, ρ the air density at the required altitude, V the design speed, $C_{L,0}$ is the zero angle of attack lift coefficient, $C_{L,\alpha}$ is the lift coefficient slope, α is the angle of attack and S is the reference wing area.

Figures 4.11 and 4.12 give the local overall lift and pitching moment coefficients calculated about a local quarter chord.

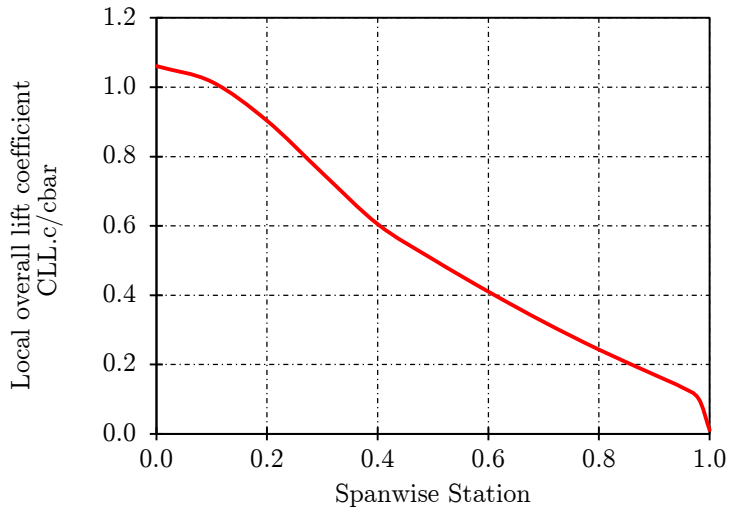

Figure 4.11: Spanwise local overall lift coefficient

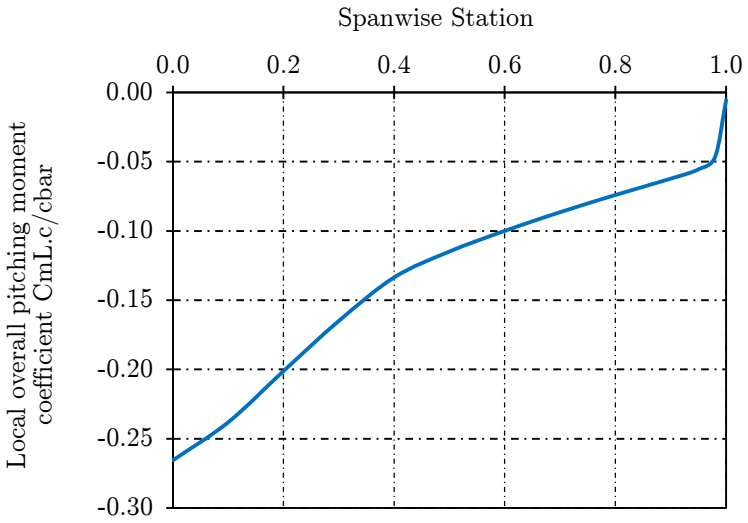

Figure 4.12: Spanwise local overall pitching moment coefficient

4.3.3 Fuel, Engine and Undercarriage Loads

In almost all modern transport aircraft, the fuel for the flight mission is carried in the airplane wing's internal fuel tanks. Usually there are three fuel tanks, one centre tank in the centre wingbox, and two others located within the inner and

outer wingbox structures. During steady level flight manoeuvers, fuel loads result in wing load alleviation and provide inertial relief, thus leading to a decrease in the total wing loads. For the given fuel mass of the CRM aircraft, the maximum capacity of the fuel tanks and their centre of gravity data are calculated using the wing 3D geometrical model for each wing section. Then, the masses corresponding to the fuel are distributed proportionally to the volume of each wing section at the centre of gravity and along the wing model up to 85% of the total span [45]. The fuel mass distribution varies as the fuel is consumed during a flight mission and usually the fuel in the inboard tanks is used up before the fuel in the outboard tanks. Thus, it is important to consider different defuelling scenarios in order to evaluate the maximum inertia load relief contribution due to fuel consumption on the wing structural mass estimation process. Figure 4.13 gives the layout of the fuel tanks and the fuel distribution for the CRM wing.

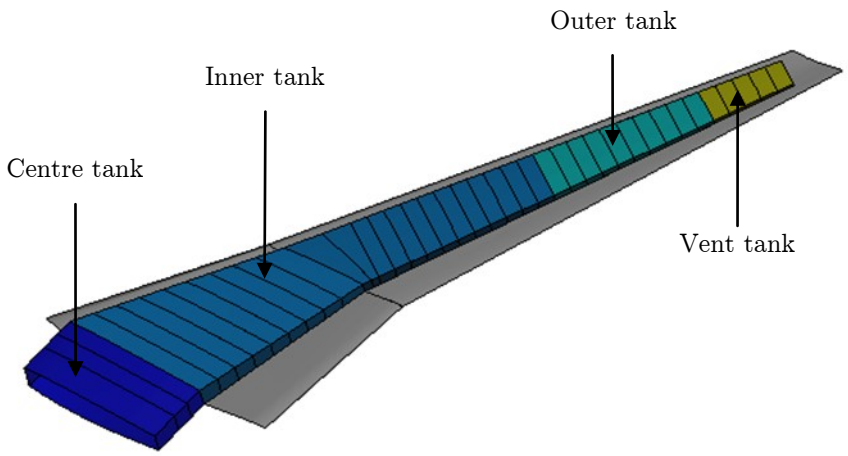

Figure 4.13: Fuel tank layout and fuel distribution in the CRM wing

The inertia load relief due to the CRM wing-mounted engine and wing-mounted landing gear leads to a similar effect as experienced with fuel loads. According to Torenbeek [14], the engine and landing gear masses can cause unfavourable complex wing flutter characteristics depending on the locations of their centres of gravity with respect to the wing elastic axis. The influence of the engine mass on flutter speed and frequency of the aircraft wing is considerably more important; therefore, in order to account for this effect more precisely, a simplified structural model was used to achieve practical engine pylon-to-wingbox connections, as shown in Figure 4.14. Mounting front and aft fittings are used to connect the pylon structural model to the wingbox structure.

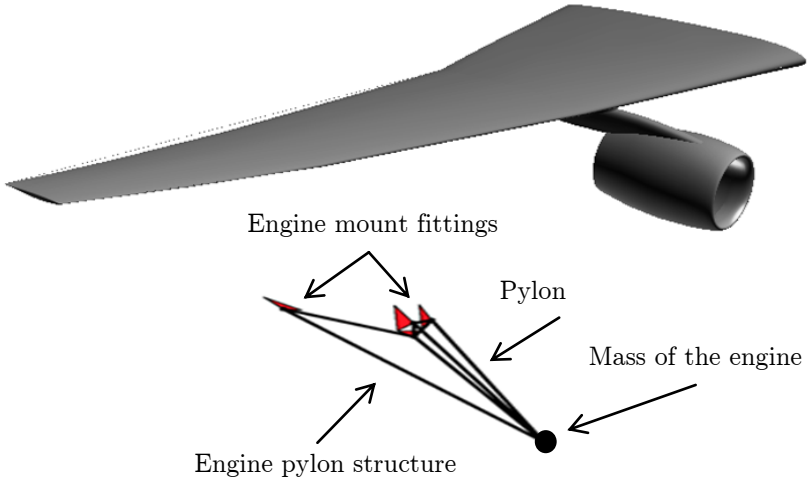

Figure 4.14: Engine pylon-to-wingbox structural connections

4.3.4 Primary and Secondary Structural Loads

The wingbox structural mass as well as the secondary masses, which include the leading and trailing edge wing components, flaps, slats, spoilers and ailerons, also lead to reduction of the wing loads. In order to evaluate the inertia loads caused by the secondary structures, the mass of their components is calculated using the semi-empirical and analytical equations of Torenbeek [21], which provide a component mass estimate based on the corresponding surface area.

4.4 Materials Selection for the CRM Wingbox Design

The complexity of an aircraft wing structure is affected by specific requirements imposed on the design. The initial requirements of the strength-to-weight ratio and the preferential directions of the applied loads will influence the choice of materials during the design of the wingbox structural components. Aerodynamic efficiency, fuel consumption and noise reduction are other design aspects that may be improved by considering new materials.

As a result, the wing of the CRM aircraft is designed by considering both metallic and composite materials, which have a high strength-to-weight ratio for lightweight structures, high strength and stiffness properties, good fatigue and corrosion resistance. High-strength aluminium 7050-T7451 alloy [133] is used for the design of the upper skins, upper stiffeners and spar caps of the wingbox, and

2024-T351 alloy [134] is used for the design of the lower skins, lower stiffeners and the ribs, since it is better suited for structures stressed by cyclic tension loads and therefore prone to fatigue damage. The physical and mechanical material properties are listed in Table 4.2.

Table 4.2: Material properties of aluminium alloys

Material Properties	2024-T351	7050-T7451
Modulus of elasticity	73.1 GPa	71.7 GPa
Shear modulus	28 GPa	26.9 GPa
Shear strength	283 MPa	303 MPa
Ultimate tensile strength	469 MPa	524 MPa
Yield tensile strength	324 MPa	469 MPa
Density	2,780 kg/m^3	2,830 kg/m^3
Poisson's ratio	0.33	0.33

In addition to aluminium alloys, composite materials made up of T300 carbon fibres and N5208 epoxy resin, which is widely used in the aircraft industry, is used as a second material choice for the wingbox structure design. Table 4.3 defines the material properties of T300/N5208 [135].

Table 4.3: T300/N5208 composite material properties

Material Properties	T300/N5208
Longitudinal modulus E_{11}	181 GPa
Transverse modulus E_{22}	10.3 GPa
In-plane shear modulus G_{12}	7.17 GPa
Longitudinal tensile strength F_{1t}	1,500 MPa
Longitudinal compressive strength F_{1c}	1,500 MPa
Transverse tensile strength F_{2t}	40 MPa
Transverse compressive strength F_{2c}	246 MPa
In-plane shear strength F_6	68 MPa
Density	1,600 kg/m^3
Major Poisson's ratio ν_{12}	0.28

For the structural use of aluminium alloys using limit loads, an allowable stress criterion is calculated by dividing the ultimate stress by a safety factor of 1.5. On the other hand, allowable strain criteria are considered for composite materials. The ultimate strain value to be used is suggested by [136] to be 0.5%, and the

allowable limit value is obtained by dividing the ultimate strain by a factor of 1.5. The allowable strain value of 0.35% includes the margins due to fatigue and damage tolerance, assuming that the allowable strains are identical in terms of tension and compression. The minimum thicknesses of the sheet metal and the composite laminate for the structural design of the CRM wingbox have been specified as 2 mm and 3 mm, respectively. For metallic thin panels, 2 mm is an acceptable thickness for riveting from a manufacturing point of view, whilst a laminate thickness of 3 mm is recommended to maintain an adequate level of laminate damage tolerance.

Chapter 5

Finite Element Modelling of the CRM Wingbox Models

This chapter describes the development of the finite element model of the CRM wingbox configurations discussed in Chapter 4. The finite element type selection, mesh quality checks, boundary conditions, wing loads introduction and flutter analysis methods will be presented. The finite element model was developed to be used in the structural optimisation module for sizing and mass estimation of the primary wing structure components.

5.1 Generation of the CRM Finite Element Model

5.1.1 Selection of Finite Element Types

In general, many finite element types could be used to model and analyse aerospace structures, which are usually characterised as being thin-walled stiffened structures, and the correct choice of element type is linked very closely to the type of loading that the structure carries. Three main finite element types may be used to model thin-walled structures. These elements are shear panels and shell elements with only bending, only membrane, or both bending and membrane behaviour [137,138]. Depending on the external loading condition, revised formulations of shell elements, which include the drilling degrees of freedom, are also used. Alternatively, beam or rod elements may be used to model stiffeners and spar caps.

In the current study, the thin-walled structures of the CRM wingbox configurations (skins, webs and ribs) were modelled using two-dimensional quadrilateral and triangular shell elements (CQUAD4, CTRAI3) with in-plane membrane and bending stiffness. On the other hand, stiffeners and spar caps were modelled using one-dimensional rod elements (CROD) with axial stiffness.

5.1.2 Mesh Quality Checks

It is well known that the accuracy of finite element analysis, such as stress analysis, can be improved by the element sizes reduction or an increase in element numbers. Highly accurate solutions may be found for simple structures by reduction of the element sizes. However, for large complex structures, such as transport aircraft wings, the use of excessively fine elements in the finite element model may result in a long computational time that exceeds the memory capacity of existing computer systems. Therefore, it is important to ensure that the CRM wingbox model has a sufficient number of elements so as to obtain the desired results with an acceptable level of accuracy and computational cost. Much of today's widely used pre-/post-processing software for finite element analysis has fully automatic mesh generation methods and mesh verification criteria, which are used to check the quality of the mesh generated. In this study, the quality was checked according to the verification criteria provided by MSC.Patran [156], which include the element aspect ratio, skew angles and warp angles. Element normal, element free edge and coincident node checks were also performed. Some common element quality measures are detailed below in Table 5.1.

Table 5.1: Element quality measures

Quality Measures	Value
Aspect ratio	< 5
Skew angle	$< 30°$
Taper	$< 0.15°$
Warp angle	$< 0.05°$

5.1.3 CRM Finite Element Models

Finite element models of the CRM wingbox configurations are generated using MSC.Patran, based on the physical dimensions and material properties of the structural cross-sectional models as specified in Chapter 4. The wing planform

was modelled for a half-wing section. The structure within the leading and trailing edges was not modelled and the lower skin of the wing has no manholes. Figure 5.1 shows the finite element mesh models for the CRM wingbox structures.

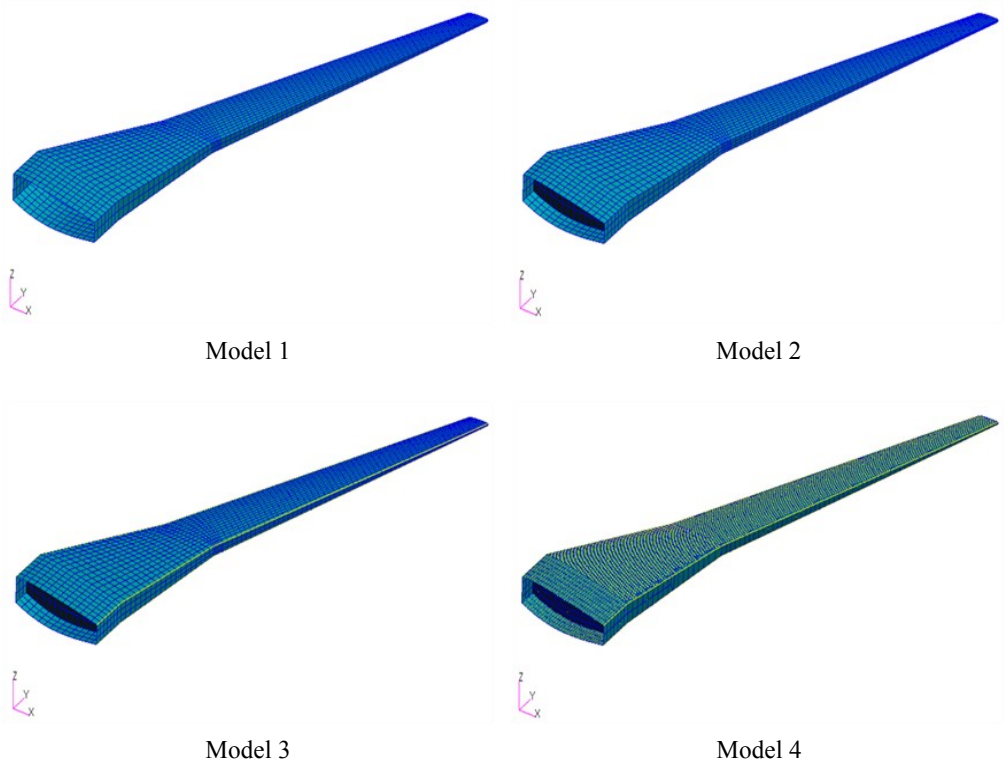

Figure 5.1: Finite element mesh models of the CRM wingbox structures

5.1.4 Modelling of Materials

Isotropic materials (aluminium alloys) and orthotropic materials (composites) were used in the modelling of the CRM wingbox structure as discussed in Chapter 4. The generation of both materials is fully supported by MSC.Patran. Inputting the material properties of the aluminium alloys into the MSC.Patran pre-processor is straightforward. Usually, the modulus of elasticity, Poisson's ratio and density are the main input values.

For modelling the wingbox using a composite material, a symmetric and balanced laminate with ply orientation angles of [45/0/-45/90]s was created in order to get an orthotropic material. The aim of this design procedure was to avoid shear extension and membrane bending coupled behaviours. The schematic of the composite laminate is given in Figure 5.2. The stacking sequence is symmetric

about the mid-plane and is balanced with the same number of +45° and -45° plies. No 0° ply was placed on the lower or upper surface of the laminate. The minimum ply thickness was taken to be 0.127 mm. The mechanical properties of the composite laminate were evaluated using the MSC.Patran Laminate Modeller.

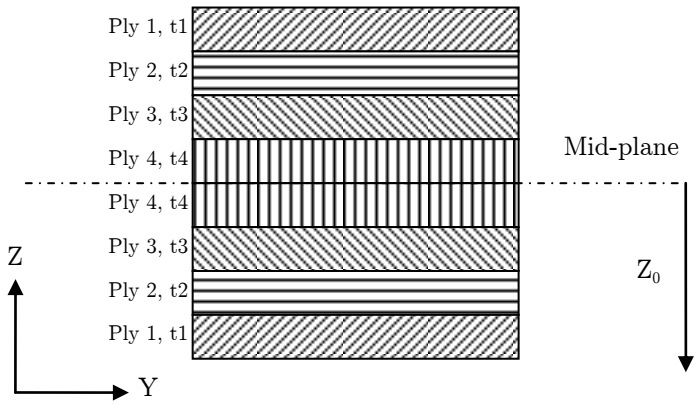

Figure 5.2: Schematic of the symmetric and balanced composite laminate

5.2 Boundary Conditions and Wing Loads Introduction Methods

According to the design methodology proposed in Chapter 3, the mass estimation of the CRM wingbox is based on multidisciplinary analysis and design optimisation sizing algorithms. Different types of analysis will be included in the sizing process, including static structural analysis, modal analysis and aeroelastic flutter analysis. The sizing algorithm will adjust the local properties of the wingbox structures according to a number of pre-defined sizing criteria. Most of the time, the sizing criteria is driven by the loads acting on the wingbox structures and therefore realistic load introduction methods become crucial for accurate wingbox mass estimation [163]. The applied loads for the set of wing loads are computed for the 2.5g pull-up critical load case. The set includes the aerodynamic loads and the inertial loads caused by the total fuel mass, engine mass, undercarriage mass, and the leading and trailing edge masses. The inertial load caused by the wingbox self-mass is dependent on the gravitational acceleration and the material properties, particularly the material density.

5.2.1 Aerodynamic Loading

Aerodynamic loading is discretely distributed along the wing by computing the equivalent lift force and pitching moment components at rib boundary locations at 25% of the local chord length. The aerodynamic loads are introduced to the wingbox structure by means of multipoint constraint (MPC) non-stiffening rigid body elements (RBE3) in the rib's perimeter nodes, as illustrated in Figure 5.3.

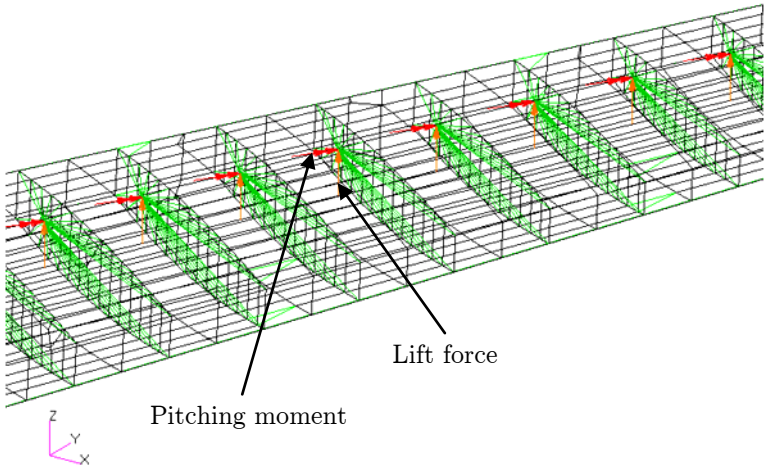

Figure 5.3: The aerodynamic load distribution reduced at the ribs

5.2.2 Fuel Loads

The total fuel mass is modelled as concentrated lumped masses using point elements distributed along the wing fuel tanks at the centre of gravity of all the rib-bay volumes, depending on the user-defined filling levels and spanwise partitioning. The fuel lumped masses are connected to the wingbox lower skin using RBE3 elements, as can be seen from Figure 5.4. The breakdown of the masses per section between two rib locations is proportional to the volume of each section.

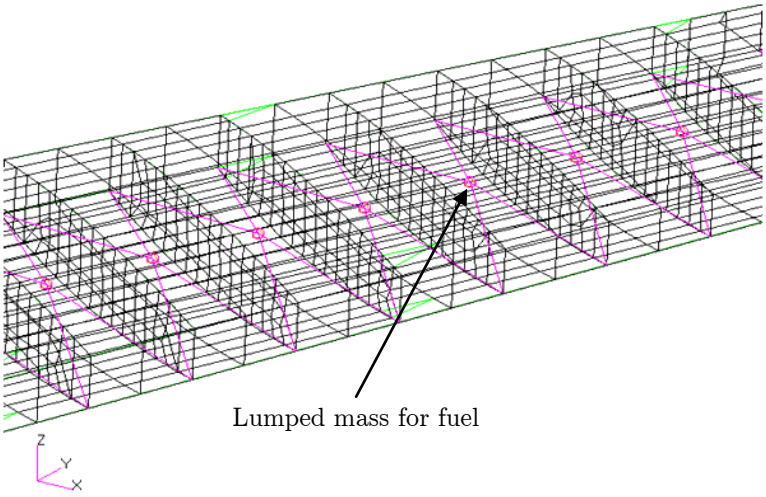

Figure 5.4: Fuel mass distribution on the wingbox lower skin

5.2.3 Engine Loads

The engine mass is modelled as a concentrated lumped mass using point elements at the centre of gravity of the engine. For the engine pylon, a simple beam structure was created to realise a distributed engine pylon-to-wingbox connection. Rod elements (CROD), mounted on front and aft fittings, modelled using a combination of non-stiffening (RBE3) and stiffening (RBE2) rigid body load-carrying elements, are used to model the engine and pylon structural components, as illustrated in Figure 5.5.

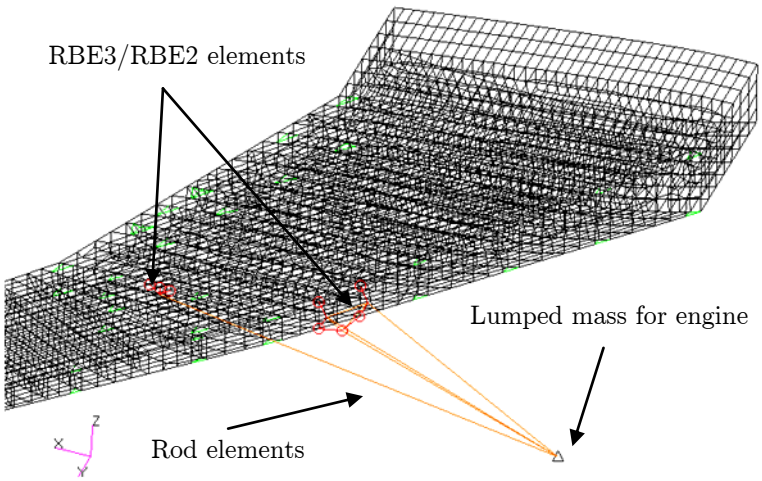

Figure 5.5: Engine mass and engine-to-pylon wingbox connections

5.2.4 Undercarriage Loads

The typical landing gear main assembly components of a transport-category aircraft are shown in Figure 5.6 [139]. Due to the high complexity level of the geometrical and structural modelling of the main landing gear, its component masses are modelled as a concentrated lumped mass using point elements, and it is introduced to the wingbox structure rear spar at its centre of gravity position using RBE3 elements, as shown in Figure 5.7.

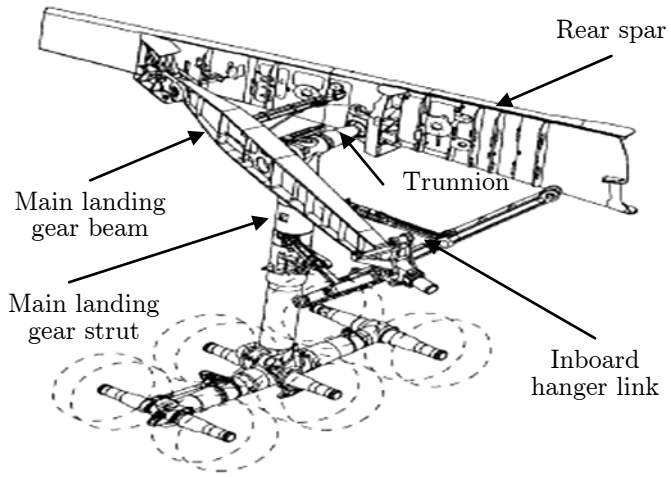

Figure 5.6: Main landing gear assembly components

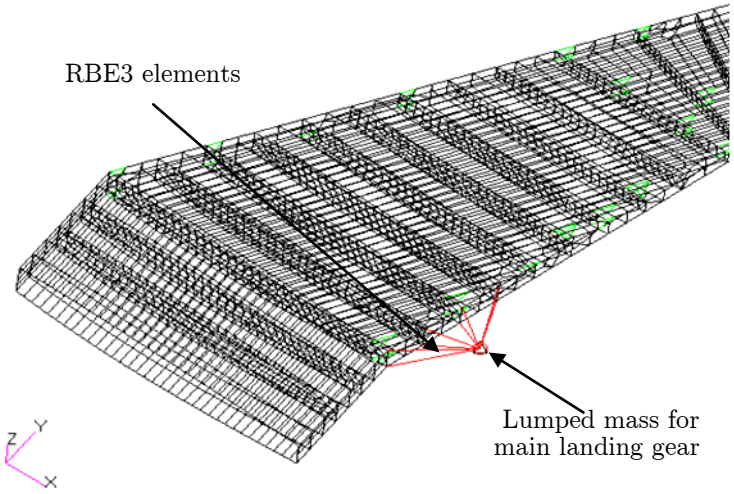

Figure 5.7: Mass distribution of the main landing gear

5.2.5 Leading and Trailing Edge Loads

The component masses of the leading and trailing edge devices are estimated based on the corresponding surface area using the semi-empirical and analytical equations of Torenbeek [21]. The inertial load impacts of these masses are modelled as lumped masses using point elements at the centre of area of the leading and trailing edge devices, and are attached to the front and rear spars of the wingbox along the span via RBE3 interpolation elements, as shown in Figure 5.8.

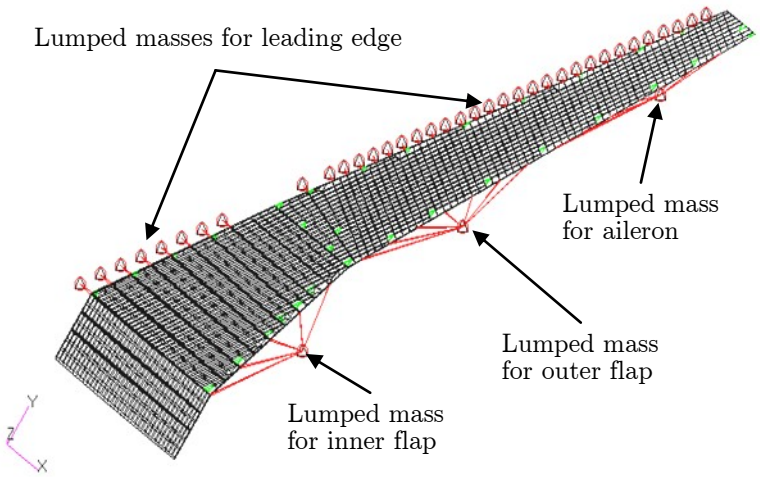

Figure 5.8: Mass distribution of the leading and trailing edge devices

5.2.6 Wingbox Self-Weight Load

The inertial load impact of the wingbox self-structural mass is derived by adding a downward gravitational acceleration ($g = 9.81\ m/s^2$) to the finite element model of the wingbox, as illustrated in Figure 5.9. The self-weight load will help to decrease the total bending moment at the wing root.

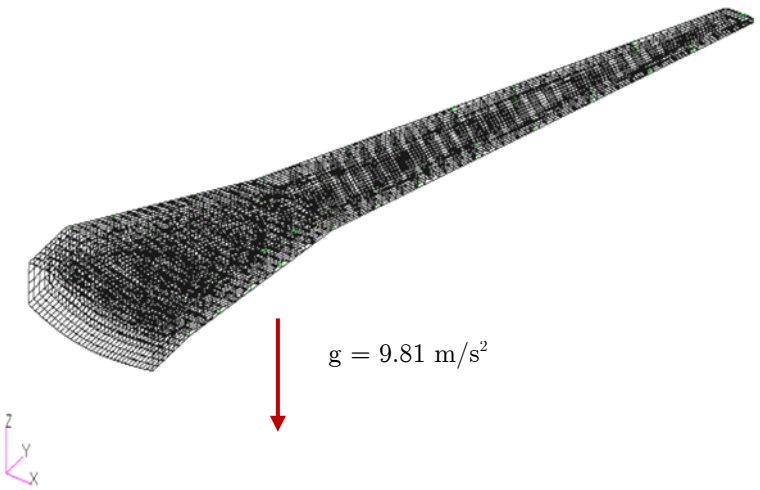

Figure 5.9: Wingbox self-weight load caused by gravitational acceleration

5.2.7 Boundary Conditions

Simulating real boundary conditions is an important and challenging part of the finite element modelling and analysis process of an aircraft structure, as it is in other engineering disciplines. In this study, spring elements (CEALS1) combined with RBE2 elements are used to create realistic boundary conditions at the wingbox root at the aircraft centreline, as shown in Figure 5.10. The spring elements were attached to a fixed ground point. The translational and rotational stiffness properties were selected to result in end boundary conditions sufficiently close to the clamped case, due to the lack of available data on wingbox root stiffness values for real aircraft structures in the open literature.

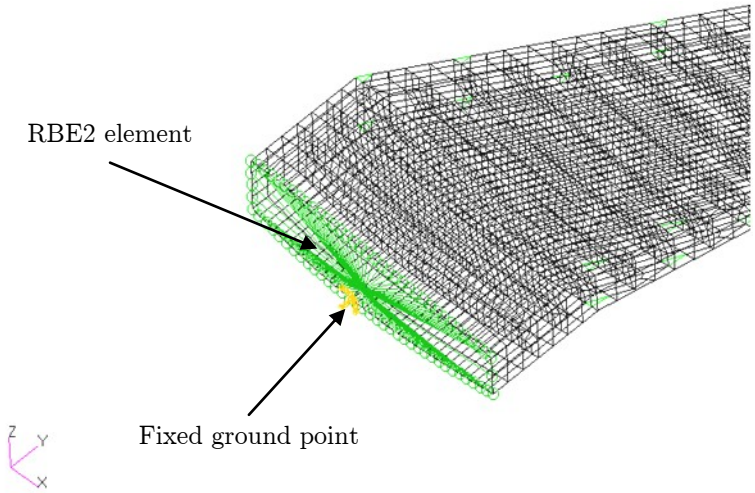

Figure 5.10: Modelling of wingbox root boundary conditions

5.3 Aeroelastic Modelling and Flutter Analysis

Aeroelasticity has been defined in many reference books [140,141,142] as the science which studies the substantial interactions among the aerodynamic, inertial and structural forces that act upon and within the flight vehicle, and the influence of these interactions on the design process. Aeroelastic phenomena are mainly described by means of a 'triangle of forces' diagram in which the inertial, elastic and aerodynamic forces each occupy a corner, as illustrated in Figure 5.11. The interaction of the aerodynamic and elastic forces results in static aeroelasticity and includes phenomena such as wing divergence, control surface effectiveness, static stability and load distribution. The interaction of the inertial and aerodynamic forces is usually associated with flight mechanics problems, while the analysis of the interaction of the inertial and elastic forces is known as structural dynamics and vibrations. The interaction of all three types of forces gives rise to dynamic aeroelastic instabilities and is shown at the centre of the diagram. It includes phenomena such as flutter, buffeting and dynamic response, of which flutter is the most important. The occurrence of flutter within the flight envelope results in a catastrophic structural failure and loss of the aircraft.

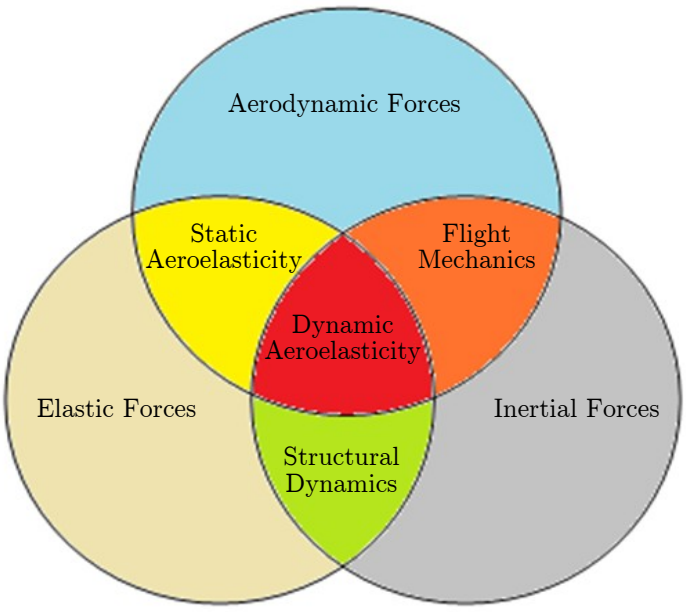

Figure 5.11: Collar's aeroelasticity triangle

The importance of aeroelasticity has been widely recognised by the aerospace industry. In recent years, the development of new types of aircraft has been explored, mainly by Boeing and Airbus. The new proposed aircraft are larger in

size, quieter, greener and more flexible than earlier generations of aircraft. By using lightweight composite materials, larger and more flexible wings have been created to generate lift with a minimum structural weight penalty. Aeroelastic effects due to wing flexibility may significantly alter the performance and safety of the new aircraft. Thus, considering aeroelastic effects at the early stages of the design is very important for producing a high-performance, competitive and safe aircraft.

5.3.1 Description of the Flutter Phenomenon

The flutter phenomenon is generally accepted as a problem of primary concern for the design of current aircraft structures. Flutter is defined as a sustained oscillation of lifting surfaces, typically aircraft wings, and vertical and horizontal stabilisers, as a result of the high-speed passage of air along the lifting panels. It is related to the self-excited vibration present at certain forward flow speeds. For aircraft, flutter should only occur at speeds that are much higher than the operating speeds of the aircraft. EASA CS 25.629 and FAR Part 25.629 specify that the aircraft must be free from flutter with an appropriate margin of damping at all speeds up to $1.15\,V_D$, where V_D is the design dive speed [125,130]. The total aerodynamic plus structural damping coefficient shall not be less than 3% ($g = 0.03$) for any critical flutter mode at all altitudes and flight speeds from the minimum cruising speed up to the speed limit as defined by the flight envelope. Minimum damping and airspeed requirements are shown in Figure 5.12. For a given flight speed, damping is the modal parameter responsible for increasing the vibration amplitude and has been used as the index of flutter stability margins. If a mode exhibits damping characteristics similar to curve (1) in Figure 5.12, where the curve crosses the $g = 0$ line above $1.15\,V_D$, the curve is considered critical for flutter. Modes as illustrated by curves (2) and (3) are considered noncritical for flutter.

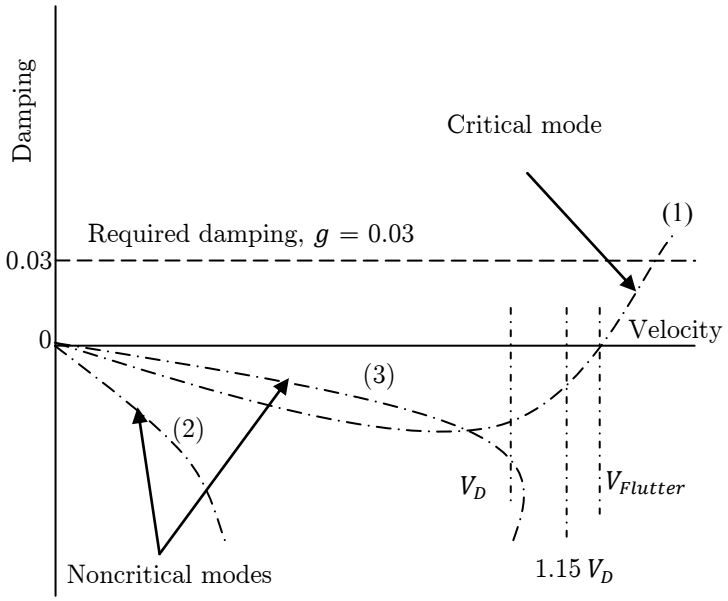

Figure 5.12: Minimum damping and airspeed requirements

Stiffness criteria based on flutter requirements are, in many instances, the critical design criteria for aircraft wing structures, and are highly influenced by structural stiffness and mass distribution. Torsional stiffness is the most significant parameter affected by flutter considerations, and it is common for the flutter condition to play a major role in the selection of wing skin thicknesses [142]. Flutter may be induced by an inappropriate ratio of the wing torsional stiffness GJ and the bending stiffness EI, or by the addition of wing mass at points far behind the wing spar. Optimum mass distributions of wing structural components and the appropriate locations and distributions of heavy mass items along the wing, such as engine and fuel mass, are usually important parameters for flutter prevention. Hence, the wing design should be verified, using airframe aeroelastic stability analysis, with respect to the structural stiffness and mass distribution in order to guarantee that the wing is free from any kind of aeroelastic instability within the design flight envelope.

5.3.2 Theoretical Background for Flutter Analysis

A typical finite element model of an aircraft structure exhibits a large number of degrees of freedom. The equation of motion of a multi degree of freedom, discrete and damped aeroelastic system can be derived based on the dynamic equilibrium of forces. The time-domain equation of motion in matrix form is given as

$$[\boldsymbol{M}]\ddot{\boldsymbol{x}}(t) + [\boldsymbol{C}]\dot{\boldsymbol{x}}(t) + [\boldsymbol{K}]\boldsymbol{x}(t) = \boldsymbol{F}(\boldsymbol{x}, t), \tag{5.1}$$

where $[\boldsymbol{M}]$, $[\boldsymbol{C}]$ and $[\boldsymbol{K}]$ represent the mass, damping and stiffness matrices of the system, respectively, and $\boldsymbol{x}(t)$ is the structural deformation vector. In general, the applied aerodynamic load vector $\boldsymbol{F}(\boldsymbol{x}, t)$ is a time function of the structural deformation and the free stream Mach number M_∞ which is defined as

$$M_\infty = \frac{V_\infty}{a_s}, \tag{5.2}$$

where V_∞ is the free stream velocity and a_s is the speed of sound, which is a function of the flow temperature and density. The applied aerodynamic load vector $\boldsymbol{F}(\boldsymbol{x}, t)$ consists mainly of two parts, as given by

$$\boldsymbol{F}(\boldsymbol{x}, t) = \boldsymbol{F}_e(t) + \boldsymbol{F}_a\big(\boldsymbol{x}(t)\big), \tag{5.3}$$

where $\boldsymbol{F}_e(t)$ represents the externally applied non-aeroelastic forces such as gust and control surface loads, and $\boldsymbol{F}_a\big(\boldsymbol{x}(t)\big)$ represents the aeroelastic forces, which are the induced aerodynamic forces due to the deformation of the structure. The aeroelastic forces are functions of flight speed and altitude, and the calculation of them relies on theoretical prediction methods that require unsteady aerodynamic computations. Since the aeroelastic forces are also functions of the structural deformation, Eqn. (5.1) can be written as

$$[\boldsymbol{M}]\ddot{\boldsymbol{x}}(t) + [\boldsymbol{C}]\dot{\boldsymbol{x}}(t) + [\boldsymbol{K}]\boldsymbol{x}(t) - \boldsymbol{F}_a\big(\boldsymbol{x}(t)\big) = \boldsymbol{F}_e(t). \tag{5.4}$$

For aeroelastic stability analysis, the non-aeroelastic forces are ignored, resulting in the following equation:

$$[\boldsymbol{M}]\ddot{\boldsymbol{x}}(t) + [\boldsymbol{C}]\dot{\boldsymbol{x}}(t) + [\boldsymbol{K}]\boldsymbol{x}(t) - \boldsymbol{F}_a\big(\boldsymbol{x}(t)\big) = 0. \tag{5.5}$$

Equation (5.5) is a nonlinear time-domain equation that defines an aeroelastic structural system that can be self-excited in nature and gives rise to aeroelastic stability problems such as flutter and divergence.

The aeroelastic stability equation can be solved using Laplace domain solution methods or frequency domain solution methods. The p method and the root locus method are the two main methods used in the Laplace domain. In the frequency

domain, two methods are generally used to perform aeroelastic stability analysis (flutter). These methods are known as the *p-k* method, or the British method, and the *k* method, or the American method. Information on the mathematical formulation and implementation of these methods can be easily found in a number of reference books on the field of aeroelasticity and its technical literature [140,141,142].

The frequency domain *p-k* method, which is widely used in the aircraft industry, is utilised to perform flutter analysis. One of the advantages of using the *p-k* method over other methods is that it produces results directly for the given velocity values, and the damping found from the *p-k* method equation represents a more realistic estimate of physical damping when compared to other methods. It also allows the use of flutter results as the design responses for aeroelastic optimisation. The fundamental matrix equation of the modal flutter solution is formulated as

$$\left[\boldsymbol{M}_{hh}\, p^2 + \left(\boldsymbol{B}_{hh} - \frac{1}{4}\frac{\rho c V_\infty \boldsymbol{Q}_{hh}^{Im}}{k}\right) p + \left(\boldsymbol{K}_{hh} - \frac{1}{2}\,\rho V_\infty \boldsymbol{Q}_{hh}^{Re}\right)\right] \boldsymbol{u}_h = 0, \qquad (5.6)$$

where $\boldsymbol{M}_{hh}$, $\boldsymbol{B}_{hh}$ and $\boldsymbol{K}_{hh}$ are the modal mass, damping and stiffness matrices, respectively, and $\boldsymbol{u}_h$ is the modal amplitude vector. The unsteady aerodynamic loads are induced into the damping and stiffness matrices. The aerodynamic matrices are dependent on the reduced frequency k but at a slow rate only. All the matrices in Eqn. (5.6) are real; $\boldsymbol{Q}_{hh}^{Re}$ and $\boldsymbol{Q}_{hh}^{Im}$ are the real and imaginary parts of the complex aerodynamic matrix $\boldsymbol{Q}_{hh}$, respectively. $\boldsymbol{Q}_{hh}$ is dependent on the Mach number and reduced frequency $\boldsymbol{Q}_{hh}(M_\infty, k)$. In Eqn. (5.6), k is the reduced frequency parameter and is defined in terms of the system angular frequency ω, the reference chord length c, and the selected free stream velocity V_∞ as

$$k = \frac{\omega c}{2V_\infty}. \qquad (5.7)$$

The eigenvalue p parameter is defined in terms of the angular frequency ω and the coefficient of the transient decay rate γ as

$$p = \omega(\gamma \mp i), \text{ where } i = \sqrt{-1}\,. \qquad (5.8)$$

The transient decay rate is related to the structural damping coefficient g by the following relation:

$$\gamma = \frac{g}{2}. \tag{5.9}$$

Equation (5.6) is solved at a set of user-specified free stream velocities V_∞ and air densities ρ, for the complex roots of the eigenvalue p parameter with the modes of interest.

For the solution of the *p-k* method, the baseline equation, Eqn. (5.6), of the system can be represented in the state-space form as

$$([\boldsymbol{A}] - [\boldsymbol{I}]p)\,\boldsymbol{u}_h = 0, \tag{5.10}$$

where $[\boldsymbol{A}]$ is the real matrix, $[\boldsymbol{I}]$ is the identity matrix and the vector $\boldsymbol{u}_h$ includes both the modal amplitudes and the velocities:

$$[\boldsymbol{A}] = \begin{bmatrix} 0 & \boldsymbol{I} \\ -\boldsymbol{M}_{hh}^{-1}\left(\boldsymbol{K}_{hh} - \frac{1}{2}\rho {V_\infty}^2 \boldsymbol{Q}_{hh}^{Re}\right) & -\boldsymbol{M}_{hh}^{-1}\left(\boldsymbol{B}_{hh} - \frac{1}{4}\frac{\rho c V_\infty \boldsymbol{Q}_{hh}^{Im}}{k}\right) \end{bmatrix}. \tag{5.11}$$

Equation (5.6) is solved at several given values of velocities V_∞ and air densities ρ, for the complex roots of the eigenvalue parameter p associated with the modes of interest. This is achieved by an iterative solution that matches the reduced frequency k to the imaginary part of the eigenvalue parameter p for every structural mode. Plots of V_∞ versus g can then be used to determine the flutter speed. Flutter occurs for values of M_∞, k, and ρ for which $g = 0$, where g goes from negative to positive values, indicating instability.

5.3.3 Flutter Analysis Method

In this thesis, the MSC.FlightLoads and Dynamics module is used to perform dynamic stability analysis (flutter) using MSC.Nastran solution Sol 145. The *p-k* method is selected for flutter analysis. The purpose of the flutter analysis is to find the target flutter instability. The flutter frequency and speed, as well as the flutter mode shape, are analysed. The first step in carrying out flutter analysis is to develop and verify the wingbox finite element structural model. This should

include the lumped masses of the unmodelled leading and trailing edge portions of the wing, the main landing gear mass and the engine mass. The fuel lumped masses contained within the wing fuel tanks are also taken into account. These lumped masses must be included in the analysis, since they significantly reduce the torsional frequency of the wingbox, which also slower the flutter speed.

The second step incorporates the computation of the natural frequencies and mode shapes of the wingbox structure. The natural frequency values of interest are the input values for the calculation of reduced frequencies k for the flutter analysis. MSC.Nastran solution Sol 103 is used to perform natural frequency and normal mode analysis. In MSC.Nastran Lanczos method is suggested to perform real eigenvalue extraction. It is the preferred method for most medium-to-large-sized finite element models.

The next step is to calculate the aerodynamic matrices $\boldsymbol{Q}_{hh}(M_\infty, k)$. This requires the calculation of the unsteady aerodynamic forces. These are calculated in the frequency domain for a discrete set of reduced frequencies based on the assumption of the undamped harmonic motion using the Doublet Lattice Method (DLM). The DLM is based on the linearised aerodynamic potential theory of subsonic flow and offers low-order models for unsteady aerodynamics in the subsonic regime, which lead to aeroelastic models suitable for flutter analysis. The DLM models the lifting surface, such as the wing of an aircraft, as an aerodynamic flat panel parallel to the flow. It does not account for the airfoil thickness, camber or pre-twist along the span of the wing. The aerodynamic panel is divided into small boxes arranged in strips parallel to the free stream velocity V_∞ with surface edges on the box boundaries. The aerodynamic mesh must comply with the specific criteria and guidelines as defined in [143,144] in order to achieve a sufficient level of accuracy, including requirements for the number of spanwise strips, the magnitude of the box aspect ratios and the numbers of chordwise boxes determined by the reduced frequency. The DLM mesh is composed of 15 x 80 boxes in chordwise and spanwise directions, as shown in Figure 5.13. The structural finite element model of the CRM wing is connected to an aerodynamic model by means of splines, as described in [143,144]. The Finite Plate Spline (FPS) fixes points on the structural model to points on the aerodynamic model so that the loads and deformations can be transferred at those points. Figures 5.14 and 5.15 show the selected spline points of the structural

model and the coupling between the aerodynamic and structural grids achieved using surface splines, respectively.

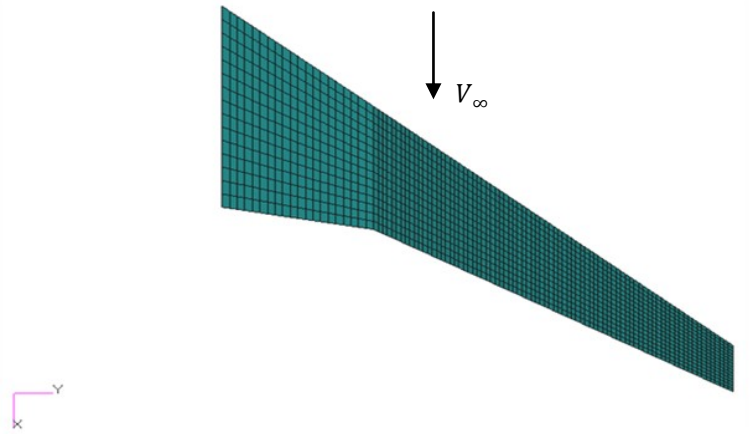

Figure 5.13: CRM wing DLM aerodynamic mesh

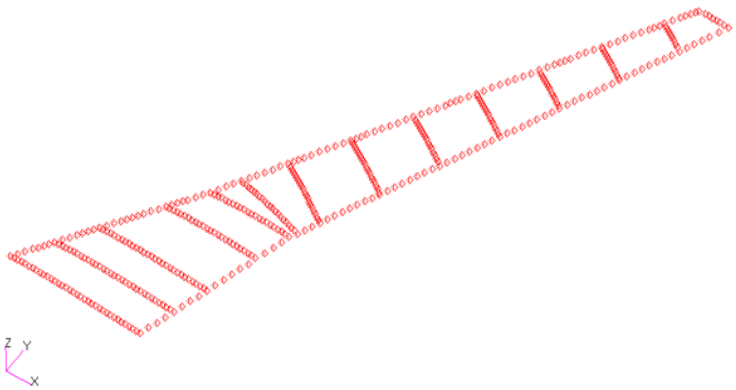

Figure 5.14: CRM wing structural model selected spline points

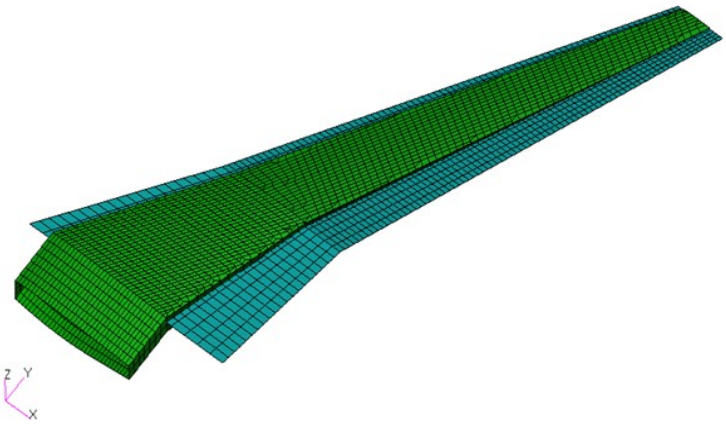

Figure 5.15: Structural and aerodynamic meshes coupling

The final step is the flutter analysis, carried out using a non-matched flutter analysis approach. This type of non-matched analysis is usually applied for the certification of subsonic aircraft. In this approach, the aerodynamic matrices $\boldsymbol{Q}_{hh}(M_\infty, k)$ are calculated for one reference value of the Mach number M_{Ref} and for a set of reduced frequencies at fixed altitude. The reference Mach number is set to M_D, which is the maximum Mach number that occurs in the aircraft flight envelope. Therefore, the analysis velocities do not match the reference Mach number and the velocity results over V_D are artificial. These results represent the flutter stability rate of reserve with respect to the flutter speed requirements.

Chapter 6

Practical Optimisation Procedure Using Gradient-Based Methods

The objective of this chapter is to propose and investigate the efficiency of a practical optimisation framework at solving large-scale nonlinear structural optimisation problems, using the existing local optimisation capability of MSC.Nastran based on gradient-based algorithms. Particular emphasis is placed on generating good initial starting points for the search process and improving the possibility of finding a better optimum solution.

6.1 Introduction

Optimisation methods play a key role in aerospace structural design; their very purpose is to find the optimal way for an engineer to obtain the utmost benefit from the available resources. As in many engineering applications, optimisation problems are mostly nonlinear with numerous mixed continuous-discrete design variables. Usually, many efforts are made to achieve sufficiently accurate results in a given amount of time.

In recent years, a variety of multidisciplinary optimisation modules have been included in a number of commercial finite element software packages that integrate different analysis disciplines for structural sizing. These include MSC.Nastran, ASTROS, GENESIS and Altair OptiStruct. In this thesis, the commercially available off-the-shelf MSC.Nastran software, which is widely used

and recognised by the aerospace industry across the globe, is preferred. The MSC.Nastran optimisation module utilises gradient-based algorithms. One of the key advantages underlying the selection of gradient-based methods is their effectiveness in solving optimisation problems where the design space is significantly large, and where the number of design variables is therefore considerably greater than the number of objectives and constraints. Another advantage is their relative computational efficiency due to rapid convergence rates with clear convergence criteria. However, one of the main drawbacks of gradient-based methods is the presence of multiple local optima, resulting in solutions where global optimality cannot be easily guaranteed. In gradient-based methods, global optimality is sought by randomly searching the design space from different starting points. However, for large nonlinear optimisation problems that involve a combination of continuous and discrete design variables, this becomes a slow and computationally inefficient method, especially when a single run of the optimiser may not converge to an optimum feasible solution. In practice, one normally seeks procedures through which the design search space is explored in a cost-effective manner, aiming for a better optimal solution within an acceptable level of accuracy depending on the size and nature of the optimisation problem.

6.2 Formulation of the Structural Optimisation Problem

Structural optimisation problems are characterised by the nature of the objective and constraint functions, which are generally nonlinear functions of the design variables. Usually, these functions are non-convex, discontinuous and implicit, as in many problems in engineering design. Furthermore, due to manufacturing constraints, design variables are quite often restricted to taking discrete values from a set of standard sizes, which gives rise to mixed integer nonlinear optimisation. Mathematically, the optimisation problem can be described as minimising or maximising the objective function $f(\boldsymbol{x})$ with respect to the design variables $\boldsymbol{x}$ under the inequality constraint $\boldsymbol{l}_i(\boldsymbol{x})$ and the equality constraint $\boldsymbol{h}_j(\boldsymbol{x})$.

The structural optimisation problem can be formalised and written as follows:

$$
\begin{aligned}
&\textit{Find } \boldsymbol{x} \textit{ to minimise } f(\boldsymbol{x}) \\
&\textit{subject to} \\
&\boldsymbol{l}_i(\boldsymbol{x}) \leq 0; i = 1,2,\dots,m \\
&\boldsymbol{h}_j(\boldsymbol{x}) = 0; j = 1,2,\dots,y \\
&\boldsymbol{x}_b^L \leq \boldsymbol{x}_b \leq \boldsymbol{x}_b^U; b = 1,2,\dots,q \\
&\boldsymbol{x}_s \in \mathrm{D}_s; \mathrm{D}_s = \{\mathrm{d}_1, \mathrm{d}_2, \dots, \mathrm{d}_\mathrm{n}\}; s = 1,2,\dots,r.
\end{aligned}
\tag{6.1}
$$

Here, $f(\boldsymbol{x})$ is the scalar objective function, $\boldsymbol{x}$ is the vector of n components, $\boldsymbol{l}$ is the vector of m inequality constraints, $\boldsymbol{h}$ is the vector of y equality constraints, $\boldsymbol{x}_b^L$ and $\boldsymbol{x}_b^U$ are the lower and upper bounds on each of the design variables (design search space), respectively, $\boldsymbol{x}_s$ is the vector of discrete design variables and D_s is the set of discrete values. The inequality and equality constraints $\boldsymbol{l}$ and $\boldsymbol{h}$ demand a solution x to be achievable only if all the constraints are satisfied. The set of all feasible solutions is named the feasible space. Typically, at least one solution x exists in the feasible space, and if this solution corresponds to the minimum objective value it is called the optimum solution.

6.3 Realisation of MSC.Nastran Design Optimisation Process

The model used for design optimisation process in MSC.Nastran can be logically divided into two parts: analysis model and design model. In the analysis model the grid is allocated across the modelled structures, elements are configured and assigned with properties, information about materials and loads are defined, boundary conditions and load cases are applied. In the design model, design variables and responses are described, objectives and constrains are applied to the model, links between element properties and variables are established. The initial design is the starting point of the optimisation process.

MSC.Nastran design optimisation process is composed of the finite element analysis, constraint screening, sensitivity analysis, approximate and improved models and the optimiser. The optimisation process is started from the finite element analysis of the initial design; afterwards the analysis is repeated multiple times during the process, with the repetition frequency defined by the design sensitivity. Constraint screening is required to select constraints that may start the redesign process. Designs constraints near violation threshold or already violated are activated during constraint screening. Design sensitivity analysis calculates the speed of change of the structural response and constraint values with changes in design variables. When a design optimisation is required, sensitivity analysis function is called automatically. The finite element analysis results are approximated and combined with the information obtained during sensitivity analysis to form the approximate model. This approximation allows minimising the number of complex finite element analyses. The approximate model is used during the optimisation process to construct the improved model. In MSC.Nastran, gradient-based, sequential linear programming and sequential quadratic programming optimisation methods are available to improve the approximate model. Soft convergence test is performed by comparison of approximate and improved models, and convergence is achieved when the changes to the model are within required range. If design is not converged, another loop of optimisation process is initiated by finite element analysis of the improved model. Hard convergence test is performed by comparison current and previous design cycle finite element analysis results. The design optimisation loop may be interrupted when either hard or soft convergence is achieved. The structural optimisation process can be significantly improved if certain approximation concepts are applied.

During the optimisation process, numerous function evaluations and response derivations are required to compute design responses and sensitivities respectively. Figure 6.1 illustrates the traditional approach to the structural optimisation, where every request of function evaluations requires finite element analysis of the model. Since the finite element analysis needs significant amount of computational power, traditional approach can only be used to solve small-scale design problems.

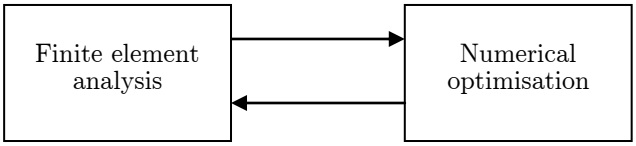

Figure 6.1: Schematic diagram of traditional approach to structural optimisation

To reduce the number of finite element analyses; approximation concepts has been developed and implemented in MSC.Nastran. These concepts that can be classified as design variable linking, constraint screening and approximate design model are described below.

Design Variable Linking

In general the design task can be narrowed if the number of design variables is minimised. To improve the efficiency of design optimisation and reduce the amount of computation, proportionally transformed design variables should be combined together, resulting in significantly reduced set of variables. Ideally, a small number of independent variables should be used during design optimisation. In MSC.Nastran design variable linking is manually performed by the user. Other concepts, such as the screening of design variables, could be considered. Pre-screening for the dimensional reduction of designs and for variable selection could play an important role in reducing the cost of the design task by identifying the most important design variables; this would allow the user to deal with large-scale design optimisation problems more effectively.

Constraint Screening

Constraint screening is another concept that can be applied to the design optimisation process to reduce the required computational power. Only constraints that are near violation threshold or already violated should be considered during optimisation, while non-critical design constraints can be deactivated. In other words, only those constrains that can trigger the redesign process should be visible to the optimiser. Constraint screening will also simplify sensitivity analysis by reducing the number of structural response derivatives required to compute design sensitivities.

Approximate Design Model

In order to establish how the active constrain set affected by design modifications, parametric analysis is preformed after the constraint screening. Response quantities, used in a parametric analysis, are approximated or expanded in series in terms of design variables. Compared to implicit finite element analysis results, formal approximations are explicitly expressed in design variables. Explicit formal approximations, computed using sensitivity analysis results, are used by the optimiser during gradient or function evaluations.

Figure 6.2 shows how the approximate design model is created and evolved during the optimisation process. The approximate model involves the construction of high-quality approximations to the finite element results, so that the number of full-scale finite element analyses can be kept to a minimum. The core of the approximate model is formed by formal approximation of the finite element analysis results. Constraint screening and design variable linking are used to simplify the approximate model. It should be noted that in MSC.Nastran, formal approximation and constraint screening are automated, while design variable linking is performed manually by the user [145].

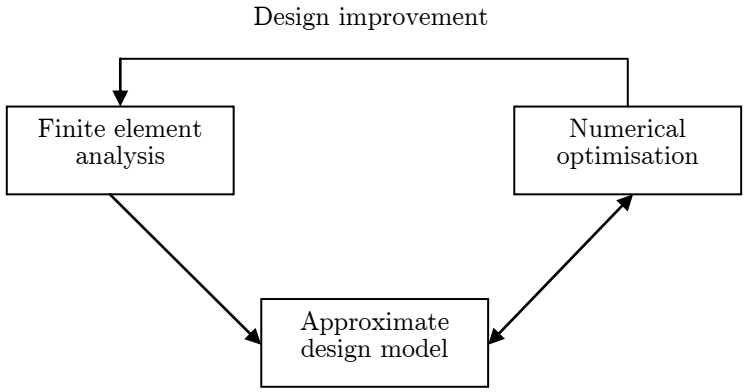

Figure 6.2: Schematic diagram of design modification process performed using approximate design model and finite element analysis

When the new configuration is generated by the optimiser, the proposed design is analysed to ensure that the design constraints are satisfied and the objective function has been improved. This process illustrated by 'Design improvement' arrow in figure 6.2.

If further design optimisation is required, the finite element analysis is performed again to form the base for the next generation approximate model. The sequence of design modifications, also referred to as design cycles, may be repeated a number of times. The design convergence is achieved when another design cycle or the optimiser are unable to produce significant changes to the model.

The detailed schematic diagram of MSC.Nastran design cycle is illustrated in Figure 6.3 [145]. Compared to traditional design approach, where the finite element model is optimised, MSC.Nastran operates with the approximate model. When the updated design configuration is generated, a finite element analysis creates new version of finite element model based on the results produced by the optimiser.

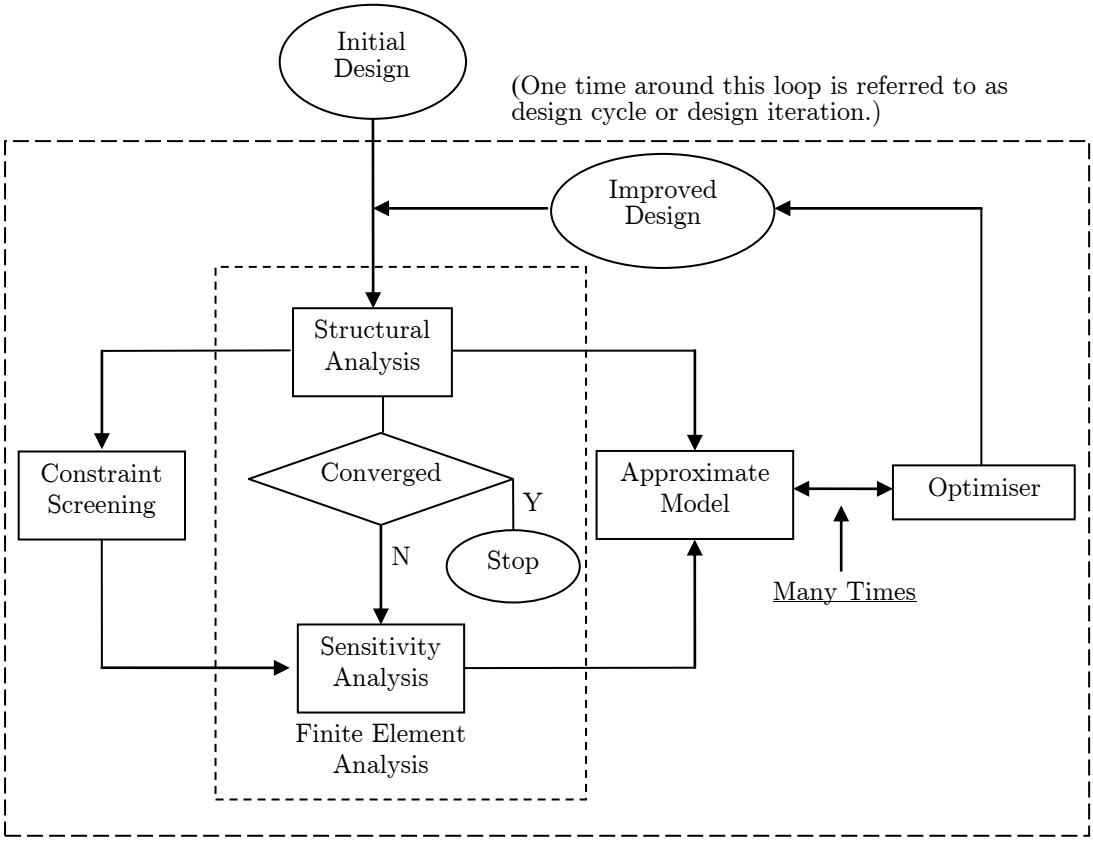

Figure 6.3: Schematic diagram of structural optimisation realised in MSC.Nastran

During the design process implementation, it is important to establish when design is complete and the process should be interrupted. Within the cycle, design is modified at two instances or levels: when optimiser generates the improved design based on the approximate model (lower level), and after finite element analysis when the finite element model is updated (higher level). As illustrated in

Figure 6.3, higher level, or hard convergence, access changes to the finite level analysis results introduced within the design cycle. Lower level, or soft convergence, is performed on the optimiser level, where design parameters and properties of the approximate model are compared before and after the optimisation. In MSC.Nastran hard convergence conditions are checked by default to stop the design process, while soft convergence can be used to terminate the design cycle in order to avoid unnecessary finite element analysis when the design alterations suggested by the optimiser are insignificant. Complete description of MSC.Nastran optimisation process can be found in [145].

6.4 Gradient-Based Optimisation Solution Procedure

Gradient-based algorithms use function gradient information to search for an optimal design. The first step in the numerical search process is to calculate the gradients of the objective function and the constraints for a given point in the design space. Once the gradient is computed, there are several options for finding a minimum. For constrained problems, sequential quadratic methods and the Modified Method of Feasible Directions (MMFD) can be used [110], whereas for unconstrained problems, quasi-Newton methods are effectively used with a line search procedure [111]. As the search direction is determined, the search process continues in that direction and can be repeated until an optimum solution has been found. The choice of optimisation method and solver is design-dependent, and generally the size of the problem and the accuracy and precession of the solvers play an important role in making the decision. In this study, the commercially available off-the-shelf MSC.Nastran software is used. The design optimisation module in MSC.Nastran is based on gradient-based solution techniques. It utilises the MMFD of Design Optimisation Tool (DOT) and MSCADS, a modified version of the Automated Design Synthesis (ADS) code for performing size optimisation.

6.4.1 Generating Good Initial Points for the Design Variables

Since gradient-based optimisation methods do not guarantee global optimality, different approaches are used to enhance the performance of the optimisation design models by generating good initial starting points for the design variables. In the first approach, two essential starting points are assigned by the user as

initial starting points. Typically, the upper and lower bounds of the continuous or discrete design variable are used. A number of interior points in the bounded design region are chosen by the user as additional initial starting points to cover more regions in the design space. These interior points can be randomly selected in the design space or, more practically, can be defined as a percentage of the upper bound value of the design variables, or by using the internal halving method.

Given a bounded design space $\boldsymbol{\Omega}_{\boldsymbol{x}}$, where the bounds on each of the design variables are in the form $\boldsymbol{x}_b^L \leq \boldsymbol{x}_b \leq \boldsymbol{x}_b^U$, a set of initial starting points $\mathrm{S} = \{\boldsymbol{x}^{(1)}, \boldsymbol{x}^{(2)}, \boldsymbol{x}^{(3)}, \boldsymbol{x}^{(4)}, \ldots, \boldsymbol{x}^{(\mathrm{n})}\}$ is generated, where $\boldsymbol{x}^{(1)} = \boldsymbol{x}_b^L$, $\boldsymbol{x}^{(\mathrm{n})} = \boldsymbol{x}_b^U$ and $\mathrm{R} = \{\boldsymbol{x}^{(2)}, \boldsymbol{x}^{(3)}, \boldsymbol{x}^{(4)}, \ldots, \boldsymbol{x}^{(\mathrm{n}-1)}\}$, R is a set of additional interior points which can be generated using one of the following methods.

As a Percentage of the upper bound value of the design variables:

$$\mathrm{R} = \left\{ \begin{array}{c} \boldsymbol{x}^{(2)} = \mathrm{a}_1 \boldsymbol{x}_b^U \\ \boldsymbol{x}^{(3)} = \mathrm{a}_2 \boldsymbol{x}_b^U \\ \boldsymbol{x}^{(4)} = \mathrm{a}_3 \boldsymbol{x}_b^U \\ \vdots \\ \boldsymbol{x}^{(\mathrm{n}-1)} = \mathrm{a}_\mathrm{n} \boldsymbol{x}_b^U \end{array} \right\}, \tag{6.2}$$

where a is a percentage value defined by the user.

Internal Halving Method:

$$\mathrm{R} = \left\{ \begin{array}{c} \boldsymbol{x}^{(2)} = \dfrac{\boldsymbol{x}_b^L + \boldsymbol{x}_b^U}{2} \\ \boldsymbol{x}^{(3)} = \dfrac{\boldsymbol{x}^{(2)} + \boldsymbol{x}_b^L}{2} \\ \boldsymbol{x}^{(4)} = \dfrac{\boldsymbol{x}^{(2)} + \boldsymbol{x}_b^U}{2} \\ \vdots \\ \boldsymbol{x}^{(\mathrm{n}-1)} = \dfrac{\boldsymbol{x}^{(\mathrm{n}-3)} + \boldsymbol{x}_b^U}{2} \end{array} \right\}. \tag{6.3}$$

In both methods, the interior points selected must be reasonably separate from each other to minimise the number of repeated visits to the same region of attraction in the search design space, and to avoid the optimiser getting stuck in local optima where no improving neighbours are available.

In the second approach, the Fully Stressed Design (FSD) algorithm, which is widely applied in the design of structures, is used to produce an initial design from a set of different starting points for the design variables provided by the user at the start of the optimisation process. Even within the limited class of problems that can be addressed, and its capability of handling a design condition subjected to strength limits only, the FSD algorithm can still provide an efficient way to begin a design task, and the output can still serve as an excellent starting point for more general optimisation tasks that need to satisfy a variety of design criteria. The FSD provides a quantitative value for the best-case estimate on the amount of material required to satisfy the applied design conditions. This technique is particularly useful if the structural weight minimisation of the designed aerospace construction is the most important requirement. The basic concept of the FSD algorithm is summarised by the following equation [145]:

$$t_i^{new} = \left(\frac{\sigma_i}{\sigma_{all}}\right)^{\alpha_{rp}} t_i^{old}, \tag{6.4}$$

where:

- t is a designed property,
- i is an index to indicate property, containing the design response and parameter,
- σ is the actual stress response quantity,
- σ_{all} is the allowable stress response quantity,
- α_{rp} is the relaxation parameter applied in the FSD to improve convergence, and it is a real number $0.0 \leq \alpha_{rp} \leq 1.0$,
- the subscripts new and old mean before and after resizing.

6.4.2 Practical Optimisation Framework

Gradient-based algorithms are very efficient at operating local searches but not so good at global searches, due to their tendency to get stuck in local optima and thus not make a thorough exploration of the design search space. A practical

optimisation framework is presented in this study to enhance the overall performance of the optimisation gradient-based algorithms. The first step is to generate a set S of initial starting points for the design variables. Then we must decide how many starting points to try and how to distribute them in the search design space. This decision is usually guided by intuition and previous experience, since there is no clear methodology available as a guide. The applicability of the FSD procedure is checked by the structural designer. If it is applicable, then a number of FSD cycles, usually 5-10 cycles, are used to generate a solution based on the FSD concept that will hopefully serve as an improved starting point for the optimisation process, because optimisation can give very poor results if poor initial guesses for the design variables are used. More general optimisation algorithms are used in the later steps of the optimisation process. The idea here is to use two different gradient-based algorithms rather than just one. The reason behind this approach is the fact that the two different algorithms will likely have completely different search directions between the initial and final points, which is output as the solution. The DOT and MSCADS optimisation codes implemented in MSC.Nastran with the MMFD are used to perform continuous and discrete optimisation. Discrete optimisation in MSC.Nastran is implemented as a post-processing step to a continuous solution or FSD; this means one additional finite element analysis followed by the discrete optimisation results. As a result, a set of solutions called A_i is created. This set contains all optimised solutions obtained using the set S of the initial starting points. Each solution is then checked to see if it meets the convergence criteria and if it is a feasible design. If this is the case, the solution with the minimum optimised mass that satisfies all the design requirements is chosen as the best of all possible candidate solutions. On the other hand, if no feasible solution exists, the user can try to test different sets of initial starting points, making sure that the optimisation problem is a well-conditioned one, that no errors have been made in specifying the model constraints and that no wrong numbers in the data are used in the optimisation. This process can be repeated until all the initial starting points defined by the user are exhausted or when the computational resources used by the algorithms, such as the computation time and memory space, exceed pre-defined limits. Figure 6.4 shows a flowchart of the proposed practical framework.

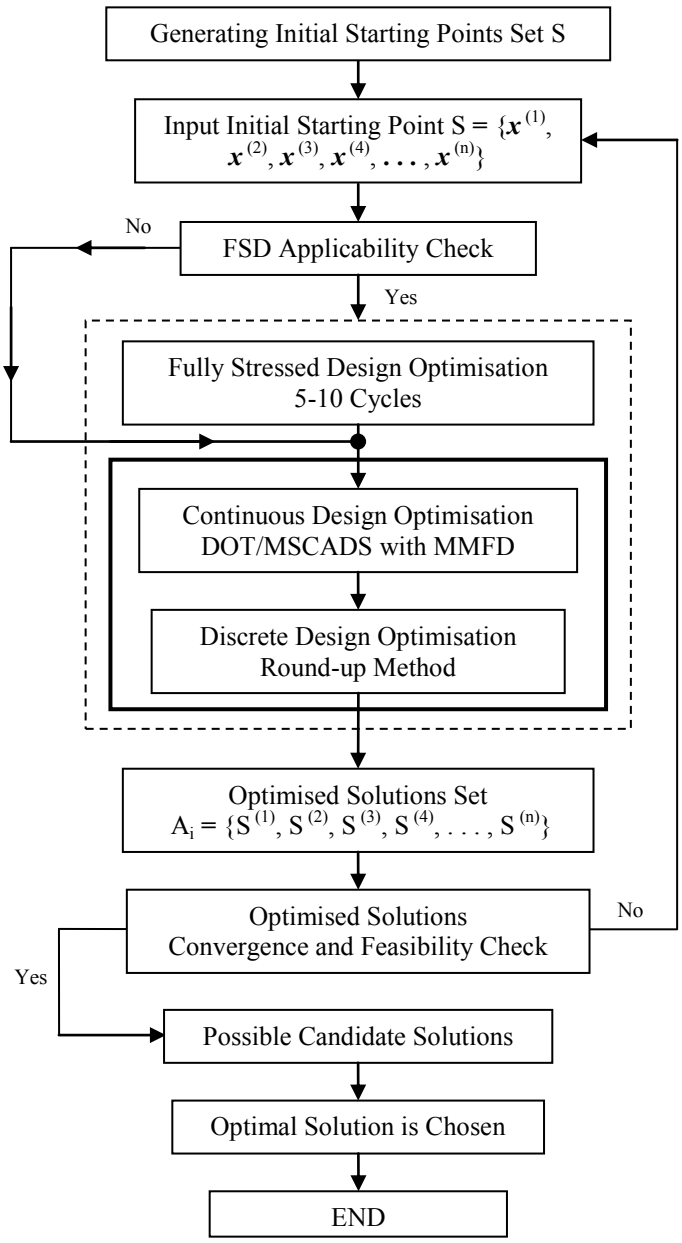

Figure 6.4: Flowchart of the proposed practical optimisation framework

6.4.3 Improving the Search for the Optimum Solution

In practice, difficulties can emerge when trying to solve a structural optimisation problem, especially when the design space is too large and contains design variables of different sensitivities, or when the optimisation problem has highly nonlinear objective and constraint functions. Problems also occur when the design variables are discrete, meaning that the search design space is discrete too. In such scenarios, it can be difficult to achieve a convergence solution, leading to a

final design that is unfeasible [146]. In this study, an improved strategy is proposed and used to enhance the search for the optimum solution. Figure 6.5 shows a flowchart of this improved strategy.

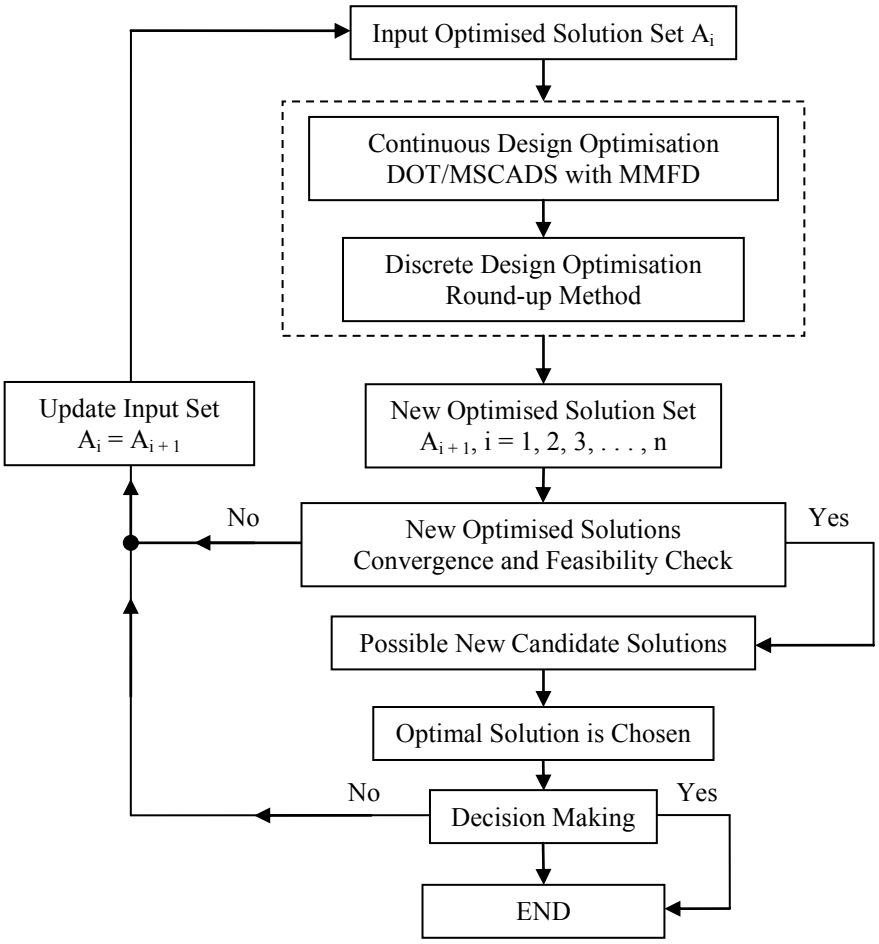

Figure 6.5: Flowchart of the improved search for an optimum solution

The strategy employed in the present work is to take the design solutions obtained using one algorithm and use them as a starting point for the other one and vice versa. A continuous and discrete optimisation solution is performed and a new set of solutions, A_{i+1}, are obtained at the end of the process. Convergence and design feasibility checks are performed, as explained in the previous section, and the solution with the minimum optimised mass that satisfies all design requirements is chosen as the best of all possible candidate solutions. In the same manner, the proposed strategy can be used to search for an improved optimum solution from the one obtained using the framework described in the previous section. This process can be repeated until an optimum feasible solution is obtained, or if an improvement in the values of the design objective is achieved.

Chapter 7

Structural Design Optimisation of the CRM Wingbox

7.1 Introduction

In this chapter, the structural optimisation of the CRM wing primary structures, both metallic and composite, is performed using the finite element method in combination with numerical gradient-based optimisation techniques. The Multidisciplinary Design Optimisation (MDO) module of MSC.Nastran is utilised in this study. The strong interaction of the structural and aeroelastic analysis disciplines along with the different design requirements and manufacturing limitations necessitate the use of MDO techniques, in order to achieve an efficient structural design with an acceptable level of accuracy for mass estimation. The optimisation problem is first described and then mathematically formulated in terms of the objective function, imposed constraints and design variables. The main goal is to study the effect of using different wingbox models of increasing structural complexity on the predicted mass of the wing primary structures. During the optimisation process, the effects of using different starting points for the design variables, the different gradient-based algorithms, and the effects of including aeroelastic constraints on the optimised wingbox configurations are also investigated.

7.2 CRM Wingbox Used for Structural Optimisation

The load-carrying structure of NASA's Common Research Model (CRM) transport aircraft wing configuration is used for the optimisation. Four different wingbox models of increasing structural complexity were created as part of this research. The technical descriptions and specifications of the NASA CRM wing as well as the wingbox models were given in Chapter 4. The structural layout of the CRM wingbox models is given in Figures 7.1, 7.2, 7.3 and 7.4. These models are discretised into components which act as design optimisation zones along the span. These areas include the upper and lower skins, front and rear spar webs, ribs, spar caps and stiffeners.

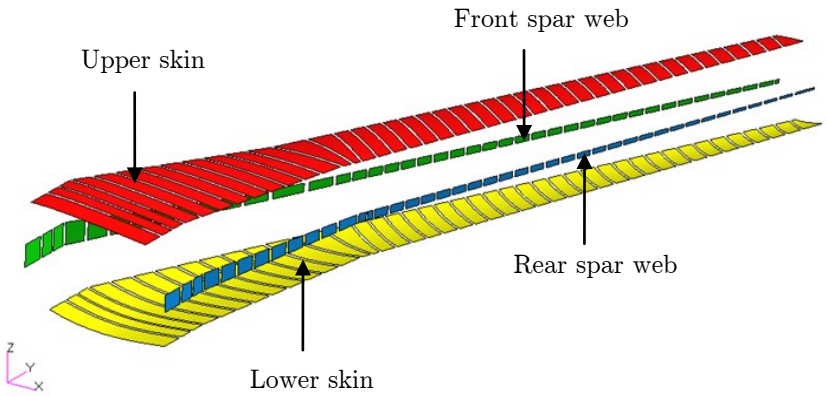

Figure 7.1: Design optimisation zones of CRM wingbox Model 1

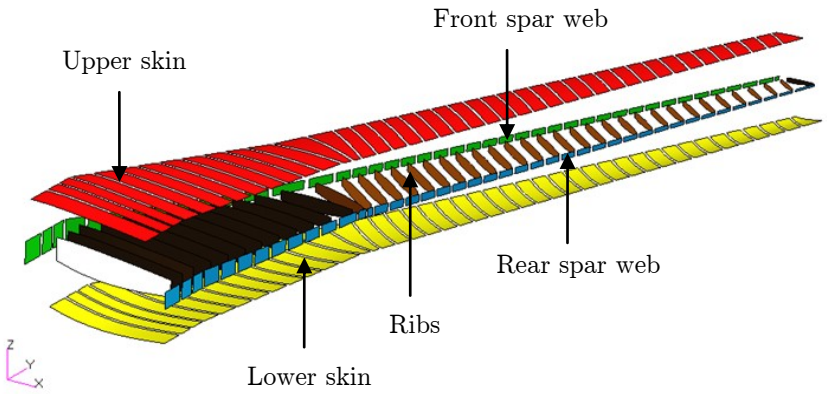

Figure 7.2: Design optimisation zones of CRM wingbox Model 2

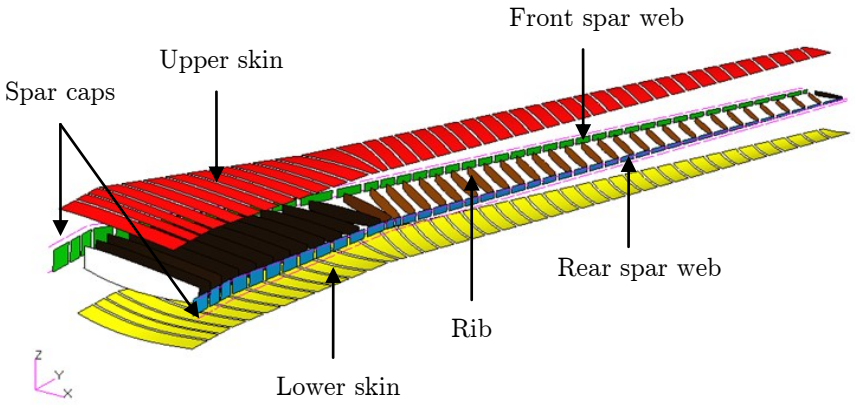

Figure 7.3: Design optimisation zones of CRM wingbox Model 3

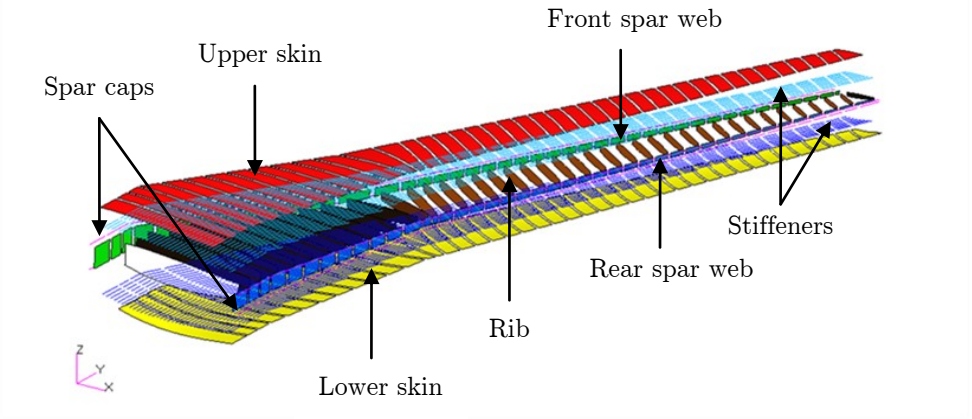

Figure 7.4: Design optimisation zones of CRM wingbox Model 4

Model 1 contains 168 design zones for the upper skin, lower skin and spar webs. Model 2 contains 210 design zones for the upper and lower skins, spar webs and ribs. Model 3 contains 378 design zones for the upper and lower skins, spar webs, ribs and spar caps. Model 4 contains 1,870 design zones for the upper and lower skins, spar webs, ribs, spar caps and stiffeners. The chordwise design zones are prescribed by the stiffener pitch, while in the spanwise direction the design zones are limited by the rib spacing. In the finite element model, each design field consists of a number of finite elements that all comprise the same thicknesses/cross-sectional areas and stiffness properties, as shown in Figure 7.5.

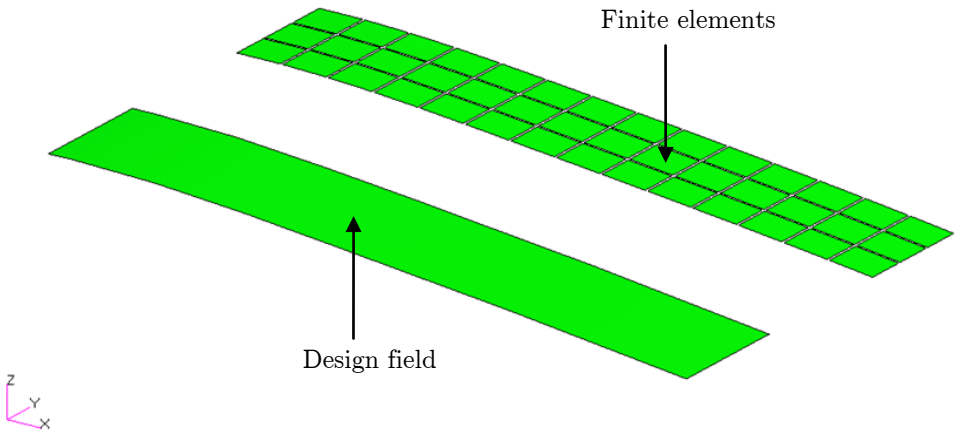

Figure 7.5: Design field consisting of a number of finite elements

7.3 Definition of the CRM Wingbox Optimisation Problem

The CRM wingbox structural optimisation that is presented in this thesis purposely deals with property optimisation. Therefore, the locations of the ribs, stiffeners and spars are considered invariable and shape optimisation is not performed in this study. The aim of the study is to minimise the masses of the metallic and composite configurations of the CRM wingbox when subjected to static strength/stiffness constraints, dynamic aeroelastic stability constraints (flutter) and side constraints (manufacturing requirements) on the design variables. The optimisation is performed using the MSC.Nastran gradient-based Sol 200 optimiser. The optimisation problem is mathematically formulated in this section as previously described in Chapter 6. The objective function, static strength/stiffness constraints, dynamic aeroelastic stability constraints and the types of design variables involved in the optimisation problem are identified.

7.3.1 Objective Function

The objective function is the structural mass of the CRM wingbox excluding any non-structural masses, like fuel mass, landing gear mass and engine mass. The objective function can be represented by:

$$\text{minimize } M(\boldsymbol{x}) = \sum_{l=1}^{N\,element} \rho_l V_l(\boldsymbol{x}). \tag{7.1}$$

Here, the objective function $M(\boldsymbol{x})$ represents the wingbox structural mass, while $N\ element$ is the number of elements in the finite element model, V_l is the volume of the lth element, ρ_l is the corresponding material density, and $\boldsymbol{x}$ is the design variable vector.

7.3.2 Design Variables

For the optimisation problem, considering the wingbox construction material to be a metallic material, one design variable per design field is defined, as described in Section 7.2. The design variables include the thicknesses of the wingbox skins, spar webs and ribs, as well as the cross-sectional areas of the wingbox spar caps and stiffeners. A minimum gauge thickness of 2 mm and a cross-sectional area of 144 mm^2 are specified for the design variables. The limits on the design variables are defined as follows:

$$2.0 \leq t_{metallic} \leq 13.5, \text{ where } t_{metallic} \text{ is the thickness in mm,} \tag{7.2}$$

$$144.0 \leq a_{metallic} \leq 972.0, \text{ where } a_{metallic} \text{ is the area in mm}^2. \tag{7.3}$$

On the other hand, considering the wingbox construction material to be a composite material, the corresponding design variables for the wingbox skins, spar webs and ribs are the thicknesses of each ply or lamina in the composite laminate associated with each design field. The cross-sectional areas of the composite spar caps and stiffeners are also treated as individual design variables for each design zone. For modelling the wingbox using a composite material, a symmetric and balanced laminate with ply orientation angles of [45/0/-45/90]s was created to get an orthotropic material. The schematic of the composite laminate is reproduced in Figure 7.6 for completeness.

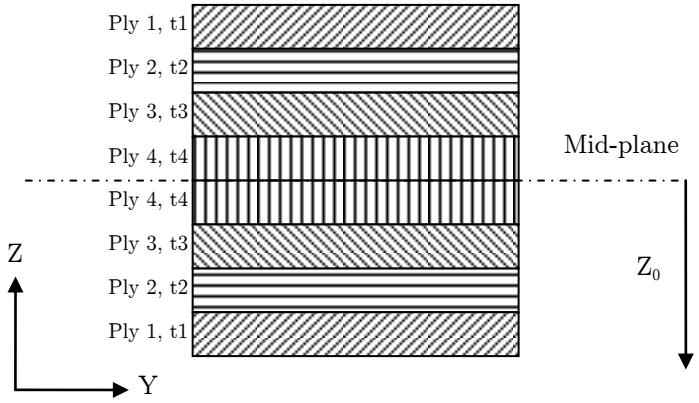

Figure 7.6: Schematic of the composite laminate

The minimum ply thickness is taken to be 0.127 mm; while a 3 mm minimum gauge laminate thickness is recommended to maintain an adequate level of laminate damage tolerance. The laminate ply thicknesses are treated as individual design variables and a count is made of the required number of plies in each ply orientation angle. The limits on the number of plies in each ply orientation angle are given as

$$3 \leq n_{ply} \leq 60, \text{ where } n_{ply} \text{ is the number of plies.} \quad (7.4)$$

Minimum cross-sectional areas of 216 mm^2 for the composite spar caps and stiffeners are specified and the limits on the design variables are defined as follows:

$$216.0 \leq a_{composite} \leq 972.0, \text{ where } a_{composite} \text{ is the area in } mm^2. \quad (7.5)$$

7.3.3 Static Strength Constraints

The failure mode of the wingbox structural components depends on their allowable stress/strain state based on the load case under consideration and the construction material. Thus, for the metallic CRM wingbox structural elements (skins, spar webs, ribs and spar caps/stiffeners), the strength constraints imposed in each design zone can be described as follows.

For metallic skin panels, spar webs and ribs, the von Mises stress is checked against the material allowable stress as defined in the following equation:

$$\sigma_{\,von\,Mises} \leq \sigma_{\,allowable}\,, \text{ where } \sigma_{\,allowable} = \frac{\sigma_{\,ultimate}}{Factor\,of\,safety\,(1.5)}\,. \qquad (7.6)$$

The von Mises stress criterion is useful since it is a single equation and is accurate for ductile materials such as aluminium alloys, which are widely used in the construction of aircraft structures. For a two-dimensional plane stress state, the von Mises stress can be defined in terms of general stress components (axial stress σ and shear stress τ) as

$$\sigma_{\,von\,Mises} = \sqrt{\sigma_{xx}^2 + \sigma_{yy}^2 - \sigma_{xx}\sigma_{yy} + 3\tau_{xy}^2}\,. \qquad (7.7)$$

The metallic spar caps and the longitudinal stiffeners are designed to carry axial stress only. Therefore, they are designed according to their stress state (tension or compression) against the allowable stress of the material.

The axial stress can be written as

$$\sigma_{axial} = \varepsilon\, E, \text{ where } \varepsilon \text{ is the axial strain and } E \text{ is the elastic modulus.} \qquad (7.8)$$

On the other hand, for composite skin panels, spar webs and ribs, the Tsai-Wu criterion [147,148,149] is used to predict the strength of the composite laminate in terms of the failure index (FI). For orthotropic plate analysis, under the plane stress state, the Tsai-Wu strength theory predicts that a lamina will undergo failure when the following inequality in satisfied:

$$FI = F_1\sigma_1 + F_2\sigma_2 + F_{11}\sigma_1^2 + 2F_{12}\sigma_1\sigma_2 + F_{22}\sigma_2^2 + F_{66}\sigma_6^2 \geq 1\,. \qquad (7.9)$$

The coefficients F_1-F_{66}, with the exception of F_{12}, are described in terms of strengths in the principal material directions. F_{12} accounts for the interaction between normal stresses, σ_1 and σ_2.

The principal strains in each ply are also checked against the material allowable strain to ensure the integrity of the plies and failure-free laminates. Thus, a constraint was placed on the strain value used for sizing the structure, as described in the following equation:

$$\varepsilon \leq \varepsilon_{\,allowable}, \text{ where } \varepsilon_{\,allowable} = \frac{\varepsilon_{\,ultimate}}{Factor\,of\,safety\,(1.5)} = 3500\,\mu\varepsilon\,. \qquad (7.10)$$

The allowable value of the strain includes the fatigue and damage tolerance margins.

The composite spar caps and longitudinal stiffeners are designed to carry axial stress only. Due to the orientation of the fibres in the longitudinal direction of the composite rods, the longitudinal strength of the composite rods is considered to be much higher than the transverse strength. Longitudinal properties are dominated by the fibres, while the transverse properties are dominated by the matrix. Therefore, the composite rods are designed according to their stress state (tension or compression) against the allowable stress of the longitudinal fibres. Generally, to obtain the properties of the composite rod, rod samples are tested for compression and tension. However, in this study, the assumed allowable stress value has been obtained by dividing the stress of the longitudinal fibres by a factor of 2. The use of a factor of safety greater than 1.5 is recommended for composite rod analysis, to account for the possible uncertainty and variability of the values of the rod properties. The axial stress constraint can be written as

$$\sigma_{axial} \leq \sigma_{allowable}, \text{ where } \sigma_{allowable} = \frac{\sigma_{ultimate}}{Factor\ of\ safety\ (2)}. \tag{7.11}$$

7.3.4 Static Stiffness Constraints

In aircraft wing design, a major requirement for stiffness arises from diverse considerations such as aeroelasticity, wing flexibility and redistribution of aerodynamic loads, and these effects may be included in the optimisation process. The torsional stiffness is necessary to counteract the twisting of the wing under aerodynamic loads and thus prevent flutter. The flexibility of the wing can cause undesirable effects on its aerodynamic performance. Lift loss due to wing deformation is one of these effects that must be taken into account in the aerodynamic load calculation. The change in wing twist distribution and bending under aerodynamic loads can have a significant effect on the wing incidence angle and consequently the aerodynamic loads acting on the wing. The redistribution of aerodynamic loads results in the redistribution of stresses/strains in the wing structures, and as a result failure can occur. Therefore, the flexural stiffness of the wingbox is controlled by limiting the vertical displacement of the wingtip leading edge, and the torsional stiffness is controlled by constraining the twist angle at the tip chord of the wing.

In general, structural stiffness information is not publicly available for commercial aircraft. However, some estimation can be made on the structural stiffness of the wingbox, providing the wing deflection is known. In this study, the wingtip deflection for the CRM wing at a 2.5g pull-up manoeuver is assumed to be 15% of the wing semi-span. This is based on the relative deformations that can be expected in the wing of a transport-category aircraft as a function of the load factor, as presented in the open scientific literature [71,150]. This value also ensures that the aircraft wingtip does not strike the ground during a taxi bump load or landing operation. The current maximum allowable deflection constraint placed on a single component of the displacement at a prescribed node is defined as follows:

$$\delta_{tip(Z)} \leq 15\% \,.\, b, \text{ where } b \text{ is the wing semi-span.} \tag{7.12}$$

The angular deformation at the wingtip chord is constrained by limiting it to a value of 6° to ensure sufficient torsional stiffness and thus an adequate aeroelastic response [151]. The twist angle constraint is defined using the vertical displacements at the wingtip chord ends. Equation (7.13) shows that the twist angle at the wingtip should not exceed 6°. $(\delta)^{+}_{max}$ and $(\delta)^{-}_{max}$ are the maximum vertical displacements in positive and negative directions of the z-coordinate, respectively. Here, C is the wing chord length at the required location:

$$\Theta_{tip} \leq 6°, \text{ where } \Theta = \arctan\left(\frac{(\delta)^{+}_{max} - (\delta)^{-}_{max}}{C}\right). \tag{7.13}$$

7.3.5 Manufacturing Constraints

Practical design rules and manufacturing constraints are considered during the design and optimisation process of the CRM wingbox. A minimum gauge thickness of 2 mm is considered for the design of the metallic wingbox thin panel structures. This is because the value of 2 mm is considered an acceptable sheet metal thickness if rivets are to be used as mechanical fasteners to join the sheet metal parts of the aircraft together. For ease of manufacturing, the wingbox thin panel thicknesses are chosen from a set of discrete values defined between the lower bound and the upper bound and incremented by 0.1 as

$t_{metallic} \in \{2.0, 2.1, \dots, 20\}$, where $t_{metallic}$ is the thickness in mm. (7.14)

Generally, the calculation of the cross-sectional areas of the spar caps and stiffeners depends on the shape and dimensions of the cross-section of a given profile. In this study, the metallic and composite spar caps and stiffeners are modelled using rod elements, and therefore for ease of manufacturing the rods are sized using a discrete set of values from which any flange shape, such as L, T and Z shapes, can be produced. The discrete sets of cross-sectional areas for the metallic and composite rod elements are defined as

$a_{metallic} \in \{144, 158, \dots, 972\}$, where $a_{metallic}$ is the area in mm^2, (7.15)

$a_{composite} \in \{216, 223, \dots, 972\}$, where $a_{composite}$ is the area in mm^2. (7.16)

For ease of manufacturing, the limits on the number of plies in each ply orientation angle are selected from a set of discrete integer values defined between the lower bound and the upper bound and incremented by 1 as

$n_{ply} \in \{3, 4, \dots, 60\}$, where n_{ply} is the number of plies. (7.17)

Practical design criteria are applied to the design and optimisation process of the composite laminate wingbox structures. The ply orientation percentages within a laminate are bounded by lower and upper bound values of 10% and 60%, respectively. This aims to avoid matrix-dominated behaviours. An optimisation constraint is applied to link the +45° and -45° layers, ensuring that their thicknesses are identical. This is done to ensure that the laminate is balanced and to minimise the possibility of introducing manufacturing stresses such as torsion. A maximum property drop-off rate criterion is applied. It aims on the one hand, at avoiding delamination and, on the other hand, at obtaining ply layouts that can actually be manufactured. The property drop-off rate between neighbouring elements/panels is evaluated according to the following equation [152]:

$$Property\ drop-off\ rate = \frac{prop_1 - prop_2}{distance(d)} \leq 20\%, \quad (7.18)$$

where $prop_{\mathrm{i}}$ is the element/panel property value of the parent (1) or adjacent (2) element/panel and the distance d is computed along the element/panel surfaces between adjacent centroids, as shown in Figure 7.7 [152].

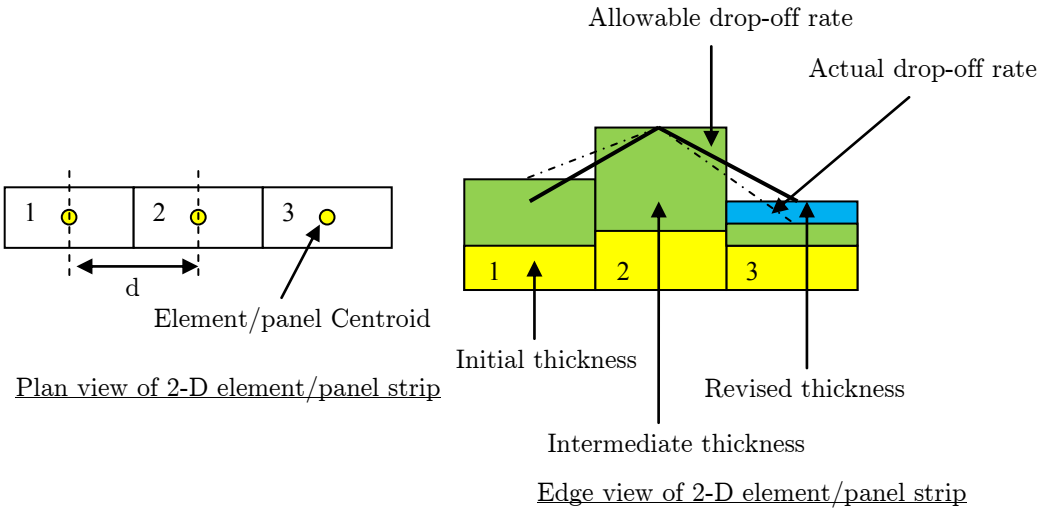

Figure 7.7: Control of property taper rate

Figure 7.7 shows how the property drop-off rate control is applied to ensure that thickness changes occur at an acceptable rate. The actual property drop-off rate from panel 2 to panel 3 indicated by the black dashed line is greater than the allowable drop-off rate, indicated by the black solid line, which is an unacceptable situation. In this case, the thickness of panel 3 is revised to meet the drop-off rate criterion as shown.

7.3.6 Aeroelastic Stability Constraints

The dynamic aeroelastic stability constraint (flutter) is imposed by constraining the damping rather than the flutter speed. Defining the constraint in such a way eliminates the need for computation of the flutter speed. Exact computation of this speed is a computationally expensive task. Treating the aeroelastic constraints in this manner was first proposed by Hajela [156] and has become a standard process in MSC.Nastran [145]. Thus, the flutter constraint is defined as follows:

$$g = \frac{\gamma_{jl} - \gamma_{jREQ}}{GFACT} \leq 0, j = 1,2,\dots,nv, l = 1,2,\dots,nroot \tag{7.19}$$

where γ_{jl} is the damping for the lth root calculated at the jth velocity and γ_{jREQ} is the user-defined required damping value at the jth velocity, typically 0.03. $GFACT$ is a scale factor that converts the damping numbers into a range of suggested values, typically in the range of 0.1-0.5, which is consistent with other constraints

in the design task. A typical *GFACT* value of 0.1 is used in this study [103,145]. The flutter constraint is to be satisfied at a series of velocities up to, and may be above, the required flutter speed.

The *p-k* method of flutter analysis produces solutions only at the velocities of interest. The evaluation of the flutter constraint is performed at a number of velocities to handle the development of 'hump' modes, since at velocities lower than the required flutter speed these modes could become critical. Hence, if the flutter analysis is performed at flight speeds that are 1.1, 1.0, 0.9, 0.75, and 0.5 times the required speed, the results should be sufficient to prevent this unwanted behaviour.

7.4 CRM Wingbox Optimisation Case Studies

7.4.1 Case Study I

The purpose of this study is to investigate and understand the effect of using different wingbox configurations of increasing structural complexity on the mass estimation of the wing primary structure. The main goal here is to identify and select an appropriate model that can predict the mass of the CRM wingbox to an acceptable level of accuracy and can serve as a baseline model for further complex structural optimisation studies as we shall see later on in section 7.4.2 and sub-sections 7.4.2.1-7.4.2.3.

In this case study, the CRM wingbox was optimised to meet static strength and stiffness requirements subject to lift force only. In this initial study, no aeroelastic or manufacturing constraints are imposed nor any other types of aerodynamic or inertial forces included, keeping the problem simple and focusing on the effects of using different structural wingbox models for the structural optimisation. Moreover, all the design variables for this problem were treated as continuous design variables. The gradient-based optimisation algorithm, DOT, was used for the design sizing of the CRM metallic and composite wingbox models. During this initial stage, it was decided to formulate this optimisation study in a simple way as possible, in order to stay focused on the main objective and ensure a thorough understanding of the decisions made, including how to solve or eliminate any unusual situations that may arise during the solution process.

In the optimisation process, the design variables change continuously within a range between a lower limit and an unbounded upper limit. Therefore, the thicknesses and cross-sectional areas of the wingbox model structural components are allowed to vary until all the design requirements are met. During the optimisation, convergence is aimed for by using different starting values for the design variables, and the effects of these starting values on the final optimisation are investigated. The sets of initial values for the design variables, the thin panel thicknesses, the number of plies in each ply orientation and the flange cross-sectional areas, for both the metallic and composite CRM wingbox optimisation models, are specified as follows:

$$t_{metallic} = \{2, 4, 6, 10, 13\}\ \text{mm}, \tag{7.20}$$

$$n_{ply} = \{3, 4, 8, 11, 15\}, \tag{7.21}$$

$$a_{metallic} = \{144, 215, 420, 643, 858\}\ \text{mm}^2, \tag{7.22}$$

$$a_{composite} = \{218, 258, 358, 585, 858\}\ \text{mm}^2. \tag{7.23}$$

Tables 7.1 and 7.2 show the optimised masses of the metallic and composite CRM wingbox models, respectively, using five different starting values for the design variables. These values were chosen at random, and in order to improve the quality of the selected starting points during this continuous optimisation case study, a fully stressed design procedure was implemented.

Table 7.1: Optimised masses of metallic CRM wingbox models (kg)
- lift force only

Design variables and initial values				
$t_1\|a_1$	$t_2\|a_2$	$t_3\|a_3$	$t_4\|a_4$	$t_5\|a_5$
Wingbox Model 1				
17,990	18,587	18,641	18,531	17,999
Wingbox Model 2				
12,167	12,271	12,166	**12,149**	12,157
Wingbox Model 3				
12,245	12,129	12,167	12,276	**12,116**
Wingbox Model 4				
12,276	**12,272**	12,325	12,445	12,401

Table 7.2: Optimised masses of composite CRM wingbox models (kg)
- lift force only

Design variables and initial values				
$n_{ply1}\|a_1$	$n_{ply2}\|a_2$	$n_{ply3}\|a_3$	$n_{ply4}\|a_4$	$n_{ply5}\|a_5$
Wingbox Model 1				
12,862	13,468	13,449	13,461	13,514
Wingbox Model 2				
8,535	9,070	9,355	**8,321**	8,587
Wingbox Model 3				
8,373	8,269	9,093	9,058	**7,891**
Wingbox Model 4				
8,917	7,940	**7,192**	8,367	7,366

Based on the results presented in Tables 7.1 and 7.2, the following conclusions can be made.

By using different initial guesses for the design variables, various local optimum designs can be obtained from the gradient-based optimisation solution. In all the solutions, hard convergence is achieved and the bold values in the tables denote the local minimum solutions obtained for each CRM wingbox model.

The optimised masses of the second, third and fourth wingbox models; turned out to be lower than those obtained by the use of the first wingbox model. Therefore, it can be seen that, in the context of using high-fidelity structural models to describe and represent the CRM wingbox design, these models attempt to improve the optimised masses of the wingbox. This representation of the CRM wingbox increases the number of structural elements describing the wingbox from one model to the next. Thus, the number of design variables increases and the design space becomes larger. The possible design alternatives within the design domain thus increase, thereby increasing the chances of arriving at a better local optimum solution and mass estimate.

The optimised masses of the composite wingbox models indicate that the results are more sensitive to their initial starting values for the design variables than the results of the metallic wingbox models. In this case, there is a greater difference in the optimised masses between the composite wingbox models than for the metallic

wingbox models. This behaviour can be explained by the different mechanical properties of the composite laminate, which are more complex than those of the metallic material. The global laminate properties are dependent on the fibre orientation angles, the number of layers and their thicknesses, and the stacking sequence. For an orthotropic material, at least two elastic constants are needed to describe the stress-strain behaviour in the material. Therefore, the stiffness of an orthotropic plate must be described by two values, one along the longitudinal direction of the fibres, commonly referred to as E_L, and one transverse to the direction of the fibres, usually denoted by E_T. Using classical lamination theory [147,148,149], the bending stiffness matrix of the symmetric laminate $[\boldsymbol{D}]$ can be written as

$$[\boldsymbol{D}] = \frac{2}{3}\sum_{k=1}^{n_{ply}} [\bar{\boldsymbol{Q}}]_K \, (Z_k^3 - Z_{k+1}^3), \tag{7.24}$$

where $[\bar{\boldsymbol{Q}}]_K$ is the transformed reduced stiffness matrix of the kth layer, $(Z_k - Z_{k+1})$ is the ply thickness and n_{ply} is the number of plies. The transformed reduced stiffness matrix can be defined in terms of the ply angle $\boldsymbol{\phi}$ and the elastic constants E_{11}, E_{22}, ν_{12} and G_{12} of the orthotropic layer. The mathematical derivation of $[\bar{\boldsymbol{Q}}]_K$ can be found in [147,148]

On the other hand, the bending stiffness k_b of beam-like metallic structures under an applied force F [154,155], as shown in Figure 7.8, can be defined as

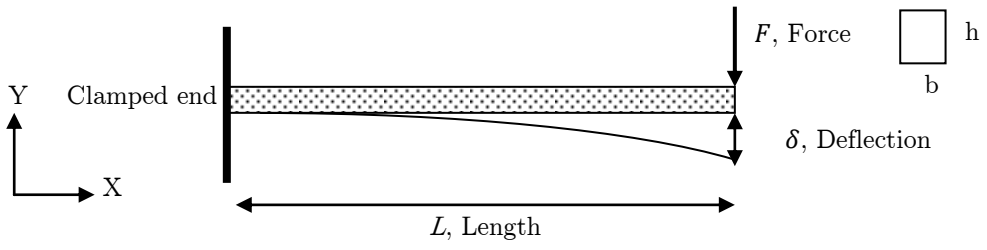

Figure 7.8: Deflection of cantilevered beam

$$k_b = \frac{F}{\delta} = \frac{3EI_{xx}}{L^3}, \text{where } I_{xx} = \frac{1}{12}\text{bh}^3, E \text{ is Young's Modulus.} \tag{7.25}$$

Mathematically, the area moment of inertia I_{xx} appears in the numerator of the stiffness equation, Eqn. (7.25), therefore the larger the area moment of the inertia, the less the structure deflects and thus the greater the stiffness.

According to Eqns. (7.24) and (7.25), the derivation of the composite laminate bending stiffness with respect to the layer thickness is a bit more complex than for the metallic isotropic material, where the stiffness is described by one constant value; the modulus E of the material regardless of the direction of load. An infinitesimal change in the composite layer thickness has an influence on its own stiffness and on the stiffness of all the layers above. We can therefore create an equivalent design with the same bending stiffness by changing the thicknesses of the composite layers while preserving the original ply orientation of each layer and the same total thickness of the laminate. The existence of multiple laminate equivalent designs has important implications for the optimisation process, in that it results in multiple optima and will always have a major influence on the objective function value.

The accuracy of the four proposed wingbox models in predicting the mass of the primary wing structure is analysed using the estimated optimum mass of the fourth wingbox model m_4 as a reference value. Table 7.3 shows the errors of the wingbox masses predicted using the four different models of increasing structural complexity.

The error has been calculated as

$$error = \frac{m_i - m_4}{m_i}, \text{where } i = 1,2,3,4. \tag{7.26}$$

Table 7.3: Errors of the wingbox mass estimation

Wingbox Model	Metallic [%]	Composite [%]
Model 1	31.78	44.08
Model 2	-1.01	13.57
Model 3	-1.29	8.86
Model 4	0.00	0.00

From Table 7.3, it is observed that the first wingbox model over predicts the primary wing structure mass for the CRM aircraft in comparison with the other models. A possible cause for this larger deviation of Model 1 can be explained by

the lack of internal chordwise oriented wing structural elements, meaning that the wing skins have to carry an additional part of the lift load that is usually transferred to the wing main spar by the ribs. Furthermore, the first wingbox model is a hollow beam and is less efficient than the rest of the models, which contain ribs with hybrid orientation, in torsional stiffness. As a consequence, the wingbox skin thicknesses are increased, resulting in an increase in the mass of the wingbox.

From the results summarised in Table 7.3, it can be seen that the second and third metallic wingbox models show good accuracy with errors of -1.01 and -1.29%, respectively, for the mass estimation of the CRM wingbox. For the composite wingbox models, this is not the case. The second and third composite wingbox models over predict the primary wing structure mass for the CRM aircraft with errors of 13.57 and 8.86%, respectively.

The total wall-clock time for each optimisation run until convergence occurs and an optimum solution has been found is also compared, and the summary of the computational time is shown in Table 7.4. In this study, computations were carried out on a laptop computer with a 2.60 GHz Intel i5 CPU and 8GB RAM.

Table 7.4: Total wall-clock time (seconds)

Wingbox Model	Metallic [s]	Composite [s]
Model 1	55.5	562.6
Model 2	55.9	497.1
Model 3	63.9	662.9
Model 4	742.4	5,303.4

From the results given in Table 7.4, it can be seen that the computational times for the optimised composite models are very long compared to the optimised metallic models, as the design space for the composite models is relatively complex with a large number of design variables and constraints. Furthermore, it is also observed that the optimisation run time was significantly increased for the fourth wingbox mass estimation model for both the metallic and composite CRM wingbox configurations. Despite the long run time, the fourth wingbox model is shown to have improved the accuracy of the objective function value, particularly for the CRM composite wingbox model, as explained in the foregoing discussion of the results presented in Table 7.3.

Based on the results presented in this case study, it can be concluded that, using the second wingbox model of structural fidelity, a preliminary estimate of the metallic CRM wingbox mass can be done with sufficient confidence, as long as the gradient-based designs are also optimised using a sufficient number of different starting values for the design variables, as practised in the design and optimisation phase of this study. Moreover, the mass of the metallic CRM wingbox can be estimated with an acceptable level of accuracy and reduced computational time. However, this is not the case for the composite CRM wingbox mass estimate, as can be seen from the results given in Tables 7.3 and 7.4. In the scenario where composite materials are used as the primary construction material for the design of the CRM wingbox, it is observed that by increasing the structural fidelity of the wingbox model, as observed in the second and third wingbox models, the discrepancy in the mass estimate becomes smaller but still significant. Therefore, it is strongly recommended that the fourth wingbox model be used as the baseline model for the preliminary estimate of the composite CRM wingbox mass, requiring higher computational time in order to achieve the required accuracy level.

7.4.2 Case Study II

The purpose of this study is to calculate the mass of the CRM aircraft wingbox when subjected to aerodynamic loads, lift force and pitching moment, and inertial relief loading due to the engine, fuel and undercarriage masses, as well as the wingbox own mass and the secondary structure masses as shown in Figure 7.9.

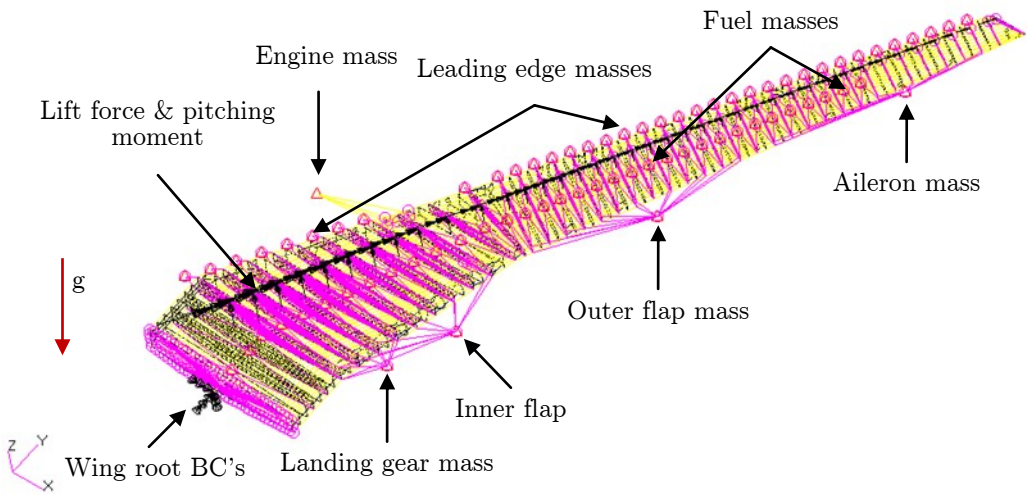

Figure 7.9: CRM wingbox Model 4 used in the optimisation study

The viability of using composites for the design of the CRM wingbox is also assessed by examining the potential benefits in terms of the total mass saving when compared to metallic materials. In order to perform such an assessment, the fourth wingbox model, which is a high-fidelity semi-monocoque finite element structural model, is used to perform sizing optimisation and to predict the mass of the CRM wingbox. The effects of aerodynamic and inertial loads on the optimised mass of the wingbox configuration are also investigated during the design optimisation. The capability of the practical optimisation procedure proposed in this thesis is also investigated.

In this case study, the CRM wingbox in its original twisted form is optimised to satisfy static strength and stiffness design requirements. Manufacturing constraints are imposed and the design variable values are selected from discrete sets. The gradient-based optimisation algorithm DOT is used for the design sizing of the CRM metallic and composite wingbox models. During this stage, 10 fully stressed design cycles are used to generate an initial solution that serves as an improved design starting point for the continuous and discrete optimisation solutions. Throughout the optimisation, convergence is aimed for by using different starting values for the design variables, and the effects of these starting values on the final optimisation are investigated. The initial values for the design variables are defined typically as the upper and lower bounds of the design variables and three additional initial starting points are defined in a more practical way as percentages of the upper bound values in order to cover more regions in the design space.

7.4.2.1 Optimisation Results of the CRM Wingbox Due to Aerodynamic and Inertial Loads

Tables 7.5 and 7.6 give the optimised masses of the CRM wingbox for both the metallic and composite configurations and for both the continuous and discrete optimisation solutions. It can be seen that, like before, the local optimum design can be achieved if design variables assigned with different initial values during the optimisation process. During the optimisation process, hard convergence is obtained along with a hard feasible discrete design solution.

The bold values in Tables 7.5 and 7.6 refer to the local minimum optimised solutions obtained for the metallic and composite wingbox models, using discrete values for the design variables.

Table 7.5: Optimised masses (kg) of the metallic CRM wingbox

Design variable initial values				
Min	25% Max	50% Max	75% Max	Max
Continuous solution				
10,482	10,541	10,539	10,683	10,260
Discrete solution				
10,600	10,638	10,642	10,787	**10,371**

Table 7.6: Optimised masses (kg) of the composite CRM wingbox

Design variable initial values				
Min	25% Max	50% Max	75% Max	Max
Continuous solution				
8,011	7,516	9,017	7,878	8,696
Discrete solution				
8,413	**7,946**	9,415	8,304	9,106

Figure 7.10 shows the history of the objective function as a function of the design cycles for the metallic CRM wingbox model.

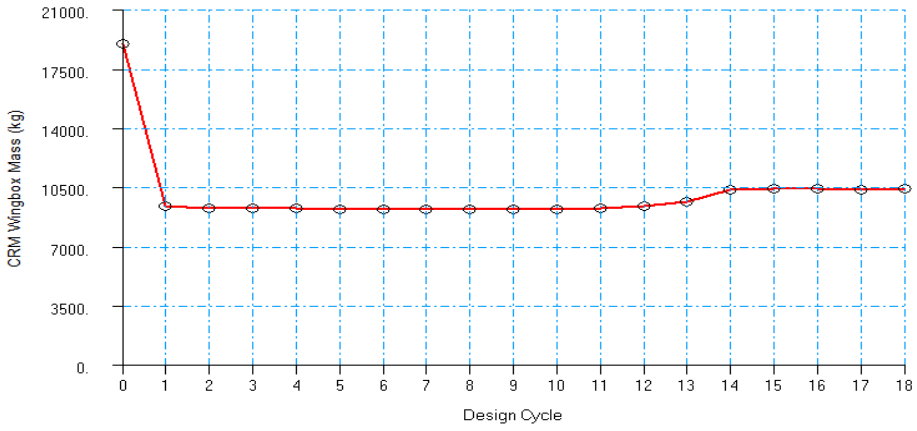

Figure 7.10: Variation of the metallic CRM wingbox mass versus the design cycle

As can be seen from Figure 7.10, hard convergence is achieved in 18 design cycles for the metallic CRM wingbox. The 0th design cycle corresponds to the initial mass of the wingbox model, which is based on the starting values of the design variables. Continuous optimisation for the metallic wingbox model is achieved in 17 design iterations. The 18th cycle, as shown in Figure 7.10, corresponds to the rounded-up discrete solution. In the round-up method, the standard size list for the design variables is used as a metric to round up continuous solutions for the design variables. Consequently, the increase of objective function value over the last design cycle in Figure 7.10 corresponds to the discrete feasible solution, found by using the round-up method.

Figure 7.11 shows the history of the maximum constraint value as a function of the design cycles for the metallic CRM wingbox model.

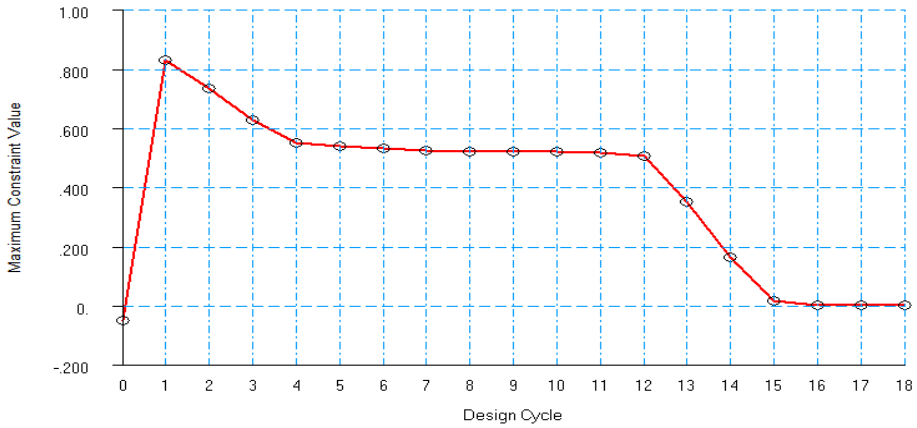

Figure 7.11: Maximum constraint value versus design cycle for the metallic CRM wingbox

From Figure 7.11, it can be seen that all constraints are initially satisfied, since the maximum constraint value of the 0th design cycle is less than the allowable value of 0.005. The 0th design cycle corresponds to the initial mass of the wingbox, which is calculated using the upper bound of the design variables. In this case, the search direction becomes the one that reduces the value of the objective function (see Figure 7.10), and therefore one or more constraints may become violated when the objective function value starts to reduce. During the search for a feasible design, movement is allowed to continue in the search direction even if the constraint violations are overcome, if a feasible design can be found that allows further reduction in the objective function value while satisfying the constraint violation criteria. For instance, although the mass of the metallic

wingbox model decreased during the first design cycle, the maximum constraint value increased and became violated, thus the search continued in the same direction until the constraint violation was overcome, the mass versus design cycle curve levelled out and a converged solution was achieved.

Figure 7.12 shows the history of the objective function as a function of the design cycles for the composite CRM wingbox model. As can be seen from this figure, hard convergence for the composite wingbox model is achieved in 18 design cycles. The 0th design cycle corresponds to the initial mass of the wingbox model, which is based on the initial values of the design variables. Continuous optimisation for the composite wingbox model is achieved in 17 design iterations. The 18th design cycle, as shown in Figure 7.12, corresponds to the rounded-up discrete solution. The increase in the objective function value in the last design cycle in Figure 7.12 therefore corresponds to the discrete feasible solution which has been found by using the round-up method.

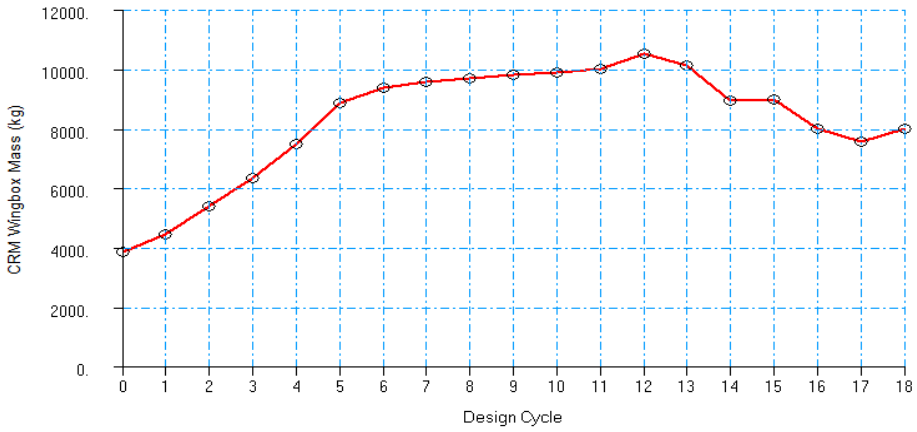

Figure 7.12: Variation of the composite CRM wingbox mass versus the design cycle

Figure 7.13 shows the history of the maximum constraint value with respect to the design cycles for the composite CRM wingbox model. As can be seen from the figure, the initial constraints are violated because the maximum constraint value is far greater than the allowable value of 0.005. The 0th design cycle corresponds to the initial mass of the wingbox which is calculated using the lower bound of the design variables. In this case, the search direction has been chosen to reduce the constraint violation. Thus, the objective function value will increase, since the first priority is to overcome the constraint violations. If it is not possible to overcome the constraint violations in this direction, they may at least be reduced.

By using a number of fully stressed design cycles at the beginning of the optimisation process, the large value of the maximum constraint violation was reduced to a smaller value during the 12th design cycle, as can be seen from Figure 7.13. After this happens, the value of the objective function starts to decrease, allowing additional reduction in the wingbox optimised mass while keeping the constraint unviolated, as can be seen from Figures 7.12 and 7.13.

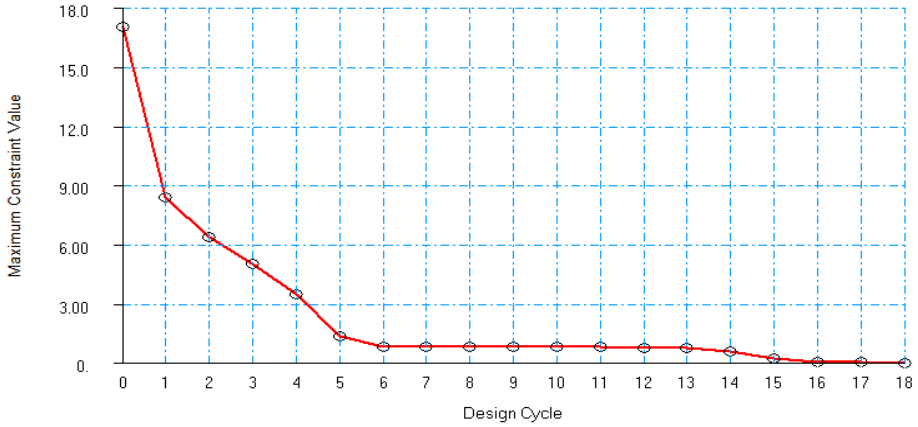

Figure 7.13: Maximum constraint value versus design cycle for the composite CRM wingbox

Figures 7.14 and 7.15 show scalar plots of the thicknesses and flange cross-sectional areas in the optimised metallic CRM wingbox model. Note, that these scalar plots refer to discrete optimisation solution results and it can be clearly seen, that there is a significant increase in the thicknesses of the wingbox thin panels as well as in the flange cross-sectional areas over the central part of the wingbox along the span. This occurs near the trailing edge kink position and close to the regions where concentrated lumped masses (engine, landing gear and fuel masses) are connected to the wingbox. These are regions of high stress levels, as can be seen from Figure 7.16 and 7.17. On the other hand, it can be observed that the thicknesses of the panels and the flange cross-sectional areas decrease towards the wingbox tip. This drop appears to reflect the lower stress levels at these regions.

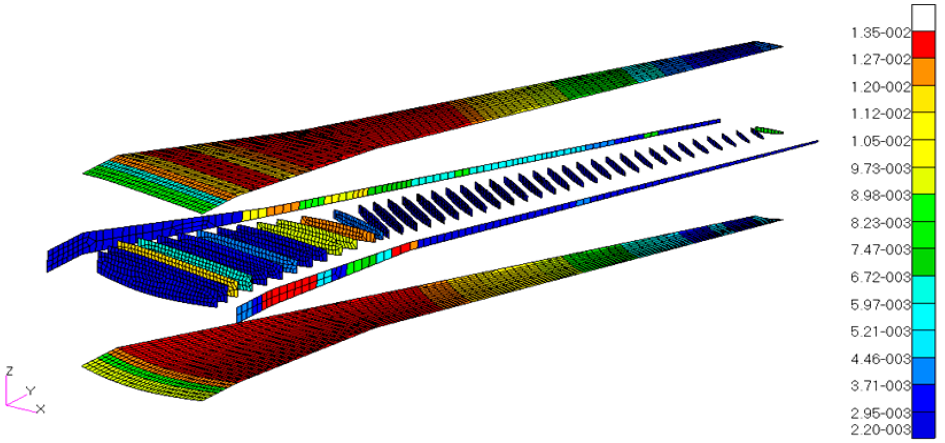

Figure 7.14: Scalar plots of the thicknesses (m) of the optimised metallic CRM wingbox model

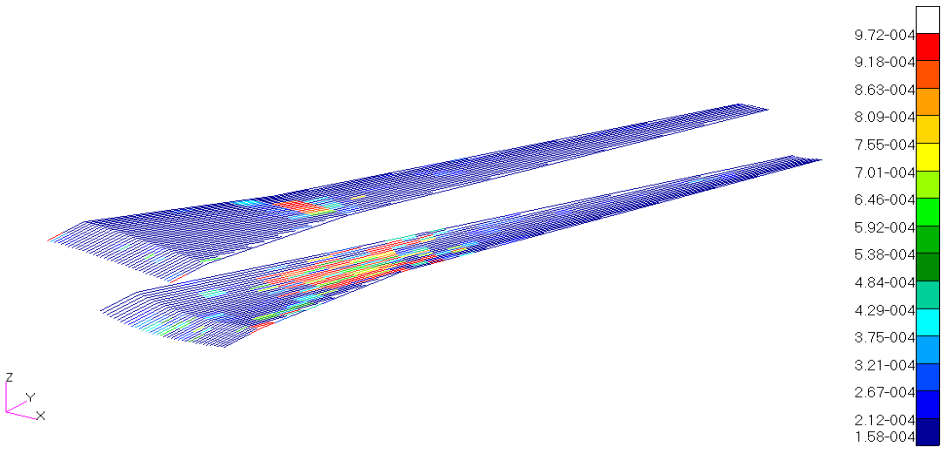

Figure 7.15: Scalar plots of the flange cross-sectional areas (m^2) of the optimised metallic CRM wingbox model

Figure 7.16 and 7.17 show fringe plots of the von Mises stress and axial stress distributions in the optimised metallic CRM wingbox model, respectively. In MSC.Patran, fringe plots are developed from the nodal averaged scalar values and plotted on the element model's faces. As the element's analysis result is moved to the element's node locations, multiple values can occur at nodes that are shared by adjacent elements. The averaging domain was specified as all entities and the drive/average method was used to determine the results. In this method, element-based tensor results are first derived, and then a simple average is applied to resolve multiple results that occur at the shared element's node locations. The element-based results are extrapolated and displayed at the nodes using shape functions. This is the preferred method, and it is the most accurate representation [156].

Figure 7.16 and 7.17 illustrate that the stress values are within the allowable stress limits defined on the design optimisation domain and they satisfy the stress constraints. Figure 7.16 shows high peak stresses close to the regions where concentrated lumped masses are connected to the rear spar. In general, and as shown in the finite element literature [157], the approximate stress field is much more accurate near the centres of the finite elements than near their nodes. Therefore, due to the local nature of these high peak stresses, they should be ignored. Figure 7.17 shows the maximum tensile and compressive axial stresses and the positions at which they occur. High-compression axial stresses are shown in the top flanges and slightly lower-tension axial stresses are shown in the bottom flanges. Under the wingbox loading conditions, these results are as expected.

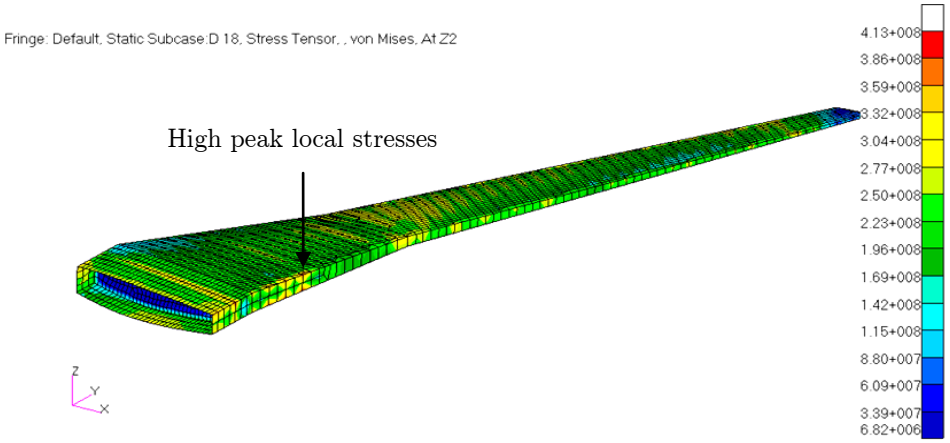

Figure 7.16: von Mises (MPa) distributions on the thin panels of the optimised metallic CRM wingbox model

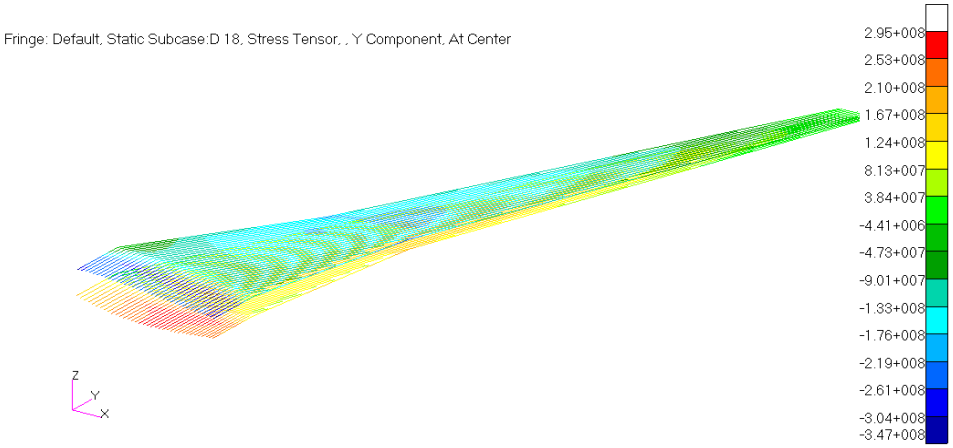

Figure 7.17: Axial stress (MPa) distributions on flanges of the optimised metallic CRM wingbox model

Figures 7.18 and 7.19 show scalar plots of the thicknesses and flange cross-sectional areas in the optimised composite CRM wingbox model. As noted before, these scalar plots refer to discrete optimisation solution results. From the scalar plots, it can be observed that thicker laminates are required to meet the structural design and optimisation requirements for the composite CRM wingbox model over the central part of the wingbox along the span as compared to the metallic model. The increase in the thicknesses and flange cross-sectional areas occurs near the trailing edge kink position and close to the regions where concentrated lumped masses (engine, landing gear and fuel masses) are connected to the wingbox. On the other hand, it can be observed that the thicknesses of the panels and the flange cross-sectional areas decrease towards the wingbox tip.

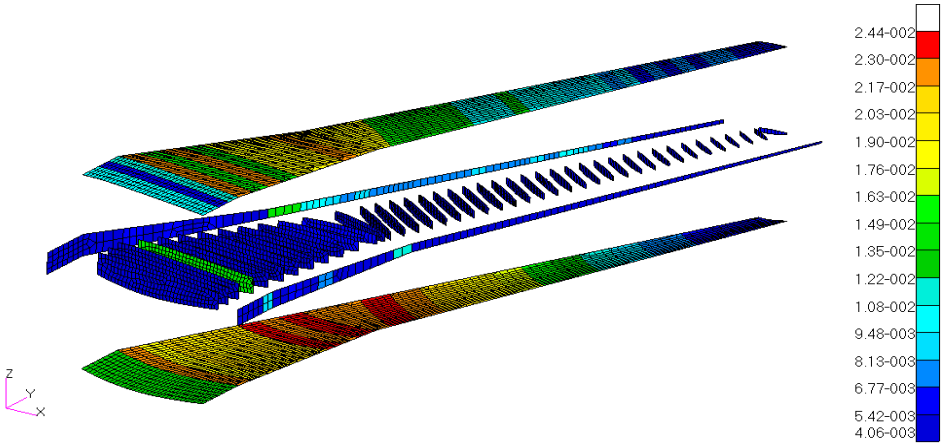

Figure 7.18: Scalar plots of the thicknesses (m) of the optimised composite CRM wingbox model

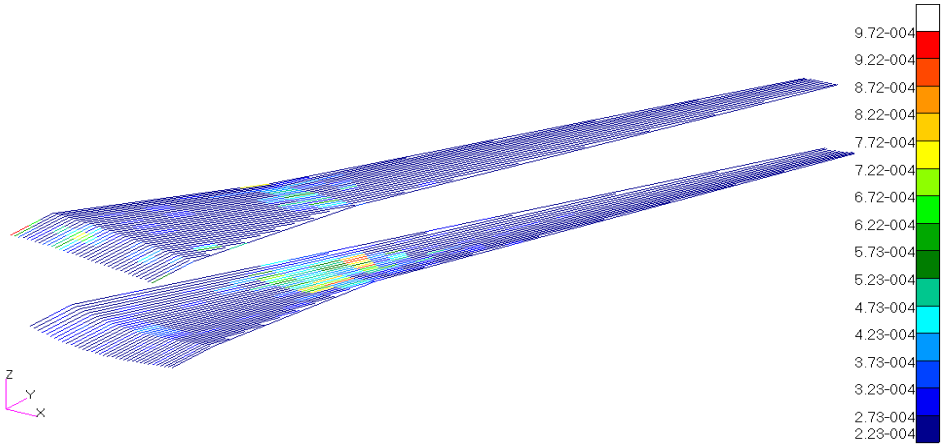

Figure 7.19: Scalar plots of the flange cross-sectional areas (m^2) of the optimised composite CRM wingbox model

For each optimised composite laminate layer, principal strain distributions, axial stress distributions and failure indices were examined. Figures 7.20, 7.21 and 7.22 show the fringe plots of the maximum and minimum principal strain distributions and the failure indices of the first layer in the optimised composite CRM wingbox model, respectively. From Figures 7.20 and 7.21 it is obvious that the maximum strain constraint is satisfied, since the values in both plots are below the upper bound limit on the strain constraint (3,500 με). Figure 7.22 shows that failure will not occur in the first layer since the failure index values are below the critical value of 1.

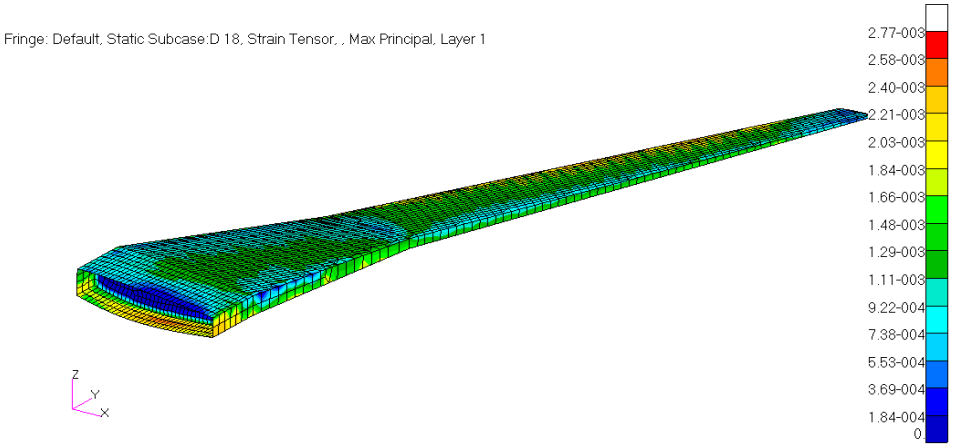

Figure 7.20: Maximum principal strain distribution (με) - layer 1

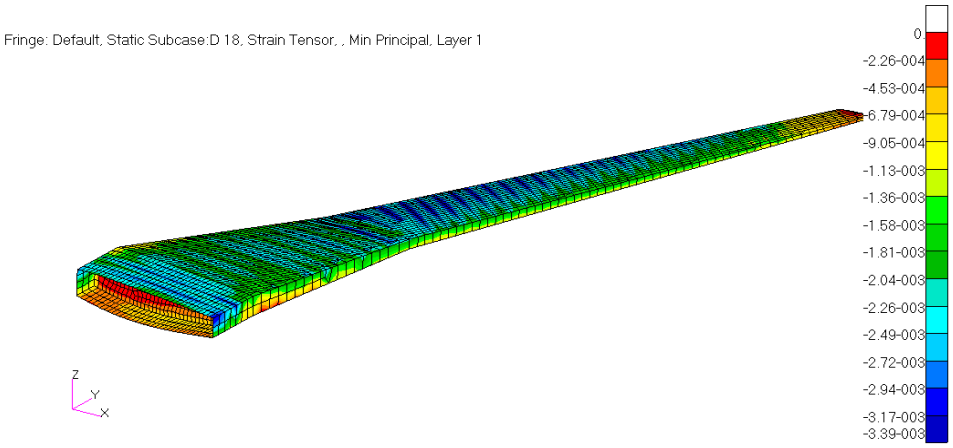

Figure 7.21: Minimum principal strain distribution (με) - layer 1

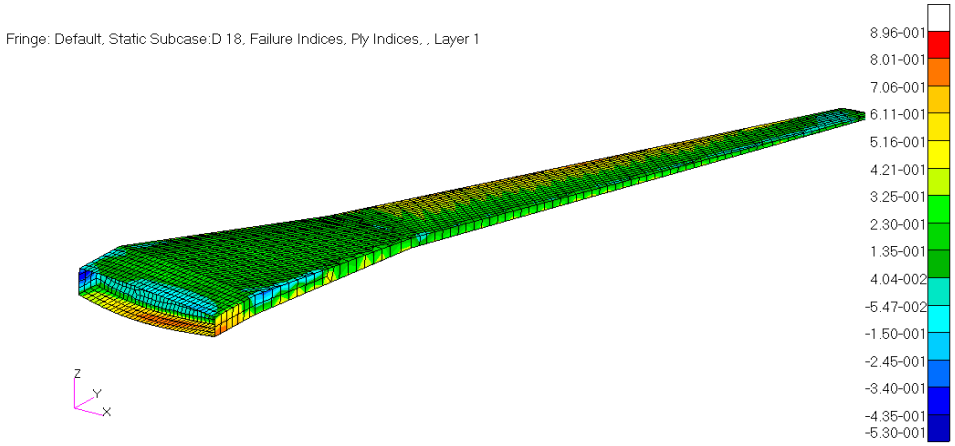

Figure 7.22: Failure indices - layer 1

Figure 7.23 shows the maximum tensile and compressive axial stresses and the positions at which they occur. High-compression axial stresses are shown in the top flanges and considerably lower-tension axial stresses are shown in the bottom flanges. Under the wingbox loading conditions, these results are as expected.

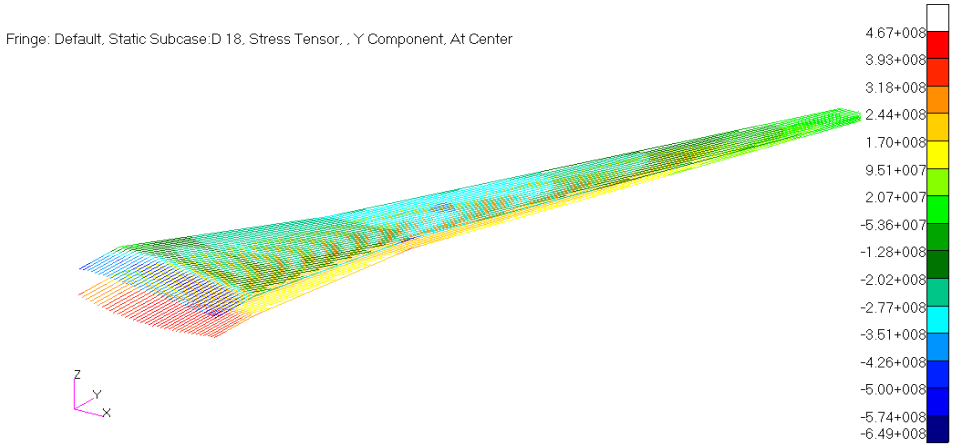

Figure 7.23: Axial stress distribution (MPa) on the flanges of the optimised composite CRM wingbox model

The deformation of the optimised metallic and composite CRM wingbox models is described by two values: the vertical tip displacement component $\delta_{tip(Z)}$, which is defined depending on the global coordinate of the wingbox model, and the angular twist at the wingtip Θ_{tip}. Table 7.7 summarises the maximum tip displacement and the change in wingtip twist from the baseline values in the optimised CRM wingbox model for both the metallic and composite configurations.

Table 7.7: Deformation values of the optimised CRM wingbox models

Deformation	Metallic	Composite
Displacement $\delta_{tip(Z)}$	4.32 m	3.03 m
Twist Θ_{tip}	3.02°	1.15°

From Table 7.7, it can be seen that using metallic materials for the design of the CRM wing generates a high wingtip deflection as compared to using composite materials. This indicates that the flexural stiffness of the metallic wing is lower than the flexural stiffness of the composite wing. Thus, the metallic wing is deflected more than the composite wing. This makes designers concerned about the effectiveness of the wing's ailerons, dynamic aeroelasticity effects such as flutter and the negative impact on aerodynamic performance that can result in lift loss.

The difference in the wingtip twist, going from the baseline model to the optimised model, shows that the wingtip twists upwards. The positive twist angle values at the wingtip indicate that the torsional stiffness of the metallic wing is lower than the torsional stiffness of the composite wing. As a result, the metallic wingtip twists more than the composite wing. The change in twist angle will effectively contribute to the angle of attack of the aircraft. Because of the effective increase in the angle of attack, aerodynamic loading on the wing also increases for the same angle of attack. The deformations of the metallic CRM wing can be reduced to a lower value, but at the cost of increasing the structural mass of the wing, which is considered a major disadvantage in the design process of a commercial transport aircraft.

Figures 7.24 and 7.25 show the deformation plots of the optimised metallic and composite CRM wingbox models. The maximum displacement is determined as 4.32 m and 3.03 m, respectively.

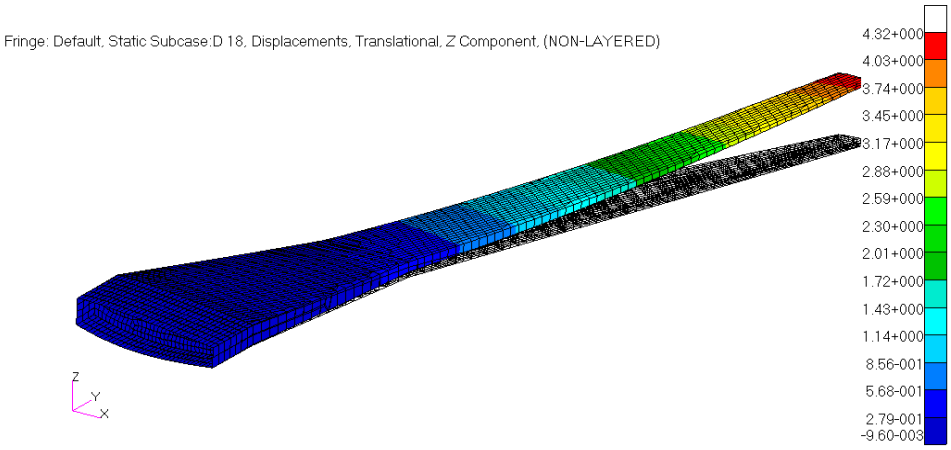

Figure 7.24: Deformation (m) plots of the optimised metallic CRM wingbox model

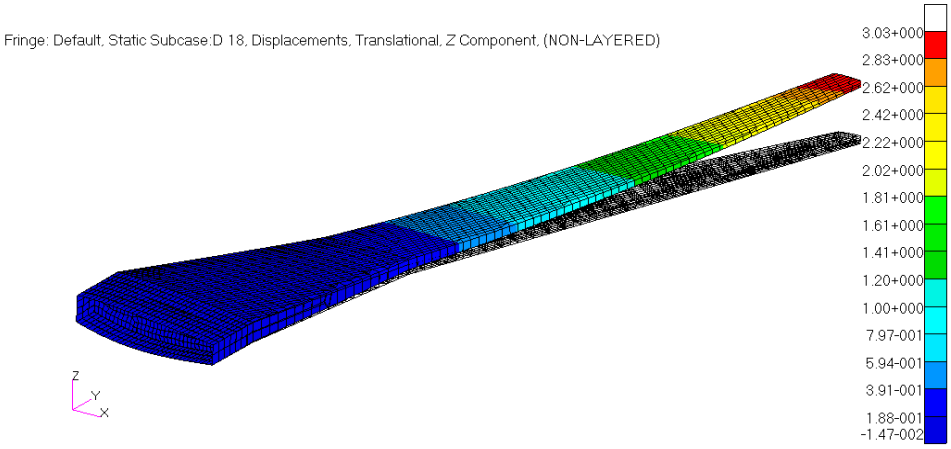

Figure 7.25: Deformation (m) plots of the optimised composite CRM wingbox model

From Figures 7.24 and 7.25, it can be seen that the maximum tip deflections (at a 2.5g load case) are less than 25% of the wing semi-span, and the corresponding curvatures are still small with the stress/strain values being within the allowable design limits. Thus, the geometric nonlinearities usually associated with high aspect ratio wings [158,159] are not an issue for the current design optimisation case study.

7.4.2.2 Mass Breakdown of the Metallic and Composite CRM Wing Models

The mass breakdown of the metallic CRM wing is given in Table 7.8. Detailed breakdowns of the wing primary and secondary structures are provided in Tables 7.9 and 7.10, respectively.

Table 7.8: Mass breakdown (kg) - metallic CRM wing

Wing structural components	Mass [kg]	Mass [%]
Primary structures	10,947.2	71.19
Secondary structures	3,853.1	25.06
Miscellaneous items	576.6	3.75
Wing mass (total)	15,376.9	100.00

Table 7.9: Mass breakdown (kg) - metallic primary structures

Primary structures	Mass [kg]	Mass [%]
Upper cover (skin + stiffener)	4,023.8	36.76
Lower cover (skin + stiffener)	4,360.6	39.83
Ribs	1,380.4	12.61
Front spar (web + spar caps)	303.5	2.77
Rear spar (web + spar caps)	302.9	2.77
Engine/pylon attachment	134.0	1.22
Undercarriage attachment	442.0	4.04
Primary structures (total)	10,947.2	100.00

Table 7.10: Mass breakdown (kg) - metallic secondary structures

Secondary structures	Mass [kg]	Mass [%]
Fixed leading edge	959.9	24.91
Fixed trailing edge	545.6	14.16
Slats	656.1	17.03
Flaps	1,320.5	34.27
Spoilers	118.3	3.07
Ailerons	155.6	4.04
Support structure	97.1	2.52
Secondary structures (total)	3,853.1	100.00

Similarly, the mass breakdown of the composite CRM wing is given in Table 7.11. Detailed breakdowns of the wing primary and secondary structures are provided in Tables 7.12 and 7.13, respectively.

Table 7.11: Mass breakdown (kg) - composite CRM wing

Wing structural components	Mass [kg]	Mass [%]
Primary structures	8,522.4	70.68
Secondary structures	3,082.5	25.57
Miscellaneous items	452.1	3.75
Wing mass (total)	12,057.0	100.00

Table 7.12: Mass breakdown (kg) - composite primary structures

Primary structures	Mass [kg]	Mass [%]
Upper cover (skin + stiffener)	2,931.0	34.39
Lower cover (skin + stiffener)	3,683.8	43.22
Ribs	949.7	11.14
Front spar (web + spar caps)	233.8	2.74
Rear spar (web + spar caps)	148.1	1.74
Engine/pylon attachment	134.0	1.57
Undercarriage attachment	442.0	5.19
Primary structures (total)	8,522.4	100.00

Table 7.13: Mass breakdown (kg) - composite secondary structures

Secondary structures	Mass [kg]	Mass [%]
Fixed leading edge	767.9	24.91
Fixed trailing edge	436.5	14.16
Slats	524.9	17.03
Flaps	1,056.4	34.27
Spoilers	94.7	3.07
Ailerons	124.5	4.04
Support structure	77.7	2.52
Secondary structures (total)	3,082.5	100.00

From the results presented in Tables 7.8 and 7.11 it can be seen that the mass of the wing primary structures is a large contributor to the overall mass of the CRM wing. The wing primary structures make up around 71.2% and 70.7% of the total

masses of the metallic and composite CRM wings, respectively. Therefore, it is important to ensure that the mass of the wing primary structures is estimated using appropriate methods and approaches that can guarantee the accuracy and quality of results.

The substructure masses of the wing primary structures summarised in Tables 7.9 and 7.12 show that the mass of the wingbox lower cover is heavier than the upper cover. This is because the lower cover was designed to withstand tension loads and fuel loads in 2.5g up-bending flight conditions. Fuel loads have a direct impact on the thickness distribution of the wingbox lower skin and thus some mass penalty is given over the upper wingbox cover.

From the results in Tables 7.9 and 7.12 it can be observed that the metallic and composite CRM wing upper cover masses make up about 36.8% and 34.4% of the total mass of the wing primary structures, respectively. On the other hand, the lower cover of the composite CRM wing makes up a slightly larger percentage of the wing primary structure mass than that of the metallic model (43.2% for the composite versus 39.8% for the metallic). It is also interesting to note that while the metallic spars share an equal percentage of the total mass of the wing primary structures; this is not the case for the composite CRM wing model. The rear spar of the composite wingbox shares a lower percentage of the total mass of the wing primary structures compared to the front spar. It is worth mentioning that during the twisting or torsion of the wing, the spars of the wing represent a wall that resists the twisting motion from the applied loads. Taking into account the previous results identified in Table 7.7 and the related discussions, the lower mass of the composite rear spar is likely to be related to the decreased torsional stiffness of the wing.

From Tables 7.10 and 7.13 it can be seen that the flaps of the CRM wing are the heaviest structural components of the wing secondary structures. The masses of the metallic wing secondary structures are calculated using the semi-empirical and analytical equations of Torenbeek [21], and the results were adjusted to account for the effects of using composite materials. Hence, the masses of the wing composite secondary structures were assumed to be 20% less than the masses of the metallic wing secondary structures.

The results from this study show that the total masses of the metallic and composite CRM wings are 30,754 kg and 24,114 kg, respectively. Thus, the total mass saving for the composite CRM wing over the metallic wing is 21.5%.

7.4.2.3 Comparison of the CRM Wing Mass Results with the Literature

Mass estimation results for the NASA Common Research Model obtained in the course of this work are first compared with the results reported in the open literature. The results are then compared to the well-known 12% rule, which estimates the wing mass as being 12% of the maximum take-off mass, and to the latest wing mass estimation equations derived by Elham in [19], which present the wing mass as a function of the aircraft maximum take-off mass and as a function of the wingbox mass computed analytically:

$$W_{wing} = 68.22 \times 10^{-4}\, MTOM^{1.25}. \tag{7.27}$$

$$W_{wing} = 9.1669 \times W_{wingbox}^{0.8248}\,. \tag{7.28}$$

Since the original purpose of the CRM was to aid in the verification and validation of computational fluid dynamics, the CRM does not provide any information with respect to the wing internal structure or the wing structural mass estimate. In recent years, a number of efforts have been made to produce a CRM wing structural model that is as representative as possible, for use as a model for aerostructural and aeroelastic design, analysis and optimisation studies [10,160,161].

Kenway et al. [161] designed a jig shape and corresponding wingbox structure that deflects to the CRM flying shape at CRM nominal flight conditions using an inverse design procedure. Later on, the CRM jig shape geometry was used to perform a high-fidelity aerostructural optimisation to determine the potential decrease in fuel burn for a long-range mission when varying wing planform and airfoil shapes. In their work, the CRM wingbox layout was produced based on the examined cutaway view of a Boeing 777 aircraft. The wingbox consists of two spars located at the leading and trailing edges, respectively. There are 49 ribs in total, including 4 ribs on the centre wingbox section, and most of them are perpendicular to the trailing edge spar. The proportions (front and rear spar locations, rib spacing, etc.) and structural layout of the Boeing 777 were the same

as used for the CRM wing. The spars located at the leading and trailing edges of the wing root were at 10% and 60% of the local chord, whereas the spars located at the leading and trailing edges of the wingtip were at 35% and 60% of the local chord. The rib spacing for the CRM wingbox was chosen to be approximately the same as for the Boeing 777, with a normal distance spacing of 73.15 cm.

In their work, Kenway et al. modelled the wingbox skin panels using a simplified model that ignored the stiffeners usually found on all modern aircrafts. Moreover, they assumed that the upper and lower wingbox skin panels had the same thicknesses and that all structural panels were made of 7000 series aluminium alloy with a density value of 2,780 kg/m^3, an elastic modulus value of 73.1 GPa and a Poisson's ratio value of 0.33. The thickness distributions were determined using structural optimisation that used material failure constraints only and a single 2.5g load, including inertial and fuel load relief. The resulting mass of the simple wingbox model was reported to be 12,263 kg. The initial wing mass estimated from the structural optimisation performed before the start of the aerostructural optimisation was 30,286 kg. The aircraft was assumed to have an initial take-off gross mass of 299,375 kg, a fuel burn mass of 112,276 kg, a wingspan of 58.8 m and an aspect ratio of 9.0. The aerostructural design optimisation results show that the wingspan increased to 68.9 m with an aspect ratio of 12.6 and the take-off gross mass and the fuel burn mass decreased to 290,142 kg and 102,345 kg, respectively. The total structural mass of the wing increased to 30,983 kg.

In Klimmek's work [10] on the development of a structural finite element model for the generic aircraft configuration FERMAT, the NASA Common Research Model is used as the geometry of the FERMAT configuration. A parametric modelling approach and methods from computer-aided geometric design were used in the development of the complete structure of the aircraft. A design process was established that included the parametric modelling part, load analysis and the sizing of the structure considering structural strength, buckling and aeroelastic constraints.

The wingbox was modelled using a detailed finite element model and metallic material. The wingbox thin panels (skins, spar webs and ribs) were modelled using shell elements, while the wingbox flanges (stiffeners and spar caps) were modelled using bar elements. A symmetric pull-up manoeuver load case with a 2.5g load factor was used for sizing the wingbox structures. Detailed information

about the sizing process, comprising the definition of the design variables, objective function and constraints can be found in [10]. The total wing mass calculated by Klimmek was 31,089 kg. This value was calculated using a sizing process that included setting up the structural model of the FERMAT configuration, then setting up all simulations and optimisation models in terms of components. In his work, Klimmek compared the value of the total mass of the wing with the mass value of 33,144 kg estimated according to [162].

On the other hand, the mass value of the wingbox was estimated using three sizing steps. In the first step, which is called preliminary cross-section sizing, the structural properties of the wingbox components were sized based on cutting loads and the wingbox mass was calculated to be 11,040 kg. For the second and third steps, where mathematical optimisation algorithms were applied using MSC.Nastran Sol 200, the wingbox mass values were calculated to be 11,134 kg under stress and buckling constraints and 11,494 kg under aileron effectiveness constraints, respectively.

In Table 7.14, the values of the total mass of the CRM wing and the wingbox mass in the current study are compared with the estimated mass values according to the literature. It should be noted that no mass values were reported for the composite CRM wing in the open literature. Generally, the total mass value of the metallic CRM wing calculated in the current study is in good agreement with the values estimated by Klimmek and Kenway et al., and with the 12% rule. Eqns. (7.27) and (7.28) overestimate the metallic CRM wing total mass. On the other hand, the CRM wingbox mass calculated in the current study is lower than the masses reported in the literature.

Table 7.14: Comparison of the results for the metallic CRM wing mass (kg)

Method	Wingbox Mass [kg]	Wing Total Mass [kg]
Current study	10,371	30,754
Klimmek	11,040 - 11,134 - 11,494	31,089 - 33,144
Kenway et al.	12,263	30,286
12% rule	----------	31,200
Eqn. (7.27)	----------	40,052
Eqn. (7.28)	----------	38,186

Discrepancies have been observed between the wing mass calculated in the current study and the mass values according to the literature. Possible sources for

these discrepancies can be traced to the use of an oversimplified geometry model for the wingbox; the location of the spars and the number of ribs, as well as their spacing and location, also have a direct effect on the wingbox mass. Flight conditions for the calculation of sizing loads and/or inaccurate aerodynamic loads, the definition and number of design variables and constraints in the scenario of using optimisation techniques, and finally a strong reliance on empirical relation methods for the mass estimation may also be reasons for the discrepancies.

7.4.3 Case Study III

The purpose of this case study is to look into the advantages of considering the dynamic aeroelastic stability constraint (flutter) at early stages of the design process. The CRM wing considered in the second case study is modified to have airfoil sections with the same twist angle along the semi-span of the wing to enable it to be used in flutter analysis. Therefore, the chord lines of the airfoils at the root and tip wing sections were rotated in a spanwise direction with respect to the chord line of the airfoil at the kink wing section to produce a similar geometrical twist angle of 0.8°. The modified CRM wing is first optimised subject to static strength and stiffness constraints and manufacturing constraints only, and is then optimised to meet the requirements of the dynamic aeroelastic constraint, the static strength and stiffness constraints and the manufacturing constraints simultaneously. The results of both cases, including the optimised masses and flutter speeds, were compared in order to more accurately assess the advantages of considering the dynamic aeroelastic stability constraint at early stages of the design process.

7.4.3.1 Aerodynamic Loading on the Modified CRM Wing

The aerodynamic loads have been recalculated to account for the effects of the wing geometrical twist modifications. Figures 7.26 and 7.27 compare the spanwise distributions of the local overall lift and pitching moment calculated about a local quarter chord of the CRM wing configurations.

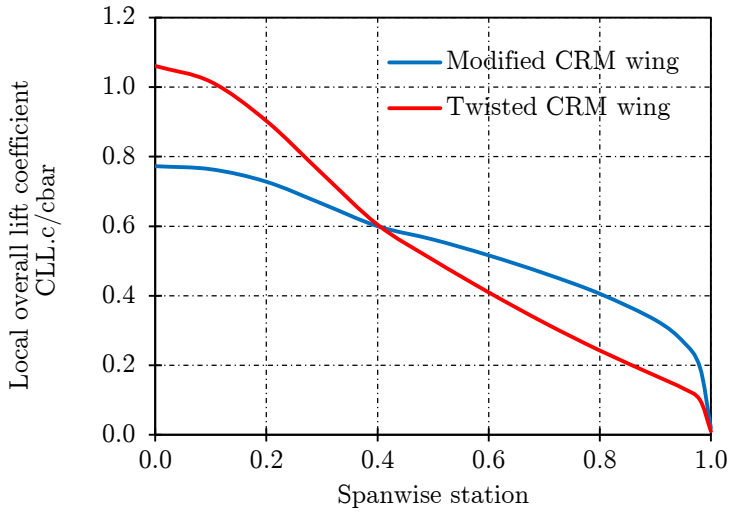

Figure 7.26: Spanwise distribution of the local overall lift coefficient

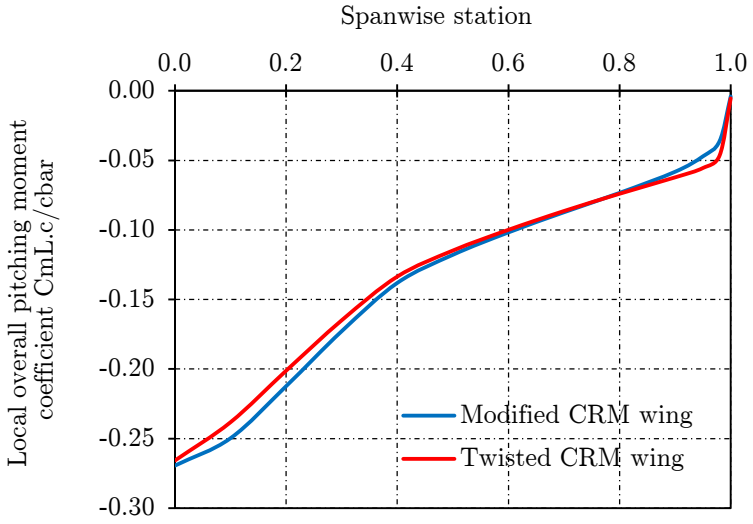

Figure 7.27: Spanwise distribution of the local overall pitching moment coefficient

From Figure 7.26, one can observe that changing the wing twist changes the local overall lift coefficient distribution, and thus the spanwise lift distribution will also change. While the local overall lift coefficient distribution of the modified CRM wing decreases towards the wing root, it increases towards the wingtip just after the wing kink point. As a result, the distributed lift load becomes too highly weighted at the wingtip, modifying the bending moment distribution over the wing and changing the structural mass of the wing. On the other hand, as can be seen from Figure 7.27, the difference in the spanwise distributions of the local

overall pitching moment coefficient for both CRM wing configurations is negligible. The pitching moment coefficient measured about the aerodynamic centre of the airfoil (25% of the chord) is independent of the angle of attack and therefore does not vary with it, or at least does not vary significantly over the operating range of the angle of attack of the airfoil.

7.4.3.2 Optimisation Results of the CRM Wingbox Subject to Static Strength, Stiffness and Manufacturing Constraints

The wing design process and optimisation procedure for the current case study followed a similar approach to the second case study. However, it was found to be convenient to relax the upper limit of the vertical wingtip displacement constraint to more than the initial assigned value of 15% of the wing semi-span. Therefore, the wingtip vertical displacement was assigned a new upper limit of 17% of the wing semi-span. This does not increase the value of the objective function in the wing mass minimisation problem or perturb the feasible design domain.

The wingtip vertical displacement constraint was modified because changing the wing twist has an effect on the distributions of the local overall lift coefficient and lift over the wingspan. It also results in an increase in the wingtip incidence (wash-in) with respect to the wing root, compared to the negative twist angle value at the wingtip (wash-out) of the original twisted CRM wing. The increase in the wingtip incidence will increase the effective angle of attack and therefore increase the local overall lift coefficient. The new lift distribution will affect the stress/strain distributions over the wingbox and will affect the wingbox tip deformations as a result.

Tables 7.15 and 7.16 give the optimised masses of the modified CRM wingbox for both the metallic and composite configurations and for both the continuous and discrete optimisation solutions. During the optimisation process, hard convergence is obtained along with a hard feasible discrete design solution. The bold values in Tables 7.15 and 7.16 represent the local minimum optimised solution obtained using discrete values for the design variables. However, it is worth mentioning that only one feasible discrete design solution was obtained for the modified composite CRM wing. The rest of the discrete designs were unfeasible. The response output that is responsible for the maximum constraint violation and thus for the unfeasible discrete designs was traced by screening the results of the design responses. It was seen that the minimum ply orientation percentage value

obtained for a number of design variables was less than the minimum allowable value of 10%, and as a result a discrete unfeasible design is obtained. This again shows the importance of using different initial guesses for the design variables in order to achieve feasible local optimum designs in the gradient-based optimisation solutions. From Tables 7.15 and 7.16 it also can be seen that the wingbox structural masses of the modified CRM wing are larger than the wingbox masses of the twisted CRM wing (see Tables 7.5 and 7.6). Such results are as expected and are in agreement with the comments and discussions provided in the previous section.

Table 7.15: Optimised masses (kg) of the modified metallic CRM wingbox

Design variable initial values				
Min	25% Max	50% Max	75% Max	Max
Continuous solution				
13,168	13,422	13,303	13,388	13,342
Discrete solution				
13,265	13,523	13,401	13,486	13,441

Table 7.16: Optimised masses (kg) of the modified composite CRM wingbox

Design variable initial values				
Min	25% Max	50% Max	75% Max	Max
Continuous solution				
10,420	10,528	10,869	11,031	11,256
Discrete solution				
10,837	**10,954**	11,289	11,465	11,665

Table 7.17 summarises the maximum tip displacement value in the optimised CRM wingbox model for both the metallic and composite configurations, as well as the change in the wingtip twist angle from the baseline modified wing model.

Table 7.17: Deformation values of the optimised modified CRM wingbox models

Deformation	Metallic	Composite
Displacement $\delta_{tip(Z)}$	4.99 m	3.48 m
Twist Θ_{tip}	0.42°	3.77°

With respect to the displacement $\delta_{tip(Z)}$ results of the wingbox models presented in Table 7.17, the same conclusions hold as were already mentioned in the discussion of Table 7.7. For both wingbox models, the difference in the wingtip twist, going from the baseline model to the optimised model, shows that the wingtip twists upwards. The composite wingbox twists more than the metallic wingbox, which indicates that the torsional stiffness of the composite wingbox is less than the metallic one. This can be improved by using more 45° fibres in the laminate. The minimum 45° ply orientation percentage within a laminate can be bounded by a lower limit greater than the 10% value used in the optimisation study.

7.4.3.3 Flutter Analysis of the Optimised CRM Wingbox Subject to Static Strength, Stiffness and Manufacturing Constraints

A free vibration analysis is first performed to determine the natural frequencies and mode shapes of the optimised CRM wingbox. Computation of shape modes and natural frequencies is carried out using the normal mode analysis module of MSC.Nastran with the Lanczos method [138]. The resulting global mode shapes and corresponding natural frequencies of the optimised modified metallic and composite CRM wingboxes are presented in Tables 7.18 and 7.19, respectively. The analysis was performed on the CRM wingbox models with full fuel and zero fuel loading.

Table 7.18: Global mode shapes and the associated frequencies of the optimised modified metallic CRM wingbox

Mode Number	Mode Shape Description	Natural Frequency [Hz] (Full Fuel)	Natural Frequency [Hz] (Zero Fuel)
1	1st Out-of-Plane Bending	1.07	1.65
2	2nd Out-of-Plane Bending	3.12	4.28
3	1st Lateral Bending	3.39	5.51
4	3rd Out-of-Plane Bending	4.57	8.79
5	1st Torsion	19.02	19.19

Table 7.19: Global mode shapes and the associated frequencies of the optimised modified composite CRM wingbox

Mode Number	Mode Shape Description	Natural Frequency [Hz] (Full Fuel)	Natural Frequency [Hz] (Zero Fuel)
1	1st Out-of-Plane Bending	1.39	2.28
2	2nd Out-of-Plane Bending	3.72	5.63
3	1st Lateral Bending	4.44	7.52
4	3rd Out-of-Plane Bending	6.21	11.01
5	1st Torsion	23.40	24.79

Comparison of the global mode shapes shows that the natural frequencies of the optimised composite wingbox are higher than those for the optimised metallic wingbox. The fuel masses located in the inboard and outboard portions of the wingbox lowered the structural frequency of the wing bending in contrast to when the fuel tanks were empty. Generally, fuel quantity can affect the flutter modes and speed and therefore the most critical conditions should be tested.

Aeroelastic stability analysis is then performed for the optimised modified CRM wingbox using the *p-k* method at sea-level conditions. The flutter type of aeroelastic instability is detected in the subsonic regime using non-matched flutter analysis. The aerodynamic forces are calculated for one reference value of Mach number M_{Ref} and for a set of reduced frequencies at fixed altitude. The input values for the reference flutter critical flight altitude and Mach number are generally chosen at sea level and at maximum design dive speed (V_D = 221.7 m/s EAS), respectively. The Doublet Lattice Method integrated in MSC.Nastran is used to calculate the unsteady aerodynamic forces. The flutter speed of the optimised modified metallic CRM wingbox with full fuel tanks is determined as 370 m/s with a corresponding flutter frequency of 4.42 Hz, and with zero fuel the speed is determined as 306 m/s with a corresponding flutter frequency of 4.18 Hz. The damping and frequency curves of the modified metallic CRM wingbox are shown in Figures 7.28 and 7.29, respectively.

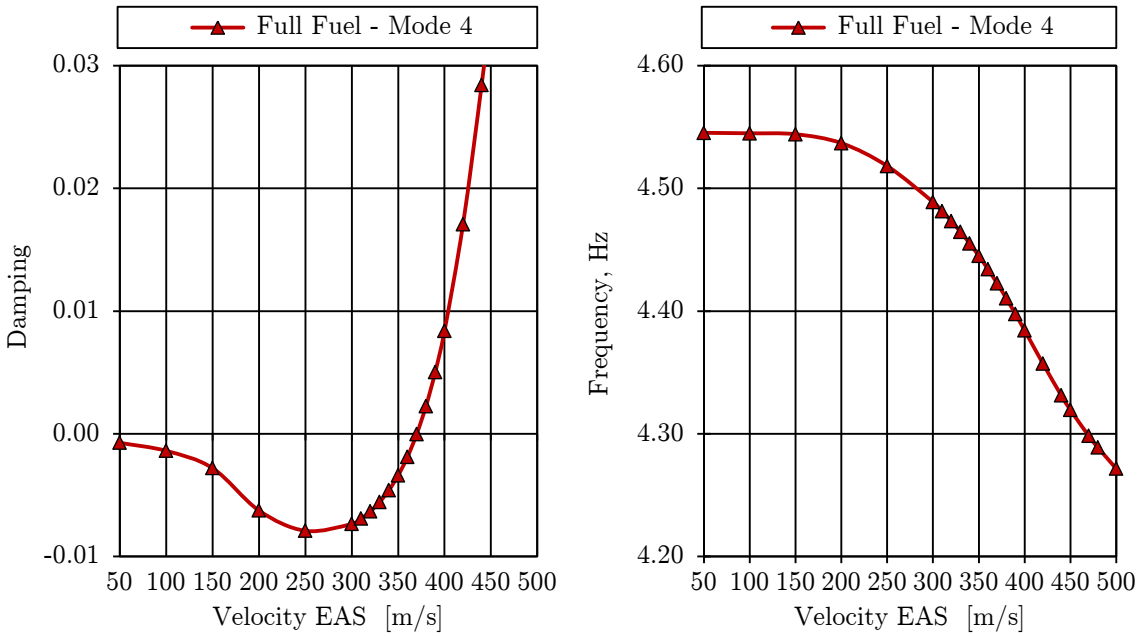

Figure 7.28: Velocity versus damping and velocity versus frequency plots of the optimised modified metallic CRM wingbox - full fuel

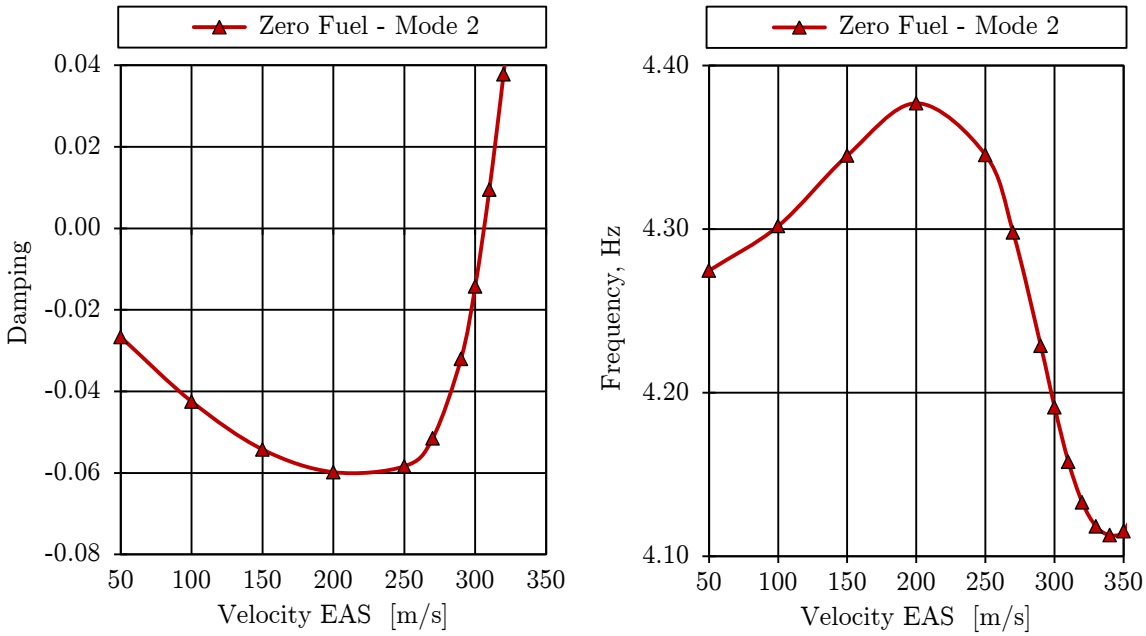

Figure 7.29: Velocity versus damping and velocity versus frequency plots of the optimised modified metallic CRM wingbox - zero fuel

On the other hand, the flutter speed of the optimised modified composite CRM wingbox with full fuel tanks is determined as 428 m/s with a corresponding flutter frequency of 6.42 Hz, and with zero fuel the speed is determined as 394 m/s with a corresponding flutter frequency of 5.80 Hz. The damping and frequency curves of the modified composite CRM wingbox are shown in Figures 7.30 and 7.31, respectively.

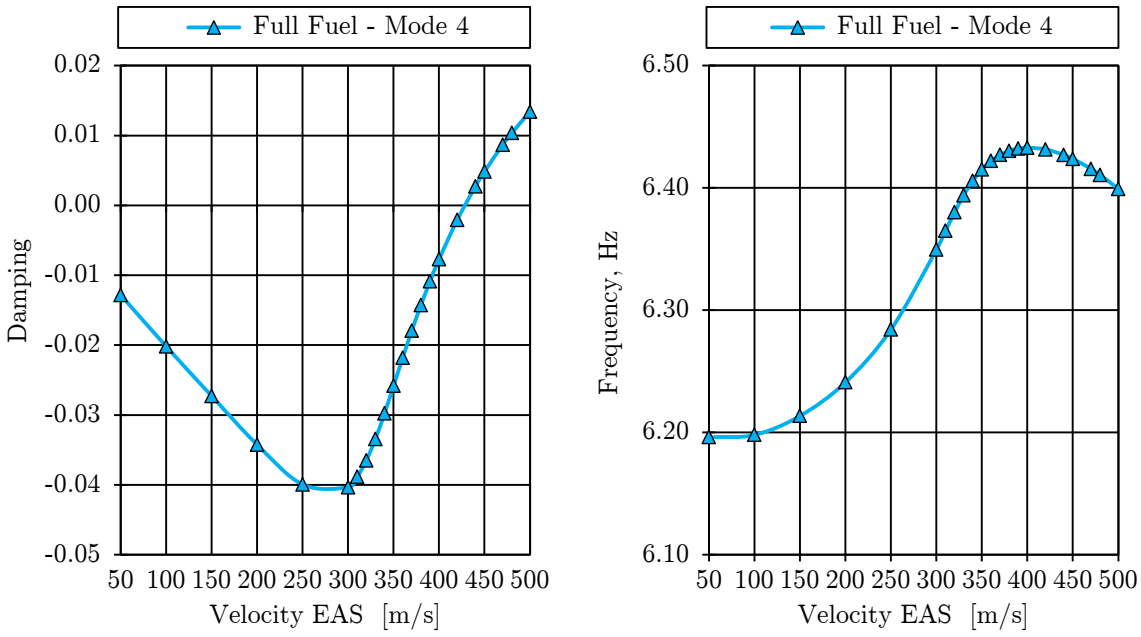

Figure 7.30: Velocity versus damping and velocity versus frequency plots of the optimised modified composite CRM wingbox - full fuel

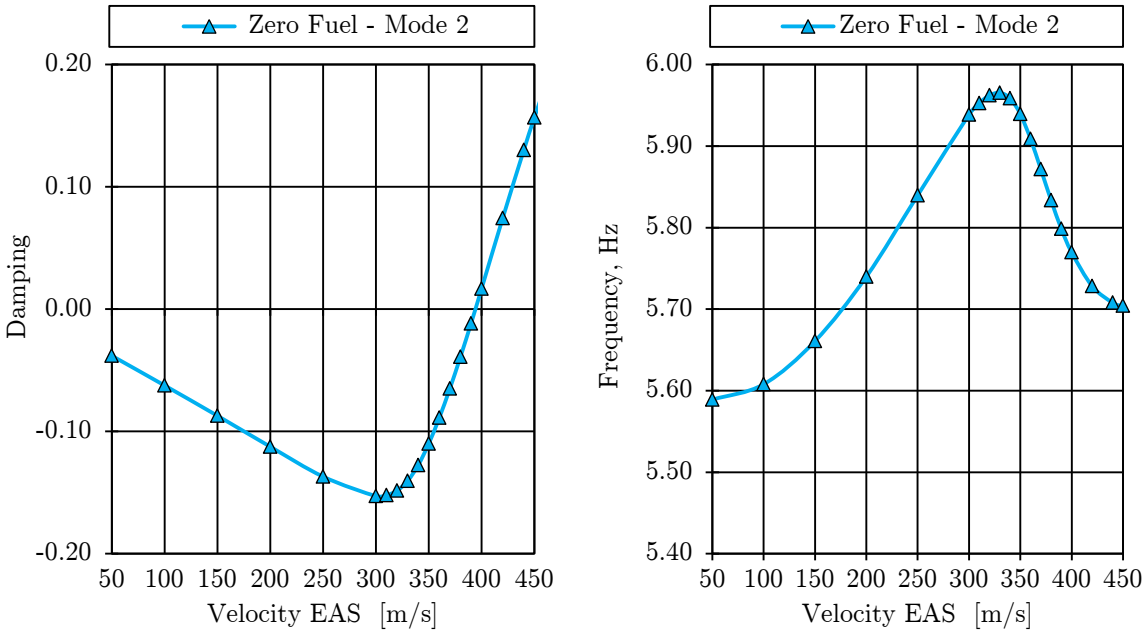

Figure 7.31: Velocity versus damping and velocity versus frequency plots of the optimised modified composite CRM wingbox - zero fuel

The results show that the optimised modified metallic and composite CRM wings are free from flutter instabilities ($V_{Flutter} > 256$ m/s). From the results it can also be seen that the flutter speed of the optimised modified composite wing is higher than for the metallic one. The results of the flutter speed, which is itself a function of the static displacement, agree with the displacement results previously presented in Table 7.17. The high displacement results give a good indication of the flexural stiffness of the wingbox. In addition to the structural stiffness, the flutter speed is found to be highly dependent on the mass quantity of the fuel in the wing fuel tanks. The lowest flutter speed, which is critical to the design, is associated with the empty fuel tanks loading conditions. The flutter results verify that the stiffness constraints work fine and that the wing is free from flutter. The stiffness of the wingbox was controlled by limiting the displacement and the twist of the wingtip to ensure adequate aeroelastic response.

7.4.3.4 Optimisation Results of the CRM Wingbox Subject to Static Strength, Stiffness, Aeroelastic and Manufacturing Constraints

In order to look into the advantages of considering the dynamic aeroelastic stability constraint (flutter) at early stages of the design process, the modified CRM wing is optimised to meet the requirements of the static strength and

stiffness constraints, the dynamic aeroelastic constraint and the manufacturing constraints simultaneously. In order to be able to compare the results with the findings in the previous section, it was considered reasonable to run the optimisation problem using the same starting point that provided a feasible optimum discrete solution.

Table 7.20 gives the optimised masses of the modified CRM wingbox for both the metallic and composite configurations and for both the continuous and discrete optimisation solutions. During the optimisation process, hard convergence is obtained along with a hard feasible discrete design solution.

Table 7.20: Optimised masses (kg) of the modified CRM wingbox (flutter constraint included)

Design variable initial values	
Metallic (Min)	Composite (25% Max)
Continuous solution	
13,393	9,931
Discrete solution	
13,498	10,340

Table 7.21 summarises the maximum tip displacement value and the change in wingtip twist angle from the baseline wing model in the optimised modified CRM wingbox model for both the metallic and composite configurations.

Table 7.21: Deformation values of the optimised modified CRM wingbox models (flutter constraint included)

Deformation	Metallic	Composite
Displacement $\delta_{tip(Z)}$	4.97 m	3.45 m
Twist Θ_{tip}	0.0°	4.19°

The results from Table 7.20 show that the mass of the optimised modified metallic CRM wingbox has increased as compared to the results obtained by only considering static strength, stiffness and manufacturing constraints only. This is not the case for the optimised modified composite CRM wingbox. The deformation results presented in Table 7.21 show that the wingtip deflection as well as the twist angle of the optimised modified metallic CRM wingbox has decreased and as a result the wingbox structural mass has increased. On the other

hand, while the wingtip deflection of the optimised modified composite has decreased, the wingtip twist angle has increased. The increase in the wingtip twist indicates that the torsional stiffness of the optimised modified composite CRM wingbox has decreased and as a result reduced the structural mass of the composite wingbox.

A free vibration analysis is performed to determine the natural frequencies and mode shapes of the optimised modified CRM wingbox models. The resulting global mode shapes and the corresponding natural frequencies of the optimised modified metallic and composite CRM wingboxes are presented in Tables 7.22 and 7.23, respectively. The analysis was performed on the CRM wingbox models with full fuel and zero fuel loading.

Table 7.22: Global mode shapes and the associated frequencies of the optimised modified metallic CRM wingbox (flutter constraint included)

Mode Number	Mode Shape Description	Natural Frequency [Hz] (Full Fuel)	Natural Frequency [Hz] (Zero Fuel)
1	1st Out-of-Plane Bending	1.07	1.63
2	2nd Out-of-Plane Bending	3.04	4.55
3	1st Lateral Bending	3.47	5.49
4	3rd Out-of-Plane Bending	6.83	8.83
5	1st Torsion	18.68	19.30

Table 7.23: Global mode shapes and the associated frequencies of the optimised modified composite CRM wingbox (flutter constraint included)

Mode Number	Mode Shape Description	Natural Frequency [Hz] (Full Fuel)	Natural Frequency [Hz] (Zero Fuel)
1	1st Out-of-Plane Bending	1.40	2.31
2	2nd Out-of-Plane Bending	3.75	4.98
3	1st Lateral Bending	3.99	7.40
4	3rd Out-of-Plane Bending	6.25	10.96
5	1st Torsion	23.09	24.32

An aeroelastic stability analysis is performed for the optimised modified CRM wingbox models to verify that the optimum design is free from flutter. The flutter speed of the metallic CRM wingbox with full fuel tanks is determined as 399 m/s with a corresponding flutter frequency of 6.87 Hz, and with zero fuel the speed is

determined as 351 m/s with a corresponding flutter frequency of 5.00 Hz. Note that a 14.7% increase in the critical flutter speed at zero fuel has been achieved at the cost of a 1.8% increase in the total wingbox structural mass. The damping and frequency curves of the optimised modified metallic CRM wingbox at the lowest flutter speed are shown in Figure 7.32.

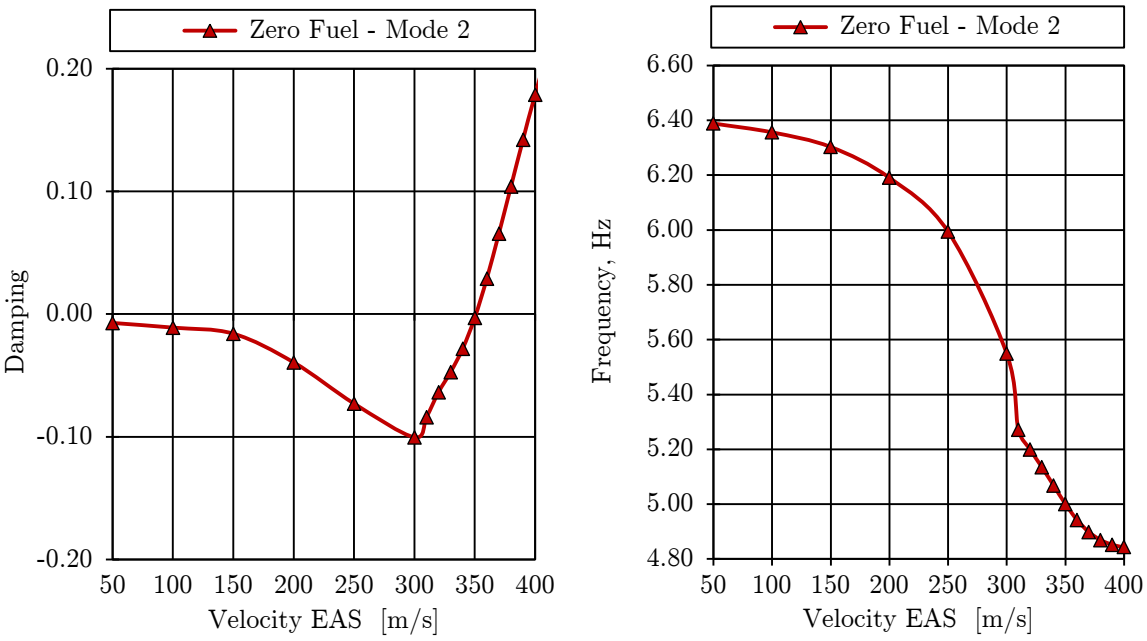

Figure 7.32: Velocity versus damping and velocity versus frequency plots of the optimised modified metallic CRM wingbox (flutter constraint included)

On the other hand, the flutter speed of the optimised modified composite CRM wingbox with full fuel tanks is determined as 432 m/s with a corresponding flutter frequency of 8.10 Hz, and with zero fuel the speed is determined as 373 m/s with a corresponding flutter frequency of 6.04 Hz. Note that a 5.6% decrease in the total wingbox structural mass has been achieved at the cost of a 5.3% decrease in the critical flutter speed at zero fuel. Although the flutter speed has decreased, the wing design is free from flutter. There is no doubt that with the added versatility of the composite material, the stiffness distribution has been tailored during the optimisation process to avoid flutter and to achieve a minimum mass design by controlling the thickness of each lamina of the wingbox structural panels. The damping and frequency curves of the optimised modified composite CRM wingbox at the lowest flutter speed are shown in Figure 7.33.

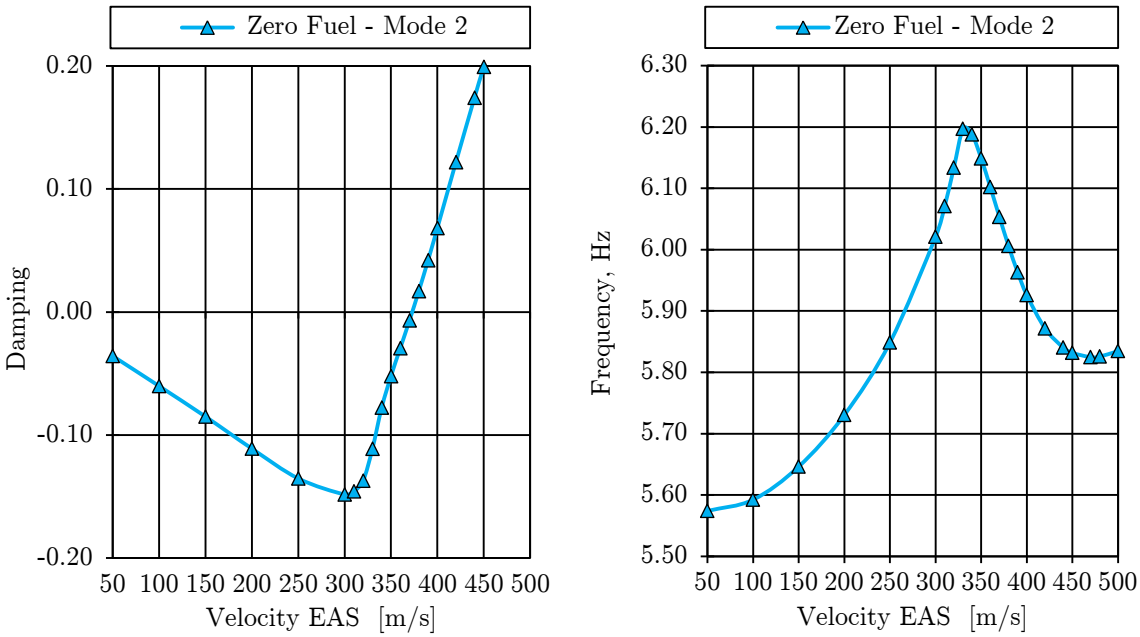

Figure 7.33: Velocity versus damping and velocity versus frequency plots of the optimised modified composite CRM wingbox (flutter constraint included)

7.4.4 Case Study IV

The aim of this case study is to demonstrate the efficiency and reliability of the proposed practical optimisation framework and enhanced strategy, as described in Chapter 6, in improving the chances of finding a better optimum solution than already found, or in finding a feasible optimum solution when traditional techniques and methods have failed.

The CRM wingbox considered in the third case study is optimised to meet static strength and stiffness requirements and manufacturing constraints. Five different initial starting point values are used for the design variables during the optimisation process. MSC.Nastran Sol 200 is used for the sizing optimisation of the wingbox model. A number of fully stressed design cycles are performed at the beginning of the optimisation process, followed by a number of continuous and discrete optimisation cycles. Both optimisation algorithms, DOT and MSCADS, are individually used to solve the optimisation problem. Then the estimated solution is updated on an iteration-by-iteration basis with the aim of improving the optimum value of the mass of the CRM wingbox model.

Table 7.24 shows the optimised masses of the metallic CRM wingbox using different starting values for the design variables along with different optimisation algorithms. In all solutions, convergence is achieved along with feasible discrete designs. The bold value denotes the local minimum solution obtained.

Table 7.24: Optimised masses of the metallic CRM wingbox with different optimisation algorithms

Solution Type	Optimised Mass (kg)				
	Min	25%	50%	75%	Max
MSCADS-MMFD-1	13,518	13,337	13,560	13,188	13,407
DOT-MMFD-1	13,265	13,523	13,401	13,486	13,441
MSCADS-MMFD-2	**13,078**	13,156	13,186	13,171	13,170
DOT-MMFD-2	13,240	13,174	13,353	13,228	13,247

Figure 7.34 illustrates the results of the first and second optimisation iterations obtained using the DOT and MSCADS algorithms for the metallic CRM wingbox model.

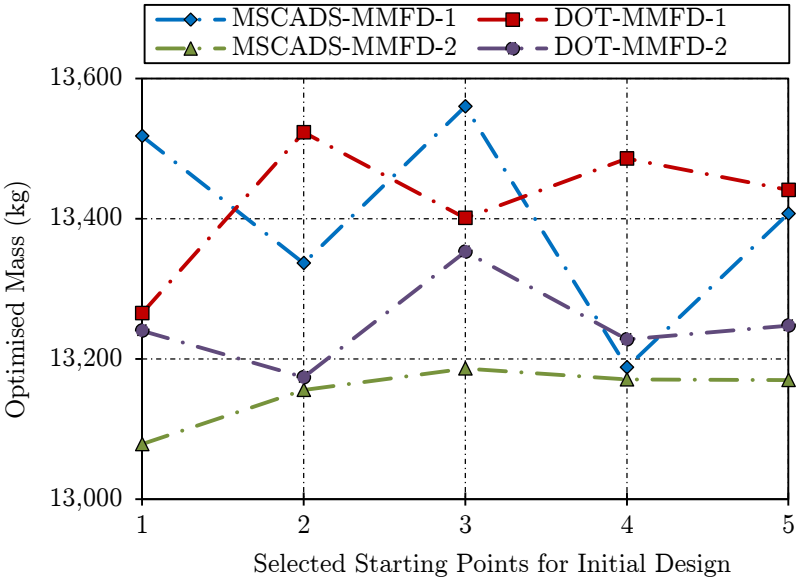

Figure 7.34: Mass of the optimised metallic CRM wingbox using an iterative procedure between algorithms

Table 7.25 shows the optimised masses of the composite CRM wingbox, using different starting values for the design variables along with different optimisation algorithms. The bold values refer to the discrete feasible solutions that have been obtained for the composite CRM wingbox.

Table 7.25: Optimised masses of the composite CRM wingbox with different optimisation algorithms

Solution Type	Optimised Mass (kg)				
	Min	25%	50%	75%	Max
MSCADS-MMFD-1	8,816	8,824	8,591	8,704	13,486
DOT-MMFD-1	10,837	**10,954**	11,289	11,465	11,665
MSCADS-MMFD-2	8,389	8,480	**8,788**	**8,564**	8,415
DOT-MMFD-2	**8,798**	**8,806**	**8,550**	**8,750**	**10,630**

Figure 7.35 illustrates the results of the first and second optimisation iterations obtained using the DOT and MSCADS algorithms for the composite CRM wingbox model.

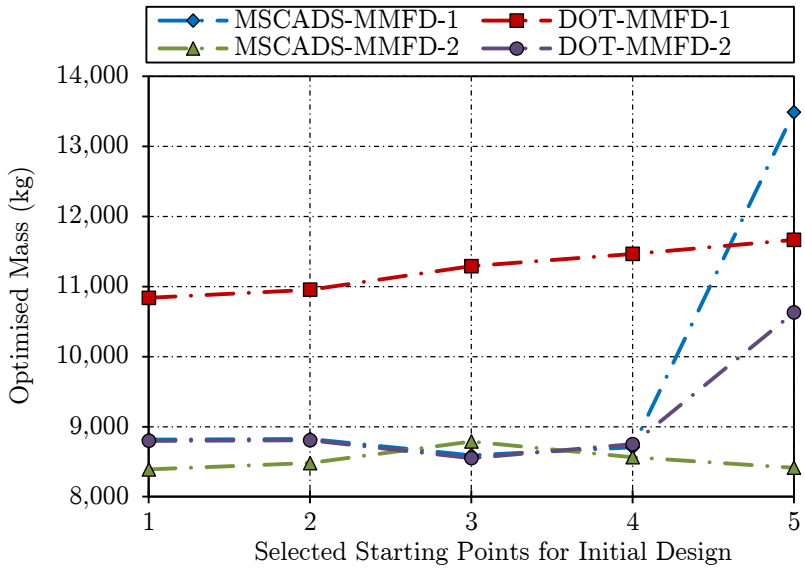

Figure 7.35: Mass of the optimised composite CRM wingbox using an iterative procedure between algorithms

From the results presented in Tables 7.24 and 7.25 and illustrated in Figures 7.34 and 7.35, the following observations can be made. In the gradient-based optimisation problem, using different starting values for the design variables can lead to local optimum designs, since the optimised wingbox configurations do not have exactly the same mass. Similarly, different gradient-based algorithms used to perform the same optimisation problem terminate at different local optima, and thus return different solutions even for the same initial starting values for the

design variables. It is also observed that optimum solutions are not restricted to extreme or corner points of the research design space.

From Table 7.24 and Figure 7.34, it can be seen that the minimum optimised mass of the metallic CRM wingbox is obtained using the MSCADS-MMFD-2 iterative solution with a value of 13,078 kg. Comparing this value with the related optimised value obtained earlier in the third case study (13,265 kg), it can be seen that the value of the objective function against the initial optimised value has improved.

The results in Table 7.25 show that the value of the objective function of the composite CRM wingbox is case-sensitive to both the choice of the optimisation algorithm and the starting values for the design variables. For instance, using the MSCADS algorithm in the first run of the optimisation obtained infeasible discrete solutions. On the other hand, by using the DOT algorithm in the first run, a feasible discrete design was obtained. Not only have the chances of finding feasible discrete solutions increased in the second run, but the value of the objective function against the initial optimised value has also improved. The minimum optimised mass of the composite CRM wingbox is obtained using the DOT-MMFD-2 iterative solution with a value of 8,550 kg, compared to the initial optimised mass of 10,954 kg.

The change in the optimised value as a result of switching between the different optimisation algorithms at each iteration step is more noticeable in the composite material case than in the metallic case. It is likely that each optimisation algorithm has completely different search routes from the initial to the final point with the output as the solution. Moreover using composite construction materials rather than metallic ones will dramatically expand the size and complexity of the design space, thereby increasing the number of solutions that a designer can choose from with the aim of improving the overall structural performance of the wing components with minimum structural mass penalty.

Chapter 8

Conclusions and Future Work

8.1 General Conclusions

In this thesis, a new framework for estimating the structural mass of a transport aircraft wing via finite element multidisciplinary analysis and design optimisation techniques has been developed. To this end, the multidisciplinary static strength and stiffness, dynamic aeroelastic stability, and manufacturing constraints are simultaneously addressed within an optimisation environment through a gradient-based search algorithm. A practical optimisation procedure has been also presented as part of the sizing optimisation process, with enhanced features in solving large-scale nonlinear structural optimisation problems, incorporating an effective initial design variable value generation scheme based on the concept of the fully stressed design. The applicability and accuracy of the proposed framework and practical optimisation procedure is illustrated through their application to four case studies in which the wingbox structure of the public domain NASA wing - commonly referred to as the Common Research Model (CRM) - is designed and optimised using four different wingbox models of increasing structural complexity to produce a minimum mass design.

The results of the research studies demonstrate that the new aircraft wing mass estimation framework can successfully tackle problems related to realistic aircraft wing design optimisation, negotiating the highly constrained, nonlinear design search space, and presenting the designer with a range of designs. This gives an insight into the competence of certain wingbox models in predicting the mass of the metallic and composite primary wing structures to an acceptable level of

accuracy, and demonstrates the trade-off between the wingbox structural complexity models under consideration and the computational resources necessary in order to achieve the required degree of accuracy.

In a scenario where high-fidelity structural models are used to describe and represent the CRM wingbox, these models do indeed attempt to improve the optimised masses of the wingbox. This representation of the CRM wingbox increases the number of structural elements describing the wingbox from one model to the next. Thus, the number of design variables increases, and the design space enlarges. The possible design alternatives within the design domain then increase, which in turn increases the chances of arriving at a better local optimum solution and mass estimate. The optimised masses of the composite wingbox models indicate that the results are more sensitive to the initial starting values of the design variables than to the results of the metallic wingbox models. In this case, the change in the optimised masses of the composite wingbox models is larger than the change for the metallic wingbox. This behaviour can be explained by the different mechanical properties of the composite laminate, which are more complex than those of metallic structures. The computational times for the optimised composite models are long and the design space is relatively complex, with a large number of design variables and constraints compared to the optimised metallic models.

Comparisons were made between the mass estimation results of the metallic CRM wingbox models and the composite models in order to identify and select an appropriate model to predict the mass of the primary wing structure to an acceptable level of accuracy. These comparisons revealed that in the case of the second wingbox model of structural fidelity, a preliminary estimate of the metallic CRM wingbox mass can be performed with a high degree of confidence as long as the gradient-based designs are also optimised using a sufficient number of different initial values for the design variables. This practice was observed in the design and optimisation phase of this study. Moreover, the mass of the metallic CRM wingbox can be estimated with an acceptable level of accuracy and reduced computational time. This is not, however, the case for the composite CRM wingbox mass estimate. Where composite materials were used as the primary construction material for the design of the CRM wingbox, it was observed that by increasing the structural fidelity of the wingbox model, the discrepancy in the mass estimate became smaller but still significant, as observed in the second and third wingbox models. Therefore, it is strongly recommended that the fourth

wingbox model should be used as a baseline model for the preliminary estimate of the composite CRM wingbox mass, as it requires a higher computational time in order to achieve the required accuracy level.

The lower-mass wingbox design (found by taking into account all the loads acting on the wingbox structures) proved the importance of considering not only the lift force but also the pitching moment and inertial loads during the CRM wingbox mass estimation process. In addition to this, it can be seen from the breakdown of the CRM wing mass results (Chapter 7, Sec. 7.4.2.2) that the mass of the wing primary structures is a large contributor to the overall mass of the CRM wing. It is important to ensure, therefore, that the mass of the wing primary structures is estimated using appropriate methods and approaches, which serve to guarantee the accuracy and quality of the results. The results also show that the total structural mass saving for the composite CRM wing over the metallic wing is around 21.5%. The values of the total mass of the metallic CRM wing and the wingbox mass calculated in the current study are generally in good agreement with the values according to the literature, although some discrepancies have been observed. Possible sources for these discrepancies can be traced to the use of an oversimplified geometry model for the wingbox; the location of the spars and the number of ribs, as well as their spacing and location, also have a direct effect on the wingbox mass. Flight conditions for the calculation of sizing loads and/or inaccurate aerodynamic loads, the definition and number of design variables and constraints in the scenario of using optimisation techniques, and finally a strong reliance on empirical relation methods for the mass estimation may also be reasons for the discrepancies.

A case study into minimising the mass of the CRM wingbox structures and obtaining a flutter-free wingbox model for a prescribed set of flight conditions, with a defined damping level in the final design proved the advantage of considering dynamic aeroelastic stability constraints in the early stages of the design process, especially in the case of composite aircraft wing designs. A 5.6% decrease in the structural mass of the total composite CRM wingbox was achieved at the cost of a 5.3% decrease in critical flutter speed. The design continues to be flutter-free within the flight envelope.

The application of the practical optimisation procedure, as part of the sizing optimisation process, increased the efficacy of the local search algorithms of MSC.Nastran Sol 200 in obtaining feasible discrete and optimal wingbox mass

designs, and improved the chances of finding a better optimum solution than already found, or in finding a feasible optimum solution when traditional techniques and methods have failed. Its performance is illustrated through the application of a case study in which the metallic and composite fourth wingbox models are optimised for a design of minimum mass. It is revealed that the change in the optimised mass value - as a consequence of using different starting values for the design variables, as well as switching between different gradient-based algorithms in deriving the local optimum at each iteration step - is more appreciable in the case of the composite construct than in the case of the metallic. It is anticipated, therefore, that each optimisation algorithm will have completely different search routes from the initial to final points, with the output as the solution. Moreover, using composite construction materials will dramatically alter the size of the design space, thereby increasing the number of solutions available to a designer, with the aim of improving the overall structural performance of the wing components.

8.2 Recommendations for Future Work

In view of the above, and for a more detailed insight into the wing mass estimation framework based on multidisciplinary analysis and design optimisation techniques, the following recommendations are made.

1. Further studies that account for the bending stiffness of the wingbox flanges (spar caps/stiffeners) could be performed. The flanges can be idealised by beam elements with defined cross-sections.

2. The use of optimisation techniques such as design variable linking is recommended in order to reduce the number of independent design variables.

3. In the course of this work, challenges were often encountered regarding the choice of the appropriate gradient-based optimisation algorithm and its effect on the quality and accuracy of the results, as well as on the computational cost. Therefore, other gradient-based algorithms and commercial optimisation tools could be investigated.

4. The optimisation model could be extended to include more design constraints, such as constraints on the fundamental frequency, local buckling, divergence speed, fatigue and thermal stresses.

5. Further work could be performed to demonstrate the application of a multidisciplinary analysis and design optimisation framework in order to analyse a hybrid wingbox structure that uses both composite and metallic construction materials for the components of the primary wing structures. Nevertheless, a nonconventional internal wing structure can be used and its effects on the optimised mass and structural behaviour of the wingbox can be investigated.

6. The optimisation model could be extended to perform a multi-objective aerodynamic and structural optimisation. Constraints could be imposed on the wing's leading edge sweep angle, taper ratio and aspect ratio. Several useful Pareto optimal designs can be seek out for the preliminary design of the CRM wing.

Bibliography

[1] Belobaba, P., & Odoni, A. (2009). Introduction and Overview. In P. Belobaba, A. Odon, & C. Barnhart (Eds.), *The Global Airline Industry* (pp. 1-3). Chichester, UK: John Wiley & Sons, Ltd.

[2] Frediani, A., & Oliviero, F. (2012). Conceptual Design of a Very Large PrandtlPlane Freighter. In G. Buttazzo, & A. Frediani (Eds.), *Variational Analysis and Aerospace Engineering: Mathematical Challenges for Aerospace Design* (Vol. 66, pp. 305-321). Springer US.

[3] Kroo, I. (2005). *Nonplanar Wing Concepts for Increased Aircraft Efficiency - VKI lecture series on Innovative Configurations and Advanced Concepts for Future Civil Aircraft.* USA: Stanford University.

[4] Washburn, A. (2010). NASA's Current Plans for ERA Airframe Technology. *48th AIAA Aerospace Sciences Meeting.* Orlando, Florida.

[5] Ciampa, P. D., Zill, T., Pfeiffer, T., & Nagel, B. (2011). A Functional Shape Parameterization Approach for Preliminary Optimization of Unconventional Aircraft. *3rd CEAS Air & Space Conference.* Venice.

[6] Rossow, C.-C. (2010). Aerodynamics - A discipline swept away? *The Aeronautical Journal, 114,* (1160), 599-609.

[7] Hansen, H. (2010). Laminar Flow Technology - The AIRBUS View. *27th International Congress of the Aeronautical Sciences.* Nice.

[8] Schneider, O., Kreth, S., & Bertsch, L. (2010). Towards a Quiet Short Take-Off and Landing Transportation System: Concept Evaluation and ATM Integration. *International Powered Lift Conference.* Philadelphia, PA: American Helicopter Society International, Inc.

[9] NASA. (2015). *NASA Successfully Tests Shape-Changing Wing for Next Generation Aviation.* Retrieved March 18, 2016, from http://www.nasa.gov/press-release/nasa-successfully-tests-shape-changing-wing-for-next-generation-aviation

[10] Klimmek, T. (2014). Parametric Set-Up of a Structural Model for FERMAT Configuration for Aeroelastic and Loads Analysis. *ASDJournal, 3,* (2), 31-49.

[11] Jutte, C. V., Stanford, B. K., & Wieseman, C. D. (2015). *Internal Structural Design of the Common Research Model Wing Box for Aeroelastic Tailoring.* Hampton, Virginia: NASA.

[12] Raymer, D. P. (2006). *Aircraft Design: A Conceptual Approach* (4th ed.). Washington, USA: AIAA Education Series.

[13] Roskam, J. (1989). *Airplane Design: Part III - Layout Design of Cockpit, Fuselage, Wing and Empennage: Cutaways and Inboard Profiles.* Kansas: Roskam Aviation and Engineering Corporation.

[14] Torenbeek, E. (1982). *Synthesis of Subsonic Airplane Design.* Amsterdam: Delft University Press.

[15] Howe, D. (2000). *Aircraft Conceptual Design Synthesis.* London: Professional Engineering Publishing Limited London and Bury St Edmunds.

[16] Murphy, N. (1987). *Analytical Wing Weight Prediction/Estimation Using Computer Based Design Techniques.* PhD Thesis, Cranfield Institute of Technology.

[17] Ardema, M., Chambers, M., Patron, A., Hahn, A., Miura, H., & Moore, M. (1996). *Analytical Fuselage and Wing Weight Estimation of Transport Aircraft.* NASA.

[18] Kundu, A. (2010). *Aircraft Design.* Cambridge: Cambridge University Press.

[19] Elham, A. (2013). *Weight Indexing for Multidisciplinary Design Optimization of Lifting Surfaces.* PhD Thesis, Delft University of Technology.

[20] Glatt, C. (1974). *WAATS - A Computer Program for Weights Analysis of Advanced Transportation Systems.* NASA.

[21] Torenbeek, E. (1992). *Development and Application of a Comprehensive Design Sensitive Weight Prediction Method for Wing Structures of Transport Category Aircraft.* Delft University of Technology.

[22] Howe, D. (1996). The Prediction of Aircraft Wing Mass Part G. *Journal of Aerospace Engineering, 210*, 135-145.

[23] Ritter, R. C. (1960). Rib Weight Estimation by Structural Analysis. SAWE Paper No. 259, *19th Annual National Conference.* Hollywood, California: Society of Allied Weight Engineers, Inc.

[24] Burt, M. E. (1955). *Weight Prediction for Wings of Box Construction.* RAE Report Structures No. 186.

[25] Shanley, F. (1950). *Weight-Strength Analysis of Aircraft Structures.* New York: Dover Publication Inc.

[26] Spath, R. (1954). A Simple Wing Weight Estimation Equation. SAWE Paper No. 98, *13th National Conference.* Baltimore, Maryland: Society of Allied Weight Engineers, Inc.

[27] John St., R. S. (1969). The Derivation and Application of Analytical-Statistical Weight Prediction Techniques. SAWE Paper No. 810, *28th Annual Conference.* San Francisco, California: Society of Allied Weight Engineers, Inc.

[28] Lewis, L. E., & St. John, R. S. (1975). Allowable Stress Estimation Methods for Preliminary Design Weight Prediction. SAWE Paper No. 1044, *34th Annual Conference.* Seattle, Washington: Society of Allied Weight Engineers, Inc.

[29] Anderson, W., & Udin, S. (1991). Wing Mass Formula for Subsonic Aircraft. *Journal of Aircraft, 29, No. 4: Engineering Notes,* 725-727.

[30] Ajaj, R. M., Smith, D., & Isikveren, A. T. (2013). A conceptual wingbox weight estimation model for transport aircraft. *Aeronautical Journal, 177* (1191), 533-551.

[31] Macci, S. H. (1995). Semi-Analytical Method for Predicting Wing Structural Mass. SAWE Paper No. 2282, *54th Annual Conference.* Huntsville, Alabama: Society of Allied Weight Engineers, Inc.

[32] Elham, A., Rocca, G. L., & Tooren, M. J. (2013). Development and implementation of an advanced, design-sensitive method for wing weight estimation. *Aerospace Science and Technology, 29*, 100-113.

[33] Bookham, J. (1973). *Improved Methods of Structure Weight Prediction, Civil Aircraft Wing Weights Part 1 and 2.* Weybridge: British Aircraft Corporation Ltd, Civil Aircraft Division and Hatfield: Hawker Siddeley Aviation Ltd.

[34] Dijk, G. (1987). *Development of a wing weight prediction method.* Haarlem: Haarlem Institute of Technology.

[35] Terpstra, A. (2002). *Wing Weight Prediction in the Preliminary Design Phase.* Delft University of Technology.

[36] Kelm, R., Lapple, M., & Grabietz, M. (1995). Wing Primary Structure Weight Estimation of Transport Aircrafts in the Pre-Development Phase. SAWE Paper No. 2283, *54th Annual Conference.* Huntsville, Alabama: Society of Allied Weight Engineers, Inc.

[37] Velden, A., Kelm, R., Kokan, D., & Mertens, J. (2000). Application of MDO to large subsonic transport aircraft. AIAA 2000-0844. *38th Aerospace Science Meeting & Exhibit.* Reno, NV: AIAA.

[38] Nisbet, J., & Hoy, J. (1976). A New Role for Structures Technology in Aircraft Configuration Development. ASME PAPER 76-WA/AERO-8.

[39] Hutton, J. G., & Richmond, L. D. (1979). Application of Finite Element Analysis to Derivation of Structural Weight. SAWE Paper No. 1271, *38th Annual Conference.* New York, New York: Society of Allied Weight Engineers, Inc.

[40] Pincha, P. J. (1982). Algorithmic Mass-Factoring of Finite Element Model Analysis. SAWE Paper No. 1451, *41st Annual Conference.* San Jose, California: Society of Allied Weight Engineers, Inc.

[41] Droegkamp, M. (1992). Finite Element Model Weight Estimation. SAWE Paper No. 2089, *51st Annual Conference.* Hartford, Connecticut: Society of Allied Weight Engineers, Inc.

[42] Zaidel, S. J. (1992). A-12 Structural Target Weight Distribution Using the Finite Element Model (FEM). SAWE Paper No. 2110, *51st Annual Conference.* Hartford, Connecticut: Society of Allied Weight Engineers, Inc.

[43] Mitchell, P. M. (1993). Advanced Finite Element Weight Estimation Process on the High Speed Civil Transport. SAWE Paper No. 2169, *52nd*

Annual Conference. Biloxi, Mississippi: Society of Allied Weight Engineers, Inc.

[44] Sensmeier, M., Stewart, B., & Samareh, J. (2006). Rapid Generation and Assessment of Aircraft Structural Topologies for Multidisciplinary Optimization and Weight Estimation. *Collection of Technical Papers - AIAA/ASME/ASCE/AHS/ASC structures, structural dynamics and materials conference*, *7*, pp. 4722-4733.

[45] Bindolino, G., Ghiringhelli, G., Ricci, S., & Terraneo, M. (2010). Multilevel Structural Optimization for Preliminary Wing-Box Weight. *Journal of Aircraft, 47, No. 2*, 475-489.

[46] Hurlimann, F., Kelm, R., Dugas, M., Oltmann, K., & Kress, G. (2010). Mass estimation of transport aircraft wingbox structures with a CAD/CAE-based multidisciplinary process. *Aerospace Science and Technology, 15* (4), 323-333.

[47] Dorbath, F., Nagel, B., & Gollnick, V. (2012). A Knowledge Based Approach for Extended Physics-Based Wing Mass Estimation in early Design Stages. *28th Congress of the International Council of the Aeronautical Sciences. 6.* Brisbane: ICAS.

[48] Wenzel, J., Sinapius, U., & Gabbert, U. (2012). Primary Structure Mass Estimation in Early Phases of Aircraft Development using the Finite Element Method. *CEAS Aeronautical Journal, 3* (1), 35-44.

[49] Seywald, K. (2012). Wing Mass Prediction Considering Quasi-Static Nonlinear Aeroelasticity. *PEGASUS-AIAA Student Conference VIII Edition.* Poitiers.

[50] Wolkovitch, J. (1986). The joined wing: An overview. *Journal of Aircraft, 23*, 161-178.

[51] Hajela, P. (1984). *Weight Evaluation of the Joined Wing Configuration.* Technical Report. CR-166592: NASA.

[52] Miura, H., Shyu, A., & Wolkovitch, J. (1985). Parametric Weight Evaluation of Joined Wings by Structural Optimization. *Journal of Aircraft, 25*, 1142-1149.

[53] Blair, M., & Canfield, R. A. (2002). A Joined-Wing Structural Weight Modeling Study. *43rd AIAA/ASME/ASCE/AHS/ASC Structures, Structural Dynamics, and Materials Con.* Denver, Colorado: AIAA.

[54] Heinze W. *Ein Beitrag zur quantitativen Analyse der technischen und wirtschaftlichen Auslegungsgrenzen verschiedener Flugzeugkonzepte für den Transport großer Nutzlasten*, PhD Thesis, TU Braunschweig, ZLR Forschungsbericht 94-01, 1994.

[55] Osterheld, C., Heinze, W., & Horst, P. (2001). Preliminary Design of a Blended Wing Body Configuration using the Design Tool PrADO. *Proceedings of the CEAS Conference on Multidisciplinary Aircraft Design and Optimisation.* Cologne.

[56] Werner-Westphal, C., Heinze, W., & Horst, P. (2008). Structural sizing for an unconventional, environment-friendly aircraft configuration within integrated conceptual design. *Aerospace Science and Technology, 12* (2), 184-194.

[57] Doherty, J., & Parker, N. (1994). Dual Point Design of a Supersonic Transport Wing using a Constrained Optimization Method. *7th European Aerospace Conference - The Supersonic Transport of Second Generation.* Toulouse.

[58] Dean, S. R. (2008). Multi-disciplinary Design Optimization: Development & Application at QinetiQ. *KATnet II Multi Disciplinary Design & Configuration Optimization Workshop.*

[59] Wasiutynski, Z., & Brandt, A. (1963). The Present State of Knowledge in the Field of Optimum Design of Structures. *Applied Mechanics Reviews, 16* (5), 341-350.

[60] Schmit, L. A. (1981). Structural synthesis - Its genesis and development. *AIAA Journal, 19* (10), 1249-1263.

[61] Vanderplaats, G. N. (1982). Structural Optimization-Past, Present, and Future. *AIAA Journal, 20* (7), 992-1000.

[62] Maxwell, C. (1952). Scientific Papers. *2*, 175-177.

[63] Michell, A. G. (1904). The limits of economy of material in frame-structures. *Philosophical Magazine Series 6, 8* (47), 589-597.

[64] Dantzig, G. B. (1948). *Programming in Linear Structures.* Washington D. C.: Comptroller, U.S.A.F.

[65] Heyman, J. (1956). Plastic Design of Beams and Frames for Minimum Material Consumption. *Quarterly of Applied Mathematics, 8*, 373-381.

[66] Schmit, L. A. (1960). Structural Design by Systematic Synthesis. *Proceedings of the 2nd Conference ASCE on Electronic Computation* (pp. 105-122). Reston, VA: American Society of Civil Engineers.

[67] Gellatly, R. H., Berke, L., & Gibson, W. (1971). The use of Optimality Criterion in Automated Structural Design. *3rd Air Force Conference on Matrix Methods in Structural Mechanics.* Wright Patterson AFB, OH.

[68] Venkayya, V. B. (1971). Design of Optimum Structures. *Computers and Structures* (No.1), 265-309.

[69] Prager, W., & Taylor, J. E. (1968). Problems in Optimal Structural Design. *Journal of Applied Mechanics, 36* (1), 102-106.

[70] Schmit, L. A., & Farshi, B. (1974). Some Approximation Concepts for Structural Synthesis. *AIAA Journal, 12* (5), 692-699.

[71] Starnes Jr, J. R., & Haftka, R. T. (1979). Preliminary Design of Composite Wings for Buckling, Stress and Displacement Constraints. *Journal of Aircraft, 16* (8), 564-570.

[72] Haug, E. J., Choi, K. K., & Komkov, V. (1986). Design Sensitivity Analysis of Structural Systems. *Mathematics in Science and Engineering, 177.*

[73] Haftka, R. T., & Adelman, H. M. (1989). Recent developments in structural sensitivity analysis. *Structural Optimization, 1*, 137-151.

[74] Brennan, J. (1999). Integrating Optimization into the Design Process. *Proceedings of the Altair HyperWorks Technology Showcase.* London.

[75] Cervellera, P. (2004). Optimization Driven Design Process: Practical Experience on Structural Components. *Proceedings of the 14th Convegno Nazionae ADM.* Bari.

[76] Gartmeier, O., & Dunne, W. L. (1999). Structural Optimization in Vehicle Design Development. *MSC. Worldwide Automotive Conference.*

[77] Krog, L., Tucker, A., & Rollema, G. (2002). Application of Topology, Sizing and Shape Optimization Methods to Optimal Design of Aircraft Components. *3rd Altair UK HyperWorks Users Conference.*

[78] Krog, L., Tucker, A., Kempt, M., & Boyd, R. (2004). Topology Optimization of Aircraft Wing Box Ribs, AIAA-2004-4481. *Proc. 10th AIAA/ISSMO Symposium on Multidisciplinary Analysis and Optimization.* Albany, NY.

[79] Schumacher, G., Stettner, M., Zotemantel, R., O'Leary, O., & Wagner, M. (2004). Optimization Assisted Structural Design of New Military Transport Aircraft, AIAA-2004-4641. *Proc. 10th AIAA MAO Conference.* Albany, NY.

[80] Gerard, G. (1966). Optimum Structural Design Concepts for Aerospace Vehicles. *Journal of Spacecraft, 3* (1), 5-18.

[81] Ashley, H. (1982). On Making Things the Best-Aeronautical Uses of Optimization. *Journal of Aircraft, 19* (1), 5-28.

[82] Butler, R. (1998). The Optimization of Wing Structures. *Aircraft Engineering and Aerospace Technology, 70* (1), 4-8.

[83] Rao, S. S. (1982). *Automated Optimum Design of Wing Structures.* Technical Memorandum 84475, NASA.

[84] Dababneh, O., & Kayran, A. (2014). Design, analysis and optimization of thin walled semi-monocoque wing structures using different structural idealization in the preliminary design phase. *International Journal of Structural Integrity, 5* (3), 214-226.

[85] Krone, J. J. (1975). Divergence Elimination with Advanced Composites. AIAA paper 75-1009.

[86] Edwin, L. (1958). Application of Practical Optimization Techniques in the Preliminary Structural Design of Forward-Swept Wing. *Second International Symposium on Aeroelasticity and Structural Dynamics.* Aachen.

[87] Green, A. J. (1987). Aeroelastic Tailoring of Aft-Swept High-Aspect-Ratio. *Journal of Aircraft, 24* (11), 812-819.

[88] Eastep, E. F., Tischler, V. V., & Khot, S. N. (1999). Aeroelastic Tailoring of Composite Structures. *Journal of Aircraft, 36* (6), 1041-1047.

[89] Gurdal, Z., Haftka, R. T., & Hajela, P. (1999). *Design and Optimization of Laminated Composite Materials.* New York, NY: Wiley-Interscience.

[90] Kameyama, M., & Fukunaga, H. (2007). Optimum Design of Composite Plate Wings for Aeroelastic Characteristics using Lamination Parameters. *Computers and Structures, 85* (3-4), 213-224.

[91] Dillinger, S. K., Abdalla, M. M., Klimmek, T., & Gurdal, Z. (2013). Static Aeroelastic Stiffness Optimization and Investigation of Forward Swept Composite Wings. *10th World Congress on Structural and Multidisciplinary Optimization*. Orlando, Florida.

[92] Popelka, D., Lindsay, D., Parham Jr, T., Berry, V., & Baker, D. J. (1995). Results of an Aeroelastic Tailoring Study for a Composite Tiltrotor Wing. *51st American Helicopter Society Annual Forum*. Fort Worth, Texas.

[93] Lottati, I. (1985). Flutter and Divergence Aeroelastic Characteristics for Composite Forward Swept Cantilevered Wing. *Journal of Aircraft, 22* (11), 1001-1007.

[94] Weisshaar, T. A., & Foist, B. F. (1983). Vibration and Flutter of Advanced Composite Lifting Surfaces. AIAA Paper 83-0961.

[95] Sobieszczanski-Sobieski, J., & Haftka, R. T. (1997). Multidisciplinary Aerospace Design Optimization: Survey of Recent Developments. *Structural Optimization, 14* (1), 1-23.

[96] Martins, J. R., & Lambe, A. B. (2013). Multidisciplinary design optimization: A survey of architectures. *AIAA Journal, 51* (9), 2049-2075.

[97] Haftka, R. T., Sobieski, S., & Padula, S. L. (1992). On Options for Interdisciplinary Analysis and Design Optimization. *Structural Optimization, 4*, 65-74.

[98] Peter, J. R., Dimitri, N. M., & Daniel, P. S. (1995). Combined Aerodynamic and Structural Optimization of High Speed Civil Transport Wing. AIAA-95-1222. *36th AIAA Structures, Dynamics, and Materials Conference.* New Orleans, LA.

[99] Grossman, B., Strauch, G. J., Eppard, W. M., Gurdal, Z., & Haftka, R. T. (1986). Integrated Aerodynamic Structural Design of Sailplane Wing. *AIAA/AHS/ASEE/ Aircraft Systems Design and Technology Meeting Conference.* Dayton, OH.

[100] Jha, R., & Chattopadhyay, A. (1999). Multidisciplinary Optimization of Composite Wings Using Refined Structural and Aeroelastic Analysis Methodologies. *Engineering Optimization, 32* (1), 59-78.

[101] Brugh, R. L. (1989). *NASA Structural Analysis System (NASTRAN).* Washington, DC: NASA.

[102] Wilkinson, K., Markowitz, J., Lerner, E., George, D., & Batill, S. M. (1977). FASTOP: A Flutter and Strength Optimization Program for Lifting Surface. *Journal of Aircraft, 14* (6), 581-587.

[103] Neill, D. J., Johnson, E. H., & Canfield, R. (1990). ASTROS - A Multidisciplinary Automated Structural Design Tool. *Journal of Aircraft, 27* (12), 1021-1027.

[104] Dodd, A. J., Kadrinka, K. E., Loikkanen, M. J., Sikes, B. A., Strong, R. C., & Tzong, T. J. (1990). Aeroelastic Optimization Program. *Journal of Aircraft, 27* (12), 1028-1036.

[105] Collier, C. S., Peckenheim, M., & Yarrington, P. W. (1997). Next Generation Structural Optimization Today. *MSC Aerospace Users.*

[106] *ALTAIR OPTISTRUCT User's Manual Ver. 13.0.* (2014). Troy, MI: Altair Engineering. Inc.

[107] *GENESIS User's Manual Ver. 13.1.* (2014). Colorado Springs, CO: Vanderplaats Research and Development. Inc.

[108] Kohnke, P. (1994). *ANSYS Theory Reference Manual.* Canonsburg, PA: ANSYS. Inc.

[109] Goldberg, D. E. (1989). *Genetic Algorithms in Search, Optimization and Machine Learning* (1st ed.). Boston, MA: Addison-Wesley Longman Publishing Co., Inc.

[110] Gill, P., Murray, W., & Saunders, M. (2002). SNOPT: An SQP Algorithm for Large Scale Constrained Optimization. *SIAM Journal on Optimization, 12* (4), 979-1006.

[111] Dennis Jr, J. E., & Schnabel, R. B. (1983). *Numerical Methods for Unconstrained Optimization and Nonlinear Equations.* Englewood Cliffs, NJ: Prentice Hall.

[112] Kogiso, N., Watson, L. T., Gurdal, Z., & Haftka, R. T. (1994). Genetic Algorithms with Local Improvement for Composite Laminate Design. *Structural Optimization, 7* (3), 207-218.

[113] Liu, B., Haftka, R. T., Akgun, M. A., & Todoroki, A. (1998). Permutation Genetic Algorithm For Stacking Sequence Design of Composite Laminates. *39th AIAA/ASME/ASCE/AHS Structures, Structure Dynamics and Material Conference.* Long Beach, CA.

[114] Gwin, L. B., & Taylor, R. F. (1973). A General Method for Flutter Optimization. *AIAA Journal, 11* (2), 1613-1617.

[115] Karpel, M. (1992). Multidisciplinary Optimization of Aeroservoelastic Systems Using Reduced-Size Models. *Journal of Aircraft, 29* (5), 939-946.

[116] Zingg, D. W., Nemec, M., & Pulliam, V. H. (2008). A Comparative Evaluation of Genetic and Gradient-Based Algorithms Applied to Aerodynamic Optimization. *European Journal of Computational Mechanics, 17* (1-2), 103-126.

[117] Dorbath, F., Nagel, B., & Gollnick, V. (2010). Comparison of Beam and Shell Theory for Mass Estimation in Preliminary Wing Design. *2nd Aircraft Structural Design Conference.* London: Royal Aeronautical Society (RAeS).

[118] Locatelli, D. (2012). *Optimization of Supersonic Aircraft Wing-Box Using Curvilinear SpaRibs.* PhD Thesis, Blacksburg, Virginia: Virginia Polytechnic Institute and State University.

[119] Vasiliev, V., Barynin, V., & Razin, A. (2012). Anisogrid composite lattice structures - Development and aerospace applications. *Composite Structures, 94* (3), 1117-1127.

[120] Ediger, K., Zeumer, C., & Dugas, M. (2004). *FAME-liA 4.00 F3 - Validation Document.* Technical Report, Airbus Deutschland GmbH.

[121] Hurlimann, F. (2010). *Mass Estimation of Transport Aircraft Wingbox Structures with a CAD/CAE-Based Multidisciplinary Process.* PhD Thesis, ETH Zurich.

[122] ESDU. (1999). *Computer program for estimation of spanwise loading of wings with camber and twist in subsonic attached flow. Lifting-surface theory.* Retrieved March 12, 2014, from https://www.esdu.com/cgi-bin/ps.pl?sess=cranfield5˙1160220142018cql&t=doc&p=esdu˙95010c

[123] Tomas, M. (2000, 12). *User's guide and reference manual for Tornado.* Retrieved March 12, 2014, from http://www.tornado.redhammer.se/index.php/documentation/documents

[124] Kroo, I. *Aircraft Design: Synthesis and analysis.* Retrieved April 20, 2014, from http://adg.stanford.edu/aa241/AircraftDesign.html

[125] EASA. (2015). *Certification Specifications and Acceptable Means of Compliance for Large Aeroplanes CS-25, Amendment 16.* Retrieved March 28, 2015, from http://easa.europa.eu/system/files/dfu/CS-25 20Amdendment 16.pdf

[126] Vassberg, J. C., DeHaan, M. A., Rivers, S. M., & Wahls, R. A. (2008). Development of a Common Research Model for Applied CFD Validation Studies, AIAA Paper 2008-6919. *AIAA Applied Aerodynamics Conference.* Honolulu, HI.

[127] Bruhn, F. E. (1973). *Analysis and Design of Flight Vehicle Structures.* Jacobs Pub.

[128] Megson, T. H. (2013). *Aircraft Structures for Engineering Students* (5th ed.). Elsevier Ltd.

[129] Peery, D. J. (1950). *Aircraft Structures* (1st ed.). New York: McGraw Hill.

[130] FAA. *FAR 25, Airworthiness Standards: Transport Category Airplanes* (*Title 14 CFR Part 25*). Retrieved January 15, 2014, from http://flightsimaviation.com/data/FARS/part˙25.html

[131] Moran, J. (1984). *An Introduction to Theoretical and Computational Aerodynamics.* New York: John Wiley & Sons, Inc.

[132] Milne-Thomson, L. M. (1966). *Theoretical Aerodynamics* (4th ed.). New York: Dover Publications.

[133] ASM. (1978). *ASM Aerospace Specification Metals, Aluminum 7050-T7451.* Retrieved June 12, 2014, from http://asm.matweb.com/search/SpecificMaterial.asp?bassnum=MA7050T745

[134] ASM. (1978). *ASM Aerospace Specification Metals, Aluminum 2024-T3.* Retrieved June 12, 2014, from http://asm.matweb.com/search/SpecificMaterial.asp?bassnum=%20MA2024T3

[135] Soni, S. R. (1980). *Elastic Properties of T300/5208 Bidirectional Symmetric Laminates - Technical Report Afwal-Tr-80-4111.* Ohio 45433: Materials Laboratory - Air Force Wright Aeronautical Laboratories - Air Force Systems Command.

[136] Niu, M. C. (2010). *Composite Airframe Structures* (3rd ed.). Hong Kong: Conmilit Press Ltd.

[137] Schaeffer, H. G. (2001). *MSC.Nastran Primer for Linear Analysis* (2nd ed.). USA: MSC. Software Corporation.

[138] McLean, M. D. (2012). *MSC.Nastran 2012 Linear Static Analysis User's Guide.* Santa Ana, CA: MSC.Software Corporation.

[139] Mera, A. (1997). Nonlinear Strength and Stability Analysis of a Landing Gear Component. *MSC Users' Conference Proceedings.* Newport Beach, CA: MSC.Software Corporation.

[140] Hodges, D. H., & Pierce, G. A. (2014). *Introduction to Structural Dynamics and Aeroelasticity* (2nd ed.). Cambridge University Press.

[141] Fung, Y. C. (1993). *An Introduction to the Theory of Aeroelasticity.* Dover Publications, Inc.

[142] Bisplinghoff, R. L., Ashley, H., & Halfman, R. L. (1996). *Aeroelasticity.* Mineola, New York: Dover Publications, Inc.

[143] Rodden, W. P., & Johnson, E. H. (1994). *MSC.Nastran Version 68 Aeroelastic Analysis User's Guide.* California: MSC.Software Corporation.

[144] *MSC.FlightLoads and Dynamics User's Guide Version 2006.* (2006). Los Angeles, CA: MSC.Software Corporation.

[145] *MSC Nastran 2012 Design Sensitivity and Optimization User's Guide.* (2012). Santa Ana, CA: MSC.Software Corporation.

[146] Kim, H., Papila, M., Mason, W. H., Haftka, R. T., Watson, L. T., & Grossman, B. (2001). Detection and Repair of Poorly Converged Optimization Runs. *AIAA Journal, 39* (12), 2242-2249.

[147] Jones, R. M. (1999). *Mechanics of Composite Materials* (2nd ed.). Taylor & Francis.

[148] Tsai, S. W., & Hahn, H. T. (1980). *Introduction to Composite Materials.* Technomic Publishing Co.

[149] Kassapoglou, C. (2013). *Review of Laminate Strength and Failure Criteria, in Design and Analysis of Composite Structures: With Applications to Aerospace Structures.* Oxford: John Wiley & Sons Ltd.

[150] Oliver, M., Climent, H., & Rosich, F. (1999). Non Linear Effects of Applied Loads and Large Deformations on Aircraft Normal Modes. *RTO AVT Specialists' Meeting on Structural Aspects of Flexible Aircraft Control.* Ottawa.

[151] Liu, Q., Mulani, S., & Kapani, R. K. (2014). Global/Local Multidisciplinary Design Optimization of Subsonic Wing, AIAA 2014-0471. *10th AIAA Multidisciplinary Design Optimization Conference - AIAA SciTech.* National Harbor, Maryland: AIAA, Inc.

[152] Barker, D. K., Johnson, J. C., Johnson, E. H., & Layfield, D. P. (2002). Integration of External Design Criteria with MSC.Nastran Structural Analysis and Optimization. *Worldwide Aerospace Conference & Technology Showcase.* Toulouse: MSC.Software Corporation.

[153] Hajela, P. (1983). A Root Locus-Based Flutter Synthesis Procedure. *Journal of Aircraft, 20* (12), 1021-1027.

[154] Niu, M. C. (1999). *Airframe Stress Analysis and Sizing.* Conmilit Pres Ltd.

[155] Beer, F., Johnston, J. E., DeWolf, J., & Mazurek, D. (2014). *Mechanics of Materials* (7th ed.). McGraw-Hill Education.

[156] *MSC.Patran 2014, User's Guide.* (2014). Newport Beach, CA: MSC Software Corporation.

[157] Herrmann, L. R. (1976). Improved Stress Calculations for Simple Quadrilateral Elements. *Computers & Structures, 6*, 141-148.

[158] Robert, J. R., & Cooper, J. E. (2008). *Introduction to Aircraft Aeroelasticity and Loads.* Chichester: John Wiley & Sons, Ltd.

[159] Patil, M. J., & Hodges, D. H. (2000). On the Importance of Aerodynamic and Structural Geometrical Nonlinearities in Aeroelastic Behavior of High-Aspect-Ratio Wings. *41st AIAA/ASME/ASCE/AHS/ASC Structures, Structural Dynamics, and Materials Conference.* Atlanta.

[160] Kenway, G. K., & Martins, J. R. (2014). Multi-Point High-Fidelity Aerostructural Optimization of a Transport Aircraft Configuration. *Journal of Aircraft, 51* (1), 144-160.

[161] Kenway, G. K., Martins, J. R., & Kennedy, G. J. (2014). Aerostructural optimization of the Common Research Model configuration, AIAA 2014-3274. *15th AIAA/ISSMO Multidisciplinary Analysis and Optimization Conference.* Atlanta, GA: AIAA Aviation.

[162] LTH. (2006). *Luftfahrttechnisches Handbuch.* Retrieved June 12, 2015, from https://www.lth-online.de/en/working-groups/iasb-structural-analysis.html

[163] Hurlimann, B., Kelm, R., Dugas, M., & Kress, G. (2012). Investigation of local load introduction methods in aircraft pre-design. *Aerospace Science and Technology, 21*, 31-41.

[164] MATLAB. (2013). *MATLAB R2013a.* The MathWorks Inc.

[165] Grihon, S., Krog, L., & Bassir, D. (2009). Numerical Optimization applied to structure sizing at AIRBUS: A multi-step process. *International Journal for Simulation and Multidisciplinary Design Optimization, 3*, 432-442.

[166] Cheeseman, J. (2014). The Myterious Art of Weight Estimation of Large Civil Aircraft. SAWE Paper No. 3629. *73rd Annual International Conference on Mass Properties.* Long Beach, California: Society of Allied Weight Engineers, Inc.

[167] Conn, A. R., Gould, N. I., & Toint, P. L. (1992). *LANCELOT: a Fortran package for large-scale nonlinear optimization (Release A)* (Vol. 17). Springer Verlag (Heidelberg, New York): Springer Series in Computational Mathematics.

[168] Holden, C. M., & Keane, A. J. (2004). Visualization Methodologies in Aircraft Design. AIAA-2004-4449. *10th AIAA/ISSMO Multidisciplinary Analysis and Optimization Conference.* Albany, New York.

Appendices

Appendix A: The Implementation of the Optimiser Used in MSC.Nastran

This appendix presents an overview of the basic mathematical programming as applied to optimisation tasks, followed by the specifics of the algorithm used by MSCADS and DOT. Guidelines for the selection and use of these optimisers are given in [145]. In Chapter 6, the basic optimisation problem statement is first introduced, after which the mathematical expression of the design problem is formulated in terms of the objective function, imposed constraints, and design variables in Chapter 7.

A.1 Numerically Searching For an Optimum

The optimisation algorithms in MSC.Nastran belong to a family of methods generally referred to as 'gradient-based', since they use function gradients in addition to function values in order to assist in the numerical search for an optimum. The numerical search process can be summarised as follows: for a given point in the design space, we determine the gradients of the objective function and its constraints, and use this information to determine a search direction. We then proceed in this direction as far as possible, after which we investigate to see if we are at an optimum point. If we are not, we repeat the process until we can make no further improvement in our objective without violating any of the constraints.

The first step in a numerical search procedure is determining the direction in which to search. The situation may be somewhat complicated if the current design is infeasible (with one or more violated constraints) or if one or more constraints are critical. For an infeasible design, we are outside of one of the fences, to use a hill analogy. In the case of a critical design, we are standing immediately adjacent to a fence. In general, we need to know at least the gradient of our objective function and perhaps some of the constraint functions as well. The process of taking small steps in each of the design variable directions (supposing we are not restricted by the fences for this step) corresponds exactly to the mathematical concept of a first-forward finite difference approximation of a derivative. For a single independent variable, the first-forward difference is given by

$$\frac{df(x)}{dx} \cong \frac{f(x+\Delta x) - f(x)}{\Delta x}, \tag{A.1}$$

where the quantity Δx represents the small step taken in the direction x. For most practical design tasks, we are usually concerned with a vector of design variables. The resultant vector of partial derivatives, or gradient, of the function can be written as

$$\nabla F(\mathbf{X}) = \begin{Bmatrix} \frac{\partial F}{\partial x_1} \\ \cdot \\ \cdot \\ \cdot \\ \frac{\partial F}{\partial x_n} \end{Bmatrix} \cong \begin{Bmatrix} \frac{F(\mathbf{X}+\Delta x_1) - F(\mathbf{X})}{\Delta x_1} \\ \cdot \\ \cdot \\ \cdot \\ \frac{F(\mathbf{X}+\Delta x_n) - F(\mathbf{X})}{\Delta x_n} \end{Bmatrix}, \tag{A.2}$$

where each partial derivative is a single component of the dimensional vector.

Physically, the gradient vector points uphill, or in the direction of increasing objective function. If we want to minimize the objective function, we will actually move in a direction opposite to that of the gradient. The steepest descent algorithm searches in the direction defined by the negative of the objective function gradient, or

$$\mathbf{S}_{\mathrm{D}} = -\nabla F, \tag{A.3}$$

Proceeding in this direction reduces the function value most rapidly. $\mathbf{S}_\mathrm{D}$ is referred to as the search vector.

MSC.Nastran uses the steepest descent direction only when none of the constraints are critical or violated; even then, it is only used as the starting point for other, more efficient search algorithms. The difficulty in practice stems from the fact that, although the direction of steepest descent is usually an appropriate starting direction, subsequent search directions often fail to improve the objective function significantly. In MSC.Nastran we use other, more efficient methods which can be generalized for the cases of active and/or violated constraints.

Once a search direction has been determined, we proceeded 'downhill' until we collide with a fence, or until we reached the lowest point along our current path. It is important to note that this requires us to take a number of steps in this given direction, which is equivalent to a number of function evaluations in numerical optimisation. For a search direction $\mathbf{S}_\mathrm{D}$ and a vector of design variables $\mathbf{X}$, the new design at the conclusion of our search in this direction can be written as

$$\mathbf{X}^1 = \mathbf{X}^0 + \alpha^* \mathbf{S}_\mathrm{D}^1, \tag{A.4}$$

where $\mathbf{X}^0$ is the initial vector of design variables, $\mathbf{S}_\mathrm{D}^1$ is the search vector, and α^* is the value of the search parameter α that yields the optimal design in the direction defined by $\mathbf{S}_\mathrm{D}$. Equation A.4, represents a one-dimensional search since the update on $\mathbf{X}^1$ depends only on the single scalar parameter α.

This relation allows us to update a potentially huge number of design variables by varying the single parameter α. When we can no longer proceed in this search direction, we have the value of α which represents the move required to reach the best design possible for this particular direction. This value is defined as α^*. The new objective and constraints can now be expressed as

$$F^1 = F(\mathbf{X}^0 + \alpha^* \mathbf{S}_\mathrm{D}^1), \tag{A.5}$$

$$\mathrm{g}_j^1 = \mathrm{g}_j(\mathbf{X}^0 + \alpha^* \mathbf{S}_\mathrm{D}^1),\ J = 1,2,\dots,n_g \tag{A.6}$$

From this new point in the design space, we can again compute the gradients and establish another search direction based on this information. Again, we will proceed in this new direction until no further improvement can be made, repeating the process if necessary. At a certain point, we will not be able to establish a search direction that can yield an improved design. We may be at the bottom of the hill, or we may have proceeded as far as possible without crossing over a fence. In the numerical search algorithm, it is necessary to have some formal definition of an optimum. Any trial design can then be measured against this criterion to see if it is met, and if an optimum has been found. This required definition is provided by the Kuhn-Tucker conditions.

Figure A.1, shows a two design variable space with constraints $\mathbf{g}_1(\mathbf{X})$ and $\mathbf{g}_2(\mathbf{X})$ and the objectives function $F(\mathbf{X})$. The constraint boundaries are those curves for which the constraint values are both zero. A few contours of constant objective are shown as well; these can be thought of as contour lines drawn along constant elevations of the hill. The optimum point in this example is the point which lies at the intersection of the two constraints. This location is shown as $\mathbf{X}^*$.

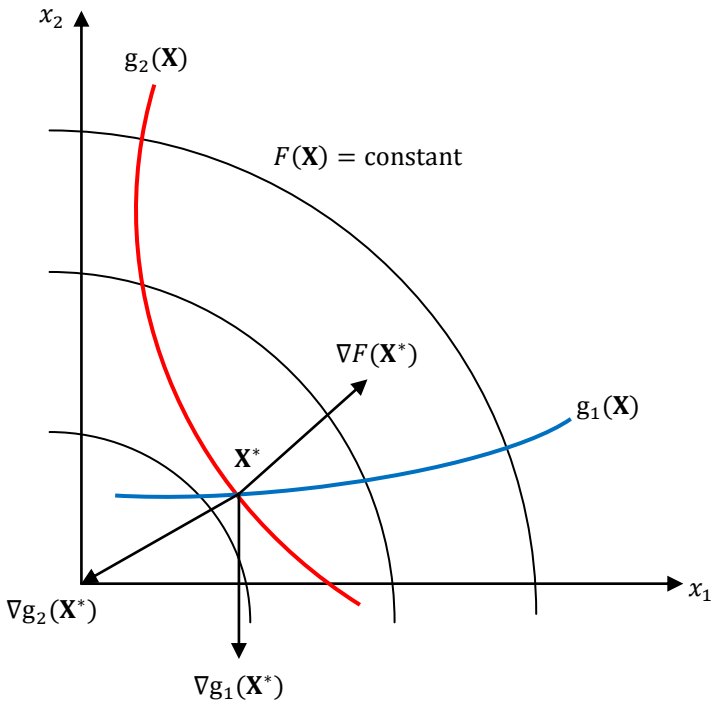

Figure A.1: Kuhn-Tucker condition at a constrained optimum

If we compute the gradients of the objective and the two active constraints at the optimum, we see that they all point off roughly in different directions (it should be remembered that function gradients point in the direction of increasing function values). For this situation - a constrained optimum - the Kuhn-Tucker conditions state that the vector sum of the objective and all active constraints must be equal to zero given an appropriate choice of multiplying factors. These factors are called the Lagrange multipliers. Constraints which are not active at the proposed optimum are not included in the vector summation.

Figure A.2 shows this to be the case, where λ_1 and λ_2 are the values of the Lagrange multipliers that enable the zero vector sum condition to be met. It is likely that we could convince ourselves that this condition could not be met for any other point in the neighboring design space.

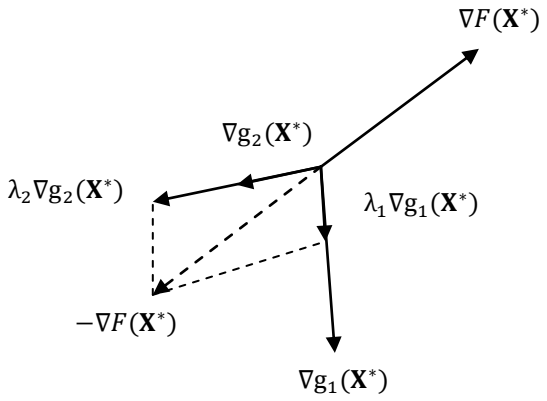

Figure A.2: Graphical interpretation of Kuhn-Tucker conditions

The Kuhn-Tucker conditions are useful even if there are no active constraints at the optimum. In this case, only the objective function gradient is considered, and this is identically equal to zero; any finite move in any direction will not decrease the objective function. A zero objective function gradient indicates a stationary condition. Not only are the Kuhn-Tucker conditions useful in determining whether we have achieved an optimal design, but they are also physically intuitive. The optimiser in MSC.Nastran tests the Kuhn-Tucker conditions in connection with the search direction determination algorithm.

A.2 Numerically Identifying the Active and Violated Constraints

The optimisation algorithm determines which of the retained constraints are violated and which are active. The constraints that are neither active nor violated can be ignored in the gradient evaluation. This reduces the amount of computations and computer memory required, as well as the size of the mathematical programming task. Figure A.3 illustrates the concept of active and violated constraints for a single inequality constraint in a simple two-design variable space.

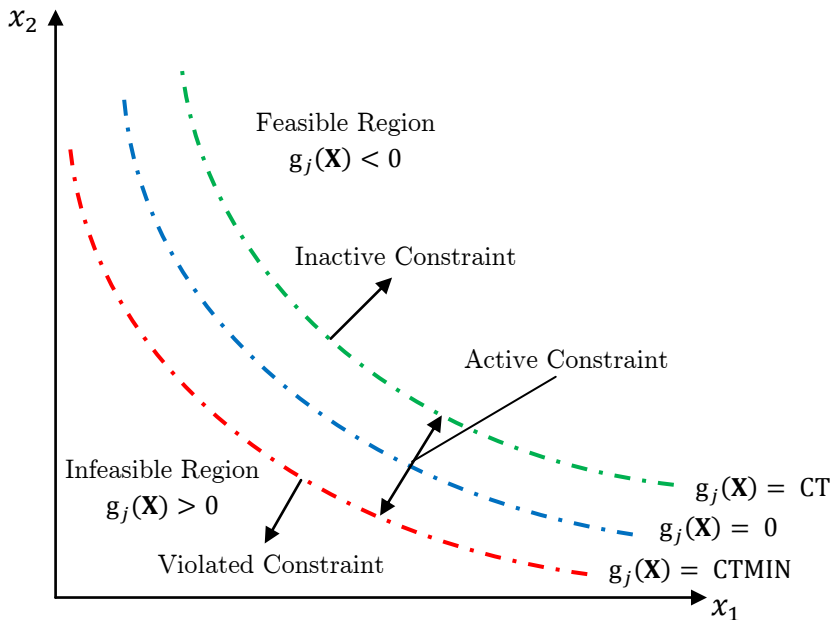

Figure A.3: Active and violated constraints

Figure A.4 presents the same information in a plot of a constraint value as a function of a single design variable or search direction. A constraint is considered active if its numerical value exceeds CT. The default value for CT is -0.03, but this can be changed by the user. Once a constraint is active, its gradient is included in the search direction computation. An active constraint may subsequently become inactive if its value falls below CT.

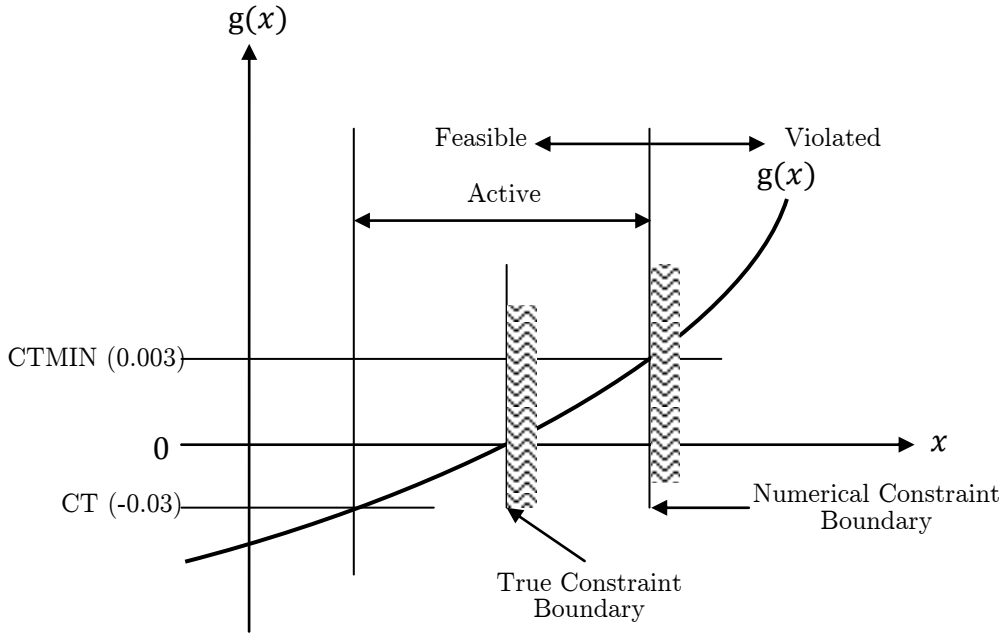

Figure A.4: CT and CTMIN

The optimiser designates a constraint as violated if its value is greater than CTMIN. The CTMIN default is 0.003, as seen in A.4. Thus, some small constraint violation (three-tenths of one percent, by default) is tolerated.

A.3 The Modified Feasible Direction Algorithm

Given an objective function $F(\mathbf{X})$ and constraints $\mathrm{g}_j(\mathbf{X}) \leq 0,\ J = 1,2,\ldots,n_g$ as well as lower and upper bounds on the design variables $x_i^L \leq x_b \leq x_i^U, i = 1,2,\ldots,n$ and given an initial $x - \text{vector}\, \mathrm{X}^0$, the design will be updated according to equation A.7 which is defined here as

$$\mathbf{X}^q = \mathbf{X}^{q-1} + \alpha^* \mathbf{S}_\mathrm{D}^q, \tag{A.7}$$

The overall optimisation process now proceeds in the following steps:

1. Start, $q = 0,\ \mathbf{X} = \mathbf{X}.$
2. $q = q + 1.$
3. Evaluate $F(\mathbf{X})$ and $\mathrm{g}_j(\mathbf{X})$ where $J = 1,2,\ldots,n_g.$
4. Identify the set of critical and near critical constraints *J*.

5. Calculate $\nabla F(\mathbf{X})$ and $\nabla \mathrm{g}_j(\mathbf{X})$ for all $j \in J$.
6. Determine a usable-feasible search direction $\mathbf{S}_{\mathrm{D}}^{q}$.
7. Perform a one-dimensional search to find α^*.
8. Set $\mathbf{X}^q = \mathbf{X}^{q-1} + \alpha^* \mathbf{S}_{\mathrm{D}}^{q}$.
9. Check for convergence to the optimum. If satisfied, exit. Otherwise, go to step, 2.

The critical parts of the optimisation task consist of:

1. Finding a usable-feasible search direction
2. Finding the scalar parameter α^* that will minimize $F\left(\mathbf{X}^{q-1} + \alpha \mathbf{S}_{\mathrm{D}}^{q}\right)$ subject to the constraints.
3. Testing for convergence to the optimum $\mathbf{X}^*$, and terminating if convergence is achieved.

The first step in finding the search direction is to determine which constraints, if any, are active or violated. In this case, an active constraint is defined as one with a value between CT and CTMlN (see previous Figure A.3), where CT is a small negative number and CTMlN is a small positive number. The constraints must be negative to be feasible; therefore, if $\mathrm{g}_j(\mathbf{X})$ is less (e.g., more negative) than CT, it is not considered active. In addition, when we approach a constraint boundary, it is predictable that we will begin moving away from that boundary. Therefore, we can initially choose a relatively large value for CT, such as -0.03. On the other hand, any constraint with a positive value is mathematically violated. Trying to achieve a precise zero on the computer, however, is not meaningful. Moreover, loads and material properties are not ever known precisely. Furthermore, the responses calculated by the finite element analysis are only approximate because of the nature of the method. Therefore, we allow for a small positive constraint value before identifying a constraint as violated. This is the value of CTMIN typically taken as 0.003. Thus, the governing definitions are

$$\mathrm{g}_j(\mathbf{X}) < \mathrm{CT}\ \text{(Inactive)}, \tag{A.8}$$

$$\mathrm{CT} \leq \mathrm{g}_j(\mathbf{X}) \leq \mathrm{CTMIN}\ \text{(Active)}, \tag{A.9}$$

$$\mathrm{g}_j(\mathbf{X}) > \mathrm{CTMIN}\ \text{(Violated)}. \tag{A.10}$$

The use of equations A.8 through A.10 underscores the importance of normalizing constraints. In MSC.Nastran, this is done automatically using the constraint bounds as normalizing factors.

Using the active constraint criteria, the algorithm first sorts all the constraints and identifies those that are active or violated. Then, the gradients of the objective function and all the active and violated constraints are calculated. Thereafter, a usable-feasible search direction is found (if one exists). There are three possibilities:

1. There are no active or violated constraints.
2. There are active constraints but no violated constraints.
3. There are one or more violated constraints.

Each of these possibilities is handled differently; the reader may refer to reference [145] for more details.

Having determined a usable-feasible search direction, we are faced with the problem of determining how far the design can be moved in that direction. Once more, a variety of possibilities exist depending on the $\mathbf{X}^{q-1}$. In each case, however, polynomial approximations are used for the objective and constraint functions in the one-dimensional search direction $\mathbf{S}_{\mathrm{D}}^{q}$.

Following the basic concept, it is necessary to try some initial value for α^* in equation A.7 and evaluate the corresponding objective and constraint functions. At the beginning of the optimisation process, very little information is available except the function values and their derivatives with respect to α^*. The one-dimensional search process now proceeds to find the bounds on the α^* that contain the solution. Once the bounds on α^* are known, the constrained minimum is found by interpolation. Since $\mathbf{S}_{\mathrm{D}}^{q}$ has been defined as a direction of improving design, the search can be limited to positive values on α^*. At the beginning of the process of finding the bounds on α^*, the values of the objective and constraints are known at $\alpha = 0$ and $\alpha = \alpha_1$, where α_1 is the initial estimate of α^*.The detailed process for finding the bounds on α^* can be found in [145].

Once the bounds of the solution to the one-dimensional search problem have been established, it is desirable to refine the solution as much as possible. To achieve

this, a polynomial interpolation of the objective and constraint functions is used. The basic tool used here is a simple polynomial curve fit, which may be linear, quadratic, or cubic, depending on the amount of information available. Experience has shown that a cubic fit can approximate the functions without introducing too much numerical error, and so higher order functions are not attempted. Whether it is objective function or a constraint that needs to be approximated, the basic approach is the same. In the optimisation algorithm contained in the Modified Feasible Directions algorithm used in DOT, the one-dimensional search process is somewhat more sophisticated, but essentially follows the same process.

Since numerical optimisation is an iterative process; one of the most critical and difficult tasks is determining when to stop. The optimisation software uses several criteria to decide when to end the iterative search process; these are described here. As with any iterative process, a maximum iteration counter is included. The default for this is 40 iterations (search directions). Usually, an optimum is found sooner than this; the maximum is mainly intended to avoid excessive computations. If the initial design is infeasible (where the constraints are violated), the first priority is to overcome these violations and find a feasible solution. If there are conflicting constraints, however, a feasible solution may not exist. If a feasible design is not achieved in 20 iterations, therefore, the optimisation process is terminated. In cases where the optimum is approached asymptotically, two criteria are used in determining when to stop. The first criterion requires that the relative change in objective between iterations should be less than a specified tolerance (DELOBJ). The default value for this is 0.001. Thus, the criterion is satisfied if

$$\frac{|F(\mathbf{X}^q) - F(\mathbf{X}^{q-1})|}{|F(\mathbf{X}^{q-1})|} \leq \text{DELOBJ}. \tag{A.11}$$

The second criterion is that the absolute change in the objective between the iterations should be less than a specified tolerance (DABOBJ). This criteria is satisfied if

$$|F(\mathbf{X}^q) - F(\mathbf{X}^{q-1})| \leq \text{DABOBJ}. \tag{A.12}$$

The default value for DABOBJ is the maximum of $0.001 \times |F(\mathbf{X}^0)|$ and 1.0×10^{-20}. The justification behind the two criteria is that if the objective function is large, the relative change between two successive iterations is an indication of

convergence. If $F(x)$ is a very small number, however, a relative change is not meaningful, and so the absolute change controls the convergence.